UNIVERSITÀ DI SIENA 1240

Dipartimento di Scienze Fisiche, della Terra e dell'Ambiente

Dottorato in Fisica Sperimentale

28° Ciclo

Coordinatore: Prof. Riccardo Paoletti

Data Analysis and Pattern Recognition in a Magnetometer Experiment

Settore scientifico disciplinare: FIS/01

Candidato:
Elisa Cali

DocuSigned by:
Elisa Cali
FB699EF7CE674B1...

Tutore:
Prof. Emilio Mariotti

Co-tutore:
Prof. Vincenzo Millucci

Anno accademico del conseguimento del titolo di Dottore di ricerca
2021-2022

Università degli Studi di Siena
Dottorato FIS/01
28° **Ciclo**

Data dell'esame finale
25/07/2022

To my uncle Guido Z"L

Contents

Abstract 1

Structure of Thesis 3

1 Magnetism and Atoms: a brief history 5

1.1 Gilbert and the "Terrellas" . . . 7
1.2 The Coulomb's period . . . 10
1.3 Gauss' period . . . 12
1.4 Maxwell's revolution and Modern Era . . . 18
1.4.1 Modern Geomagnetism . . . 23
1.5 The development of Spectroscopy . . . 25
1.6 Radiation-matter Interaction . . . 31
1.6.1 Atomic models-Thomson and Rutherford . . . 33
1.6.2 Bohr's model . . . 35
1.6.3 Sommerfeld's corrections . . . 38
1.6.4 Zeeman's effect . . . 40
1.6.4.1 The classical interpretation . . . 42
1.6.4.2 Quantum treatement of Zeeman's effect . . . 43
1.6.5 The introduction of spin . . . 45
1.6.5.1 Stern-Gerlach's experiment . . . 46
1.6.6 Magnetic Resonance . . . 48

2 Applied Magnetometry: a brief history 51

2.1 Declinometers . . . 51
2.2 Inclinometers . . . 55
2.3 Magnetometers . . . 61
2.4 Recent instruments based on classical physics . . . 70
2.4.1 Hall's effect magnetometers . . . 70
2.4.2 Fluxgate magnetometers . . . 71

2.4.3 Inductive coils . . . 72
2.5 Recent developments in Magnetometry . . . 72
2.5.1 Atomic magnetometers . . . 73
2.5.2 Applications of AMs . . . 74
2.5.3 MIT and EMI . . . 74
2.5.4 An EMI system based on Atomic Magnetometers . . . 75
2.5.5 Atomic magnetometers vs SQUID . . . 76

3 Generalities on RF Magnetometry 77
3.1 Atomic energy levels . . . 77
3.2 Hyperfine splitting of the optical resonance . . . 84
3.3 Optical pumping . . . 85
3.4 Faraday's rotation . . . 88
3.5 Optical polarization rotation . . . 90
3.6 The effect of hyperfine splitting . . . 92
3.7 Optical polarimetry . . . 94
3.8 Spin relaxations . . . 95
3.8.1 Wall collisions . . . 97
3.9 Bloch's equations description . . . 98
3.9.1 Steady-state solutions to the Bloch's equations . . . 99
3.10 Predicted resonance line shapes . . . 100
3.10.1 RF-AM linewidth . . . 101
3.11 The Density Matrix Formalism . . . 102
3.12 Fundamental noise limits . . . 103
3.12.1 Spin-projection noise . . . 104
3.12.2 Photon-shot noise . . . 104
3.12.3 Light-Shift Noise . . . 105
3.13 Sensitivity Limits . . . 106
3.13.1 Detection of Magnetometer sensitivity . . . 107

4 Fundamentals of EMI 109
4.1 Skin effect . . . 109
4.1.1 Asymptotic Limit of the Skin Depth . . . 111
4.2 Perturbation due to eddy currents (1) . . . 111
4.2.1 Perturbation due to permeability (1) . . . 113
4.3 Excitation by Helmholtz's coils . . . 115
4.3.1 Perturbation due to eddy currents (2) . . . 115

4.3.2 Perturbation due to permeability (2) . . . 116
4.4 Copper and Aluminum samples . . . 118

5 Experimental Setup **121**
5.1 Introduction . . . 121
5.2 Sensor Apparatus . . . 122
5.2.1 Vapor cell . . . 123
5.2.2 Lasers . . . 124
5.2.3 Measurement method . . . 124
5.3 Overview of UCL EMI system . . . 125
5.4 EMI-AM I . . . 126
5.4.1 Optical setup . . . 126
5.5 EMI-AM II . . . 127
5.5.1 Sensor design . . . 127
5.5.2 Sensor arrangement . . . 129
5.5.3 Active compensation system . . . 130
5.5.4 Temperature stabilisation . . . 130
5.5.5 D1 line optical pumping . . . 131
5.5.6 Magnetic field and gradient suppression . . . 132
5.6 Performance limitations . . . 133
5.7 EMI-AM II performance . . . 133

6 Imaging and Data Analysis **135**
6.1 Imaging techniques . . . 136
6.2 Electromagnetic induction images. . . . 136
6.3 Processing of data . . . 139
6.3.1 Statistical processing data . . . 140
6.3.2 Gaussian Noise . . . 150
6.3.3 Statistical Indicators: Skewness . . . 153
6.4 Filtering . . . 154
6.4.1 Convolution filters . . . 154
6.5 Conclusions . . . 164

A Atomic models **165**

B Gauss-Lamont's method **171**

C Atomic spin **175**

D Skin depth **179**

Acknowledgments **181**

Bibliography **183**

Abstract

The object of our research is the analysis of different series of data that have been collected in an experiment embedded by Prof. Ferruccio Renzoni's Group in the Laboratory of Coherent Spectroscopy at the Physics Department of University College of London (UCL).
The goal of the Thesis has been the determination of a simple, but robust algorithm able to correctly define the contour of an object, as detected by an optical magnetometer, when in presence of noise, as due by the necessary limitations in the technical construction of the experiment. Furthermore, the idea can be applied to a much larger category of experimental situations, not only in this specific kind of measurements or in this restricted field of research.
The application of the algorithm gives good results in the determination of the effective size of the studied object.

Structure of Thesis

The point of arrival of the research work presented in this thesis had to be, at first, the analysis of some data sets concerning the use of alkaline atoms as sensors for Magnetometry measurements. The experiment that produced these data involved and linked three branches of physics that had remained separate for a long time: Magnetism, Electricity and Spectroscopy.
The experiment in question in fact consists of three set-ups, each of which works on the basis of laws linked to the three scientific fields mentioned. As often happens, while we reached the pre-established goal, as we went back to the roots of the physical principles involved, the focus of our interest widened; the red thread of our discussion starts from the study of terrestrial magnetism and continues with the advent of XIX century works on electricity, up to the full $1800s$, when we began to study the relationships between chemical reactions in batteries and magnetism, between electricity and galvanism, between magnetism, electricity and heat.
The culmination came with the experimental discovery of electromagnetic waves and the arrangement of the mathematical apparatus indispensable for their description.
Another very delicate passage of absolute scientific interest is the concept of "field", which developed in XIX century in dichotomy with respect to that of electric charge. On the basis of this new theoretical apparatus, electrical and magnetic phenomena were brought back into a single elegant and mathematically solid description.
At the same time, the spectroscopic analysis had developed which, starting from the analysis of the stellar radiation spectra, made it possible to trace the chemical constitution of the star. This branch of physics has laid the foundations for understanding the intimate nature of compounds leading to a large number of hypotheses about the structure of atoms and the consequent affirmation of various atomic models. This scientific adventure continues to

be a particularly fertile topic and it therefore seemed interesting to us to summarize the most significant passages.
One of the greatest goals of Modern Physics is the use of neutral atoms as very precise and absolute "meters" of the physical World. In fact, even in the definition of the fundamental units, the tendency is to use natural objects, replacing, when possible, our artifacts. However, atomic samples can reveal much more when interacting with light, becoming the basic components of optical sensors. Our attention will be focused on the recent possibility of transforming atoms into magnetic detectors.
In Chapter 1 we reconstructed the history of the theoretical hypotheses and of the experimental tests carried out over the centuries for the understanding of electrical and magnetic phenomena. The affirmation of spectroscopic techniques, the starting point for the subsequent hypotheses on light radiation and atomic structure, was then deepened.
In Chapter 2 we extensively dealt with the history of instruments such as declinometers, inclinometers and classical magnetometers until it was understood how even the atoms themselves could be used as "sensors" for measuring magnetic fields.
In Chapter 3 we dedicated ourselves to the deepening of the quantum phenomena at the basis of Atomic Magnetometry, also from a mathematical point of view, coming to analyze in detail the Density Matrix and the Bloch equations.
The Chapter 4 deals with the phenomena underlying Electromagnetic induction imaging (EMI), in particular the Skin Effect and the Eddy Currents induced by magnetic fields in conductive cells.
The images presented in the Chapter and were taken from the doctoral thesis of Dr. Cameron Deans, researcher in the group of Professor Ferruccio Renzoni at the Department of Physics and Astronomy of the University of London.
In Chapter 5 is described in detail the experimental apparatus built by the aforementioned group, from which the images of analyzed data sets come.
In Chapter 6, the final one, we describe the procedure carried out for the analysis (processing) of the Data. The techniques used belong to basic classical statistics. It is this generic nature that allows the developed algorithm to be applied to any sample, be it metallic or biological.

Chapter 1

Magnetism and Atoms: a brief history

Magnetic fields can be detected wherever charges are in motion, but understanding each stage of the scientific adventure linking up early discoveries to modern devices is a long journey.
To begin with, there is a little dispute over the origin of the word magnet. Pliny the Elder, who lived from 23BC to 70BC, wrote that Magnes, a shepherd, had noticed that the nails of his shoes and the iron tip of his staff were sticking to the magnetite-rich rocks on the Mount Ida. According to another version, much more accredited than the previous one, it is believed that the word magnet recalls the name of the city of Magnes, in Turkey.
The only certain fact is that the compass, an instrument based on the properties of ferromagnetic materials, was invented in China between the II century BC and the I century BC, during the Han dynasty.
The Chinese had in fact discovered that when a magnet is hung or positioned so that it can rotate freely, it will always point towards the same direction. This object was used for divination, geomancy, the search of precious stones and for Feng Shui.
The use of the compass spread to Europe in the early Middle Ages and immediately proved indispensable for maritime navigation. Naval compasses consisted of a magnetic needle suspended in the water so that the needle could remain in a horizontal position at sea level.
In the history of Magnetism a central role is undoubtedly related to Pierre Peregrinus De Maricourt, a priest and scientist who lived during the XIII century. His work, "The Epistole" is one of the most impressive scientific

treatises of the Middle Ages and remained a point of reference for scientists right up to the Late Renaissance. He was responsible for identifying the four characteristics of the magnet: color, homogeneity, weight and virtue and applied the term *magnetic pole* (Figure 1.1).

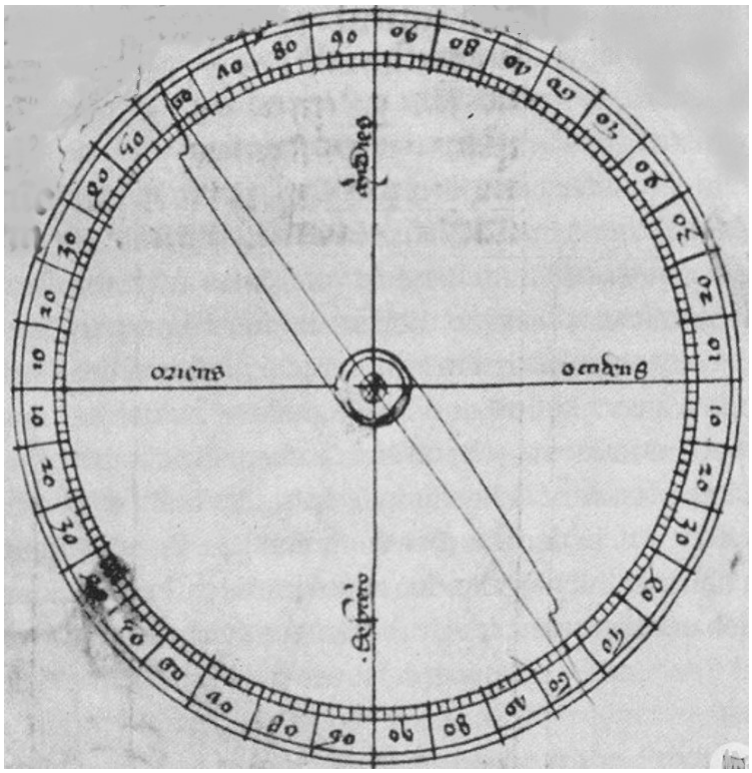

Figure 1.1: De Maricourt's Earth model.

Subsequently, starting from XVII century until the end of XIX, it is possible to conventionally identify four periods in the history of magnetism which will be analyzed in detail in this thesis work:
1 - The first period ranging from 1600, when William Gilbert $(1544 - 1603)$ publishes "De Magnete", to 1777, when Charles De Coulomb $(1736 - 1806)$ reads out an important memoir on magnetism in front of the Paris Academy of Sciences;
2 - The second period ranging from 1777 to 1833, year of publication of the Carl Friedrich Gauss' $(1777 - 1855)$ description of a device that he called a magnometer;
3 - The third period from 1833 to 1873, year of publication of the "Treatise on Electricity and Magnetism" by James Clerk Maxwell $(1831 - 1879)$;
4 - The fourth period from 1873 to 1919, when Joseph Larmor $(1857 - 1942)$

reported an important memoir on the origin of magnetism in rotating bodies.

1.1 Gilbert and the "Terrellas"

After centuries of investigations on magnets, it was assumed that their behavior was not understandable. The beginning of the era of great navigations favored the multiplication of investigations on terrestrial magnetism and magnetic declination. This quantity, fundamental for maritime orientation, is defined as the angle between the direction of the geographic north and that of the magnetic north.
It was now understood how the Earth could be assimilated to a huge magnet which, due to the ferrous masses present in the subsoil, generates a magnetic field. This field determines the magnetic poles and the magnetic meridians, distinct from the geographic ones.
Compass needles, being magnetized, point towards magnetic North Pole, not the direction of the geographic North Pole. It was necessary to determine how to correct the angular values given by the compass needle. Further complicating these problems is the fact that the magnetic declination is not fixed, but varies temporally and spatially.
In Europe, already following the observations made by Cristoforo Colombo $(1451 - 1506)$ in the second half of the XV century, the nature of this phenomenon was understood, to which was added the need to account for another phenomenon of considerable importance: the magnetic inclination which is the angle formed by the direction of the Earth's magnetic field with the horizontal plane at any point on the surface of the Earth.
The magnetic inclination varies from place to place: it is zero at the Equator and increases with latitude until it reaches its maximum value $(90°)$ at the magnetic poles.
In fact William Gilbert, the court physicist of Queen Elizabeth I, reported his discoveries in "De Magnete, Magneticisque Corporibus, et de Magno Magnete Tellure". On the basis of careful observations, he had established that the properties of magnets of attracting iron materials or other magnets were different from the attraction capacity possessed by rubbed amber. He therefore concluded that there were two distinct poles in the magnets and renamed them Southern and Northern Pole.
In particular, he verified that if the two poles were homologous, they repelled

each other while if they were opposite they attracted each other. The model of the Earth he devised, the "Terrella", represented the planet as a huge natural magnet (Figure 1.2).
A magnetic needle free in orientation does not always align itself along the Northern Pole-Southern Pole direction: if this needle is free to move on a vertical plane, it will form an increasing angle with the horizon with the latitude.
From this moment on, the Terrellas, have been used in science to investigate and demonstrate magnetic, electrostatic and electromagnetic phenomena. Gilbert's observations mark the beginning of the experimental analyses of

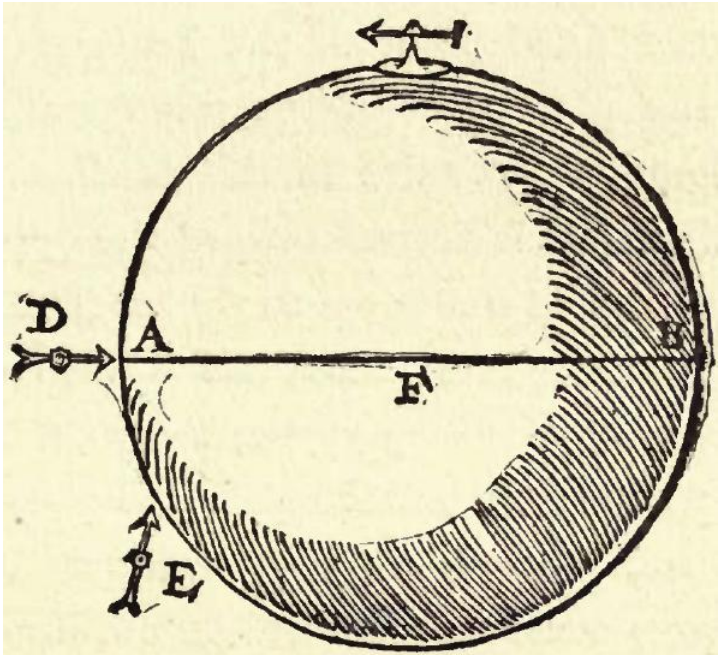

Figure 1.2: Terrella-William Gilbert's explanation was that the Earth itself is a giant magnet. He demonstrated this by creating a scale model of the magnetic Earth, a sphere formed by a magnet. Gilbert demonstrated that a horizontal compass would point towards the magnetic pole, while a plunging needle, balanced on a horizontal axis perpendicular to the magnetic one, indicated the correct magnetic inclination between the magnetic force and the horizontal direction.

magnetism but René Descartes $(1596-1650)$ was the scientist who-accepting the Gilbertian interpretation of the Earth as a natural magnet-provided a mechanistic interpretation of the behavior of magnetic objects.
The French scientist believed that the magnets did not have channels in the

North-South direction, but that inside them there was a flow of aether capable of circulating between the two poles. In his theory of magnetism, the alignment of the magnets in the north-south direction was caused by the flow of matter exerting pressure on the walls of the magnetic channels.
Furthermore, Descartes explained the variations in magnetic declination with the difference in the destruction of magnetic and ferrous substances in the Earth's surface. The Cartesian theory of natural phenomena deeply influenced the scientific activity of natural philosophers and throughout the first half of the XVIII century the adherence to this interpretation was very wide. It is easily predictable the problems of spatial orientation linked to maritime trade moved interests and economic funds, so that the main scientific academies rewarded the most active researchers.
Among the winners of the prizes offered by the Paris Academy of Sciences, for example, we find prominent names such as Leonard Euler $(1707 - 1783)$ and the Bernoulli, both Daniel $(1700 - 1782)$ and Johann $(1710 - 1790)$ faithful to Descartes' interpretation of magnetic phenomena. This line was opposed by the followers of Newton, who struggled between an interpretation of the magnetic action as due to a force at a distance in the absence of a medium and the hypothesis of the presence of a fluid in which all the objects of the physical universe are immersed. In the second hypothesis, it is the characteristics of the transmission medium which determine the methods of interaction.
To provide further magnetic models of the Earth Edmond Halley $(1656 - 1742)$, who in his memoir hypothesized that the Earth had four magnetic poles adjacent to the geographic poles and that a free-to-orient needle undergoes the action of the pole closest to it. Halley also hypothesized that the Earth had the shape of an empty shell inside which a solid body with the same center of gravity rotated; moreover, between the two globes-for each of which two magnetic poles were defined-there was a fluid medium.
A theory on Magnetism opposed to the Cartesian one is pursued by Franz Ulrich Theodor Aepinus $(1724 - 1802)$, who in a essay on electricity and magnetism, argued that all magnetic phenomena were the result of the reciprocal action of the forces exerted by masses of fluid.
This approach is interesting because it tries to give a mathematical treatment to the study of Magnetism. The attempt was not fully successful, because there was still no law of attraction between two magnets or poles considered isolated from each other.

Furthermore, the poles of the magnets are not isolated and therefore he was unable to obtain an inverse square law similar to the Newton's law for gravitation. After all, Isaac Newton (1642 – 1726) himself in the "Principia" had stated that the law of action between magnets does not go according to the inverse square law but according to the inverse cube law. Precise measurements in this sense had been made by the Genevan Giovanni Ludovico Calandrini (1703 – 1758), who had come to the conclusion that the torque exerted by a magnet on a magnetic needle varies inversely to the cube of the distance between the magnet and the needle for large distances in relation to the length of the needle.
At a competition launched by the Académie des Sciences of Paris in the 1840*s*, the question was posed of the best way to build a tilt compass. In the three winning memoirs, neo-Cartesian points of view were supported by placing a firm statement on two aspects of magnetism: a magnetic needle freely suspended in the plane of the magnetic meridian, when deflected from its equilibrium position, oscillates with harmonic motion. The period of the oscillations is inversely proportional to the product of the Earth's magnetic force and the magnetic moment of the needle. The lack of coincidence between the relative rotation times between two globes was traced back to the centuries-old change in the declination of the needle.
Between the end of the XVII century and the beginning of the XVIII various expeditions were made to different places on the planet to verify Halley's theories and in his honor the lines passing through the points of equal declination were baptized *halleyan lines*.

1.2 The Coulomb's period

In 1775 Charles De Coulomb presented at the Acadèmie des Sciences of Paris a memoir on the construction of magnetic compasses; in this work the theory of twisting in thin threads of silk and hair and the use of these in the suspension of magnetic needles was developed (Figure 1.3).
It was shown for the first time that torsion suspension could provide a method for the accurate measurement of small forces; Coulomb designed the torsion balance for this purpose. The measurement of the Earth's magnetic field was obtained by swinging the needle and calculating the mechanical moment that balanced the movement of the Earth's magnetic field. Coulomb's works are

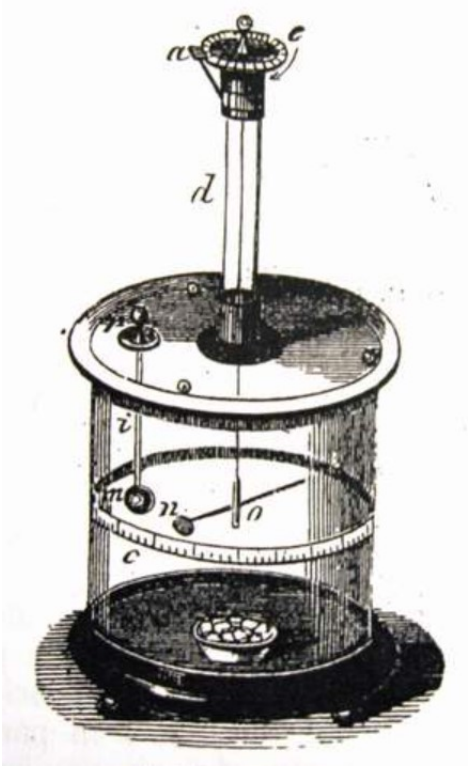

Figure 1.3: Coulomb's torsion balance: the horizontal lever consists of a shellac nozzle which supports a conducting disk or globe; the test surface is brought into contact with the globe or disk of the lever, and the repulsion generated is then measured.

important for two reasons, one of a general kind because they allowed us to ascertain the fruitfulness of the concept of action at a distance and another more specific because with his torsion balance he introduced an instrument and method of measurement which would give extraordinary results. With his balance, Coulomb found for the isolated magnetic poles a law of force similar to the Newtonian one for the masses.
Coulomb also imagined a physical model that could account for the fact that it was not possible to isolate a magnetic pole: both the theory of vortices of Cartesian inspiration and the theory of two fluids were not able to explain the phenomenon. Magnetism was thus moved from the category of phenomenological disciplines into the general Newtonian description of natural phenomena.
In the theory, two problems remained:
1 - What are the quantities whose knowledge univocally determines the value of the magnetic force of the Earth;

2 - Which is the value of the intensity of the Earth's magnetic force as a function of the units provided.
The first problem was solved by Jean Baptiste Biot ($1774 - 1862$) who presented in 1804 a paper on terrestrial magnetism at different latitudes, starting from the definition of the parameters which characterize the behavior of a magnet.

1.3 Gauss' period

In 1833 Gauss, published the "Intensitas Vis Magneticae Terrestris Ad Mensuram Absolutam Revocata". In it he formulated the hypothesis that the imponderable magnetic fluids confined in every molecule of the body are closely related to the ponderable particles of the bodies. Since the force manifests itself with an acceleration on a given mass, even a force between two units of magnetism will be equivalent to an acceleration on a given mass for which fundamental mechanical quantities could be assumed such as distance, mass, time.
Starting from reading Biot's "Traité de Physique" (1824) and Simèon-Denis Poisson ($1781 - 1840$) memoir on the distribution of electricity on the surface of conducting bodies, Gauss solved the difficulty of the fact that equal quantities of magnetic fluid existed in each molecule, but at poles they acted alone. He replaced the internal magnetism of a body with a superficial distribution such that an element, placed on the outside, was affected by an action equal to that of the really distributed magnetism.
With the use of fundamental quantities L, M, T and as units mm, mg, s, the magnetic field B is expressed by $[B] = [M^{1/2}][L^{-}1/2][T^1]$ while if they are used as fundamental quantities L, M, A (A=acceleration) B is expressed by $[B'] = [M^{1/2}][L^1][A^{1/2}]$.
The ratio between the B expressed in the two measurement systems is equal to 0.01009554. The unit of measurement of magnetism μ is defined starting from Coulomb's law for magnetism ($f\mu_1\mu_2/r^2$), imposing the condition that f, the dimensional constant of proportionality, is equal to 1 and has the following physical dimensions $[\mu] = [M^{1/2}][L^{3/2}][T^{-1}]$. Gauss put $f = 1$ in Coulomb's formula.
The problem which remained open was that the definitions of Earth pole intensity and magnetic intensity clearly met the demands for stability and

repeatability, but it was not immediately clear how this feature could be translated into precise measurements, because the magnetic poles were unclearly located.

Gauss achieves this by giving a physical meaning to the mathematical quantity which first appeared in Biot and Poisson's essays on magnetism: the concept of *magnetic moment*. Having found the functional relationships between the magnetic moment and the magnetic axis and the macroscopic observables, Gauss was able to give a satisfactory operational definition of the moment: the unit magnetic moment. In fact, it exerts an unitary torque on a similar magnet placed at a unitary distance.

Gauss was therefore able to exclude magnetic poles from his research and to deal only with magnetic moments, that is, with macroscopic observables. Once the problem of the operational definition of a magnetic pole was circumvented, he was able to make the procedure suggested by Poisson applicable and to find another relationship between the magnetic moment M and an external field B_0.

Finally, Gauss designed the instrument - the magnetometer - which would allow him to measure both the product between M and B_0 and the M/B_0 ratio.

The innovation of the instrument-compared to Coulomb's magnetic balance-was constituted by the fact that, apart from the dimensions of the instrument, a mirror was mounted on the bar: in this way the instrument could be read from a distance with a theodolite.

The measurement mode also ensured an accuracy comparable to that of astronomical measurements. To find the product MB_0 Gauss suggested using the oscillation method, introduced by Euler, although corrected in some places to increase its accuracy. In addition, to find the M/B_0 ratio, Gauss inspired the Poisson method: that is, the analysis of the interaction between two magnets which would lead him to the identification of the experimental procedures for the calculation.

Using the principle of $Virtual\ works$, he found the condition of equilibrium for a needle subjected simultaneously to the action of terrestrial magnetism and another needle. In particular, a needle was swung in the magnetometer previously used to find the MB_0 product under the action of the needle used to find the product.

Gauss, however, did not start from Coulomb's law, but left the power of the distance undetermined, which he generically set equal to n. He developed the

equilibrium condition in the general case of any n: the experiment allowed to find the coefficient n of Coulomb's law: under the given experimental conditions it was equal to 2. It was the first time that Coulomb's law for magnetism found its experimental verification with a procedure other than the one adopted by the French scientist.

The theoretical context in which Gauss set his studies on magnetism was that of the theory of potential; in 1839 he published the "Allgemeine Theorie der Erdmagnetismus" which began the modern analysis of the configuration of the magnetic field on the Earth's surface [13]. Let F be the magnetic force exerted between infinitesimal element of Magnetism $d\mu$ and let r be the distance of a generic $d\mu$ from a given point in space. At that point the magnetic potential V deriving from all $d\mu$ of the Earth will be

$$V = -\int \frac{d\mu}{r} \tag{1.1}$$

whose gradient will give the total magnetic force F. At any point O in the space V can be considered a function of three variables which expresses the position of that point with respect to a reference system.

Gauss chose the distance of O from the center of the Earth r, the colatitude u (the angle between r and the northern part of the Earth's axis) and the longitude λ (the angle, considered positive towards East, between a plane passing through r and the terrestrial axis and a prime meridian). Expanding V in decreasing series of powers of r:

$$V = \frac{R^2 P^0}{r} + \frac{R^3 P'}{r^2} + \frac{R^4 P''}{r^3} + \frac{R^5 P^{n'}}{r^4} + ... \tag{1.2}$$

where the P^n (connected with the distribution of $d\mu$ on the Earth) are functions of u and λ, and R is the radius of the supposedly spherical Earth. The explicit expression of the P^n is

$$P^n = g^{n,0} P^{n,0} + (g^{n,1} cos\lambda + h^{n,1} \sin\lambda) P^{n,1} + (g^{n,2} \cos 2\lambda + h^{n,2} \sin 2\lambda) P^{n,2} + ...$$
$$+ (g^{n,n} \cos n\lambda + h^{n,n} \sin n\lambda) P^{n,n} \tag{1.3}$$

in which the $g^{n,0}$, $g^{n,1}$, $h^{n,1}$, $h^{n,2}$, etc. numerical coefficients are determined, and the $P^{n,m}$ are the following functions of u

$$P^{n,m} = (\cos u^{n-m}) - \frac{(n-m)(n-m-1)}{2(2n-1)} \cos u^{n-m-2} +$$
$$+ \frac{(n-m)(n-m-1)(n-m-2)(n-m-3) \cos u^{n-m-4}}{2x4(2n-1)(2n-3)} - ... \sin u^m \tag{1.4}$$

In modern geomagnetic texts, the P used by Gauss, i.e. the *associated Legendre functions* or the *spherical functions* are replaced by the nearly normalized *Schmidt functions*. If the magnetic force F at the point O is decomposed into three perpendicular forces X, Y and Z with Z directed towards the center of the Earth, X and Y tangents to the concentric spherical surface of the Earth passing through O. We assume X directed towards the North and lying on a plane passing through O and the axis of rotation of the Earth, Y orthogonal to X directed towards East and lying on a plane parallel to the Equator. So we have

$$X = +\frac{\partial V}{r\partial u} \tag{1.5}$$

$$Y = -\frac{\partial V}{r\sin u\partial\lambda} \tag{1.6}$$

$$Z = +\frac{\partial V}{\partial r} \tag{1.7}$$

(in modern notation). Since the quantities of magnetism of opposite polarity are equal in the total volume of the Earth, i.e. that $P^0 = 0$, we have

$$X = +\frac{R^3}{r^3}\left(\frac{\partial P'}{\partial u} + \frac{R}{r}\frac{\partial P^n}{\partial u} + \frac{R^2}{r^2}\frac{\partial P^m}{\partial u} + ...\right) \tag{1.8}$$

$$Y = -\frac{R^3}{r^3\sin u}\left(\frac{\partial P'}{\partial\lambda} + \frac{\partial P^n}{\partial\lambda} + \frac{\partial P^m}{\partial\lambda} + ...\right) \tag{1.9}$$

$$Z = +\frac{R^3}{r^3}\left(2P' + \frac{3RP^n}{r} + \frac{4R^2P^m}{r^2} + ...\right) \tag{1.10}$$

For points on the surface of the Earth the expressions of the forces become

$$X = +\left(\frac{\partial P'}{\partial u} + \frac{\partial P^n}{\partial u} + \frac{\partial P^m}{\partial u}...\right) \tag{1.11}$$

$$Y = -\frac{1}{\sin u}\left(\frac{\partial P'}{\partial\lambda} + \frac{\partial P^n}{\partial\lambda} + \frac{\partial P^m}{\partial\lambda} + ...\right) \tag{1.12}$$

$$Z = (2P' + 3P^n + 4P^m\ ..) \tag{1.13}$$

These expressions of X, Y, Z allow (in principle) to calculate the values of F over the entire Earth's surface. In fact, the numerical coefficients appearing in the $P^{(n)}$ can be determined, once the experimental values of the magnetic force are known for a sufficient number of points, each identified with its geographic coordinates u and λ.

Each value of X or Y or Z, obtained from the F measured at that point,

will provide an equation into which the coefficients of the P^n enter, so once established at which order we want to stop the series development of the P^n, consequently having established how much equations are needed to determine the desired coefficients, the minimum number of experimental observations necessary will be fixed.

If, as proposed by Gauss, the series is stopped at the fourth-order, 8 complete observations of intensity, declination and inclination are sufficient to determine the 24 coefficients needed. In fact, it was possible to obtain, already at the time, a higher number of observations, on which, however, loomed the unknown force of accidental errors which, added to the terms neglected in the series expansion, could considerably invalidate the results.

It was for this reason that Gauss suggested to use the least squares method and was able to calculate the position of the North Pole and the South Pole. For the North Pole he had found a north latitude of $73^\circ\ 35'$ and an East longitude of $264^\circ\ 21'$ and for the South Pole a south latitude of $72^\circ\ 35'$ and a longitude East of $152^\circ\ 30'$. He then corrected the calculated value of the South Pole to 66° South and 146° East.

Captain John Ross $(1777 - 1856)$, who led various scientific expeditions to test the theory, had measured the position of the North Pole at $3^\circ\ 30'$ further South. The position of the South Pole had not yet been observed at the time of the publication of the memoir.

In the years $1837 - 1839$ three expeditions were organized in search of the magnetic South Pole but none of the three succeeded. On a later expedition, Captain Ross was able to locate him at 75° South and 154° East in Victoria Land, but found no place to disembark. The South Pole was only reached in 1908.

With the Gauss' work, Magnetism becomes a discipline with its own specific physical and mathematical language and at the same time the theory of potential leaves the field of pure mathematics.

In 1840 Gauss published a further memoir of a mathematical nature on the properties of forces which act in inverse ratio to the square of the distance; it constituted the point of reference for those who wanted to conduct research in the field of physical sciences [115].

The Gaussian analysis showed that 94% of the Earth's magnetic force was derived from inside the Earth and 6% from external contributions. To refine the results it was necessary to have systematic measurements with the same instruments and the same procedure at various points on the Earth's surface

[12] The "Magnetische Verein" intensified geographic exploration and the

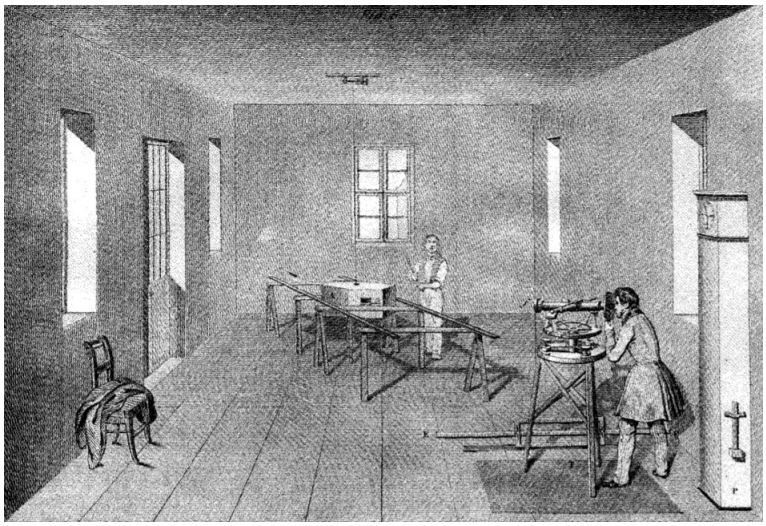

Figure 1.4: Gaussian apparatus for magnetic intensity measurements. A. Becquerel 1834 – 40, Vol. 7: plate 5.

construction of new magnetic observatories around the globe: it promoted collaborative geomagnetic research.
Alexander Humboldt (1769 – 1859) played a central role in setting up and developing international collaborations.
The procedure and the tools developed by Gauss underwent slight changes over the following decades, essentially due to practical reasons. The single-wire magnetometer, for example, due to its size and its fragility, was an instrument suitable for fixed magnetic observatories where it was able to provide values of horizontal intensity of declination with great precision.
For measurements in places without fixed magnetic observatories, smaller magnetometers were designed based on different principles.
The measurement procedure suggested by Gauss was slightly modified by Kew's magnetometer, one of the most used instruments for its reliability in the second half of the XIX century. It adopted the procedures put in place by Johann Lamont (1805 – 1879) known in literature as the method by Gauss-Lamont [73]. See Appendix 1 for more details.
Unfortunately, the single-line magnetometer did not ensure the same accuracy in the measurement of time variation in the horizontal intensity. It was for this reason that Gauss and Wilhelm Weber (1804 – 1891) again designed the bifilar magnetometer.
Gauss paid little attention to the measurement of the inclination as the in-

struments of his time did not satisfy him.
A widely used inclinometer in the second half of the XIX century was that of Henry Barrow ($1790 - 1870$). Furthermore, Weber had designed an inclinometer - the terrestrial inductor - but its use only became widespread in the XX century.
Ultimately, in the second half of the XIX century the following instruments were available for measuring the elements of the Earth's magnetic force of its spatial and time variations:
- Gauss' single-wire magnetometer: used essentially, with the Gauss-Lamont's method, for declination measurements and for the absolute measurement of the horizontal component of the Earth's magnetic force;
- Henry Prudence Gambey's declinometer ($1787 - 1847$): used to measure the temporal variation of the declination;
- Two-wire Gauss' magnetometer: used essentially for measuring the temporal variation of the horizontal component of the Earth's magnetic force;
- Barrow's inclinometer: used for the measure of inclination;
- Humphrey Lloyd's balance ($1800 - 1881$): used to measure the variation of the vertical component of the Earth's magnetic force;
- The variation of the inclination was obtained indirectly from the ratio between the vertical component and the horizontal component.
Starting from the XIX century, Gauss' memoirs gave rise to important research programs for scholars of terrestrial magnetism. After a few decades some fixed points had been acquired
a - The Earth's magnetic field is due, in its large part, to a dipole whose axis passes at $77^\circ\ 50'$ of North latitude $286^\circ\ 29'$ longitude and South latitude and $116^\circ\ 29'$ of longitude;
b - The Earth's magnetic field undergoes diurnal, annual, secular variations, the regularity of which was hypothesized by extrapolating the available data;
c - The Earth's magnetic field is subject to sudden rapid variations.
Any theory of terrestrial magnetism, to be considered valid, would have had to provide convincing explanations of the established methods.

1.4 Maxwell's revolution and Modern Era

We now propose to broadly reconstruct the scientific understanding of electrical and magnetic phenomena throughout the course of the XX century.

Among the giants of this scientific epic stands the figure of the chemist and natural philosopher Michael Faraday ($1791 - 1867$), who in his career distinguished himself for the multiplicity of in-depth scientific fields: metal alloys, electrochemistry, discovery of benzene, optical glasses, electromagnetic and electrostatic induction, diamagnetism and paramagnetism, radiative vibrations, etc. As evidence of the intensity of this scientific production, there are books bound by Faraday himself containing as much as $16,000$ in notes and notes.

The first of his intuitions, concerned the existence of an elementary unit of electric charge, was accomplished while he was conducting experiments on electrochemical decomposition. His belief in the existence of a unity of natural phenomena was thus supported by the fact that electricity seemed to build a bridge between physics and chemistry.

In 1819, the Danish Hans Christian Oersted ($1777 - 1851$), during an educational experience on the thermal effects of a current-carrying copper wire, discovered that a magnetic needle positioned in the vicinity of a metal wire connected to a galvanic, it rotated until it assumed a position perpendicular to the wire itself. In July 1820 published his results under the title "Experimenta circa effectum conflictum electrici in acum magneticum".

On the basis of what is reported in these memoirs, the French physicist André Marie Ampère ($1775 - 1836$) performed a series of experiments using two parallel conductors between which an attraction or repulsion force developed depending on the direction of the current, reaching to the recognition of a similar behavior between solenoids and magnets. He therefore concluded that the magnetism was generated by currents inside the magnets and that the magnetic force could be traced back to a central force due to the currents. On this point Faraday found himself to be in total disagreement to the point that he published an anonymous note in 1821; citing an experiment he conducted himself, he asserted that the direction of the magnetic field of a magnetized iron tube was reversed passing from the inside to the outside. Ampère, called into question, resolved the question by hypothesizing that the currents of a permanent magnet circulate around the molecules that compose it instead of around its magnetic axis. Not only that: the forces acting between two conductors depended both on the direction of the currents and on the distance with the $1/r^2$ trend.

The "quarrel" between the two pioneers of electromagnetism continued and assumed continental proportions, pitting the British and French academic

worlds against each other. All that favored a frenetic scientific activity throughout Northern Europe, also involving Denmark and especially Germany.

Georg Simon Ohm ($1789 - 1854$) found that the current in the conductors flowed with a dependence on the metal used and in a manner proportional to the cross section of the wire in which the current itself was to pass. In this way, in 1826, he defined the concepts of potential difference or electromotive force and resistance and through his homonymous law, he associated them with the intensity of current.

In 1831 Faraday, after having discovered the interconnection between magnetic effects and electric currents, finally found that it was possible to produce electricity dynamically through the relative motion between a magnet and an electrical circuit; he also found that by winding two separate coils around an iron core and sending a pulse of current into the first, an electric current was induced in the second.

Rejecting the atomistic conception of matter and in open opposition to the analytical methods of French physicists, he published the famous memoir "Magnetic induction" in which the "overall process" was interpreted according to the Jesuit father Ruder Josip Boscovich's atomic theory ($1711 - 1787$). Electric, magnetic, gravitational phenomena and the radiation itself were explained by assuming that matter was composed of centers from which direct lines of force radiate throughout space.

Faraday, at this point, chose to devote himself to the study of electrical induction and the effects that electric or magnetic fields had on light.

In 1845 he discovered that a block of glass subjected to the action of a strong magnet was able to rotate the polarization plane of a beam of light passing through it. A subsequent series of experiments allowed him to understand that substances considered inert to magnetism also had an influence on induction.

In his memoir of 1846 entitled "Thoughts on Ray-Vibrations", he concluded that if the medium modifies the induction, not only the concept of action at a distance was discarded but also the hypothesis of an instantaneous propagation of physical actions was also lost. Instead he chose to introduce the concept of a field represented by lines of force which, by vibrating, caused the radiative processes.

Among Faraday's subsequent contributions there is also the magneto-optical effect which will be explained at length in Chapter 3. Meanwhile Weber and

Gauss developed a theory of electrical and magnetic phenomena based on the idea of discrete electric charge and electric current as the motion of charges. They were able, within two years, to derive an analytical expression for the force exerted between two charges in relative motion. In addition to the Coulomb force term, there appeared a relativistic correction proportional to v/c^2 with v relative speed, and a radiative term proportional to the acceleration and inversely proportional to the distance. The coefficient c would have turned out to be equal to the speed of light. Gauss conjectured that this non-radial and distance-independent force was not instantaneous but retarded.

The decisive step in establishing the connection between light and electromagnetism was taken by the Scottish physicist James Clerk Maxwell $(1831 - 1879)$, who began to develop a unified theory of the electromagnetic field. In his first seminal contribution, published under the title "On Faraday's Lines of Force" of 1856, Maxwell used the analogy with the motion of an incompressible fluid to illustrate the concept of a line of force to represent the direction and intensity of the force of the imaginary fluid. This model did not account for the inductive phenomena whereby a variation of magnetic flux gives rise to an electromotive force in a chained circuit. Faraday had assumed that this depended on the variation of an electrotonic state of the circuit.

To this effect Maxwell dedicated the second part of the 1856 work, with the title "On Faraday's Electro-tonic state" in which he used the results of the theory of potential and applied the general concept of conservation of energy, introducing the vector potential function and obtaining a series of differential equations for current, electromotive force, induction and magnetic field.

In his second work on electromagnetism, published between 1861 and 1862 under the title "On the Physical Lines of Force," Maxwell used a complex mechanical model to illustrate the physical characteristics of a medium capable of transmitting electromagnetic actions. Space, in this conception, appeared filled with separate vortices whose rotation axes were aligned with the direction of the magnetic field, so the electrotonic function was nothing more than an angular momentum associated with the vortices whose derivative over time contributed to the electromotive force.

At the same time Maxwell introduced elastic properties to his model, considering the cases of polarization of dielectrics as a particular case of electrical conduction: the applied voltage is stored as potential energy in the form of

elastic energy associated with the deformations of molecular vortices. The electric matter would have moved from its equilibrium position while remaining bound to the molecules that would have become polarized, giving rise to an overall displacement of electricity that could be interpreted as the "beginning" of a current. This fundamental breakthrough made it possible to complete Ampère's equation with the introduction of the displacement current, a reciprocal term to Faraday's law of induction. It was clear that a variable electric field could generate a magnetic field and that the propagation of electromagnetic waves with a speed equal to that of light was possible, bringing optical and radiative phenomena back into Maxwell's theory.
In the article "A Dynamical Theory of the electromagnetic Field", divided into seven parts and published in 1865 by the Royal Society and finally in the monumental "Treatise on Electricity and Magnetism" of 1873, Maxwell, starting from the potential function, expressed the laws of induction and derived the action of the electromagnetic field from the principle of conservation of energy.
The most famous part of the Treatise is undoubtedly the third, in which the whole theory of the electromagnetic field is expressed through twenty equations in twenty unknowns. Among these, in addition to the vector potential, there is even a term to take into account the possible existence of magnetic monopoles. Finally, in the sixth part of the work, entitled "Electromagnetic Theory of Light", Maxwell derived the wave equations for the propagation of the potential function and the magnetic field.
Maxwell also derived the existence of a radiation pressure whose experimental proof was obtained by Pyotr N. Lebedev ($1866 - 1912$) in 1899. The problem contained in Maxwell's theory was related to the fact that electric charge was conceived as a displacement produced by the field, as opposed to continental European physicists who considered charge as a primitive notion. The idea of displacement prevented the consideration of radiative sources as constituted by oscillating charges, hindering the experimental verification of the theory.
These equations were later simplified by Oliver Heaviside ($1850 - 1925$) to whom we owe the modern formulation of Maxwell's equations. In the case in which the propagation occurs in material means, there are the following relationships between electric field and magnetic field

$$\Phi_S(\mathbf{E}) = \frac{\sum q_i}{\varepsilon} \tag{1.14}$$

where Φ indicates the electric flux through a surface and with q the charges inside the surface itself.

$$C(\mathbf{B}) = \mu \sum i_i \tag{1.15}$$

where C(B) indicates the circulation of the magnetic field along any closed path and μ is the magnetic permeability of the medium.

$$\Phi(\mathbf{B}) = 0 \tag{1.16}$$

where Φ represents the magnetic flux

$$fem = -\frac{\Delta\Phi(\mathbf{B})}{\Delta t} \tag{1.17}$$

where fem is the induced electromotive force.
The revolutionary importance of these equations was only fully understood in 1887, when the German physicist Heinrich Rudolf Hertz (1857 – 1894) experimentally verified the existence of electromagnetic waves: he triggered high-frequency discharges in simple electrical circuits including an inductance, and was able to pick them up with resonant circuits in which the reception of the wave was still revealed by a discharge. He also showed that these waves show the same phenomena as light, such as reflection, refraction, diffraction, interference and polarization.

1.4.1 Modern Geomagnetism

In his "Treatise" Maxwell re-proposes the Gaussian treatment (part III, chapter VIII-"The Terrestrial Magnetism" completed with an accurate description of the instruments used in magnetic measurements and the procedures for determination of the magnetic axis and the intensity of the magnetic force at a given point (part III, chapter VII). The treatment of the origin of terrestrial magnetism is lacking in the Treatise [75]; although there is no specific analysis of this problem, the scholars of Geomagnetism were provided with a theoretical framework for the construction of new physical models. Moreover, they were able to account for the observational data on the spatial and time behavior of the field that the measurements made after Gauss had highlighted.
After Maxwell, scientists were convinced that the solution to the problem of the origin of terrestrial magnetism lay in the fields of electricity and atmospheric physics rather than that of pure magnetism.

Alfred Nippoldt (1874 – 1936) and Arthur Schuster (1851 – 1934) published two review articles of the state of geomagnetic knowledge. They are very useful in the historical reconstruction of the studies carried out in the previous decades. Two features are evident:
1 - The research carried out in those years, even in its specificity, was accumulated from the attempt to find, on the basis of the geomagnetic data available, the trend of the atmospheric surface electric currents which generated them and a mechanism for their generation. The focus was essentially on the analysis of the variable part of the Earth's magnetic field;
2 - In the first decades of the XIX century, hypotheses were advanced which relate the rotation of bodies (as, for example, the planet Earth) to the generation of magnetism.
These two features deserve attention although for different reasons. The line of research concerning currents, in particular the vertical ones, did not lead to significant results; but the negative result corroborated the Gaussian analysis that the Earth's permanent magnetic field depended on forces that admit a potential. If there are no vertical currents, the Gaussian hypothesis that admits a potential in the Earth's magnetic field was proved beyond any reasonable doubt.
The theories relating rotation and magnetism are, on the other hand, interesting because they form the scientific background of Larmor's article (1920), which inspired most of the modern ideas on the mechanism of generation of the Earth's magnetic field. Larmor considers three possibilities:
1 - In the case of the Sun, the surface phenomena indicate the existence of internal residual circulation especially in the meridian planes; This internal movement induces an electric field which under certain conditions will cause the circulation of an electric current. This current, in turn, will increase the inducing magnetic field. So it is possible, thanks to internal cyclic movements, to obtain a self-excitation dynamo and to maintain a permanent magnetic field starting from an initial minimum value, at the expense of the energy of the internal circulation;
2 - The gravitational force as a centrifugal force then implies an electric polarization which, due to the rotation, produces a magnetic field;
3 - A crystal possesses a permanent intrinsic polarization, since its polar molecules are oriented: if this natural orientation corresponds to an almost complete polarization, the electric field can be pretty high. If the crystal were as big as the Earth, it would produce an enormous effect, and its rotation

would produce a magnetic field.
After explaining the inconsistency of the (2) or (3) theories, Larmor believes that the (1) theory, which seemed reasonable in the case of the Sun, could also explain the variations of the magnetic field on the Earth, both the sudden and the gradual components.
In 1934, the mathematician Thomas George Cowling ($1906 - 1990$) showed that an axially symmetrical field, such as that of the Earth, could not have originated from a hydromagnetic dynamo. The Larmor hypothesis, therefore, seemed to lack the necessary requisites to be able to inspire constructive lines of research.
Subsequently, the extent of the consequences of Cowling's out-of-patron work took over research programs which led to the elaboration of what, is now considered the standard theory for terrestrial magnetism: the modern theory of the hydromagnetic dynamo.

1.5 The development of Spectroscopy

Maxwell's synthesis opened the way to methodologies for the study of magnetic fields based on the interaction between electromagnetic waves and matter. In fact-as we said at the beginning-atoms became real measuring instruments, allowing the use of fundamental physical quantities such as, for example, atomic spin. For this reason, we briefly describe here the progress in the main field of the light matter interaction, i.e. *Spectroscopy*.
Indeed, Spectroscopy-that is, the branch of physics based on the analysis of the spectra of light emitted or absorbed based on its wavelength-had Isaac Newton among its pioneers.
The interests of the English scientist were primarily aimed at solving the problem of refraction which distorted the images produced inside optical instruments. His research led him to conclude that when a beam of white light is refracted by a prism, it exhibits not one but many refractivities each associated with a different color.
These discoveries demonstrated-in an irrefutable way-that color did not consist of a modification of white light deriving from contact with matter and from the interaction with it, but was an immutable property intrinsic to the constitution of light itself.
In 1704 Newton published the "Opticks", a treatise on light and color that

represents the sum of the knowledge achieved at the time in the field of Optics; the work ended with sixteen "Queries", in which he hypothesized that the light was made up of a heterogeneous mixture of corpuscles which responded dynamically when stimulated by particular short-range optical forces and by certain active reactants: the phenomena of reflection, refraction and diffraction would all derive from the dispersion of the particles of a ray of light subjected to the action of such forces. Newton therefore came to the conclusion that-passing through a triangular prism-the rays of the different colors were refracted at a well determined angle, different for each color. The following decades were characterized by a lively ferment, as the analysis of light scattering had profitably added to the arsenal of strategies with which to proceed to fully determine the nature of light.

In this context, John Michell $(1724-1793)$ proposed the use of the prismatic analysis of star light to trace the physical constitution of the light source that emits it proved to be of particular interest.

In 1800 Frederick William Herschel $(1738-1822)$ discovered the infrared spectrum by projecting the solar spectrum onto the bulb of a thermometer and observing a large temperature rise beyond red, in a region where there is no visible radiation. Herschel's discovery was enthusiastically welcomed by natural philosopher Johann Wilhelm Ritter $(1776-1810)$ who, in order to demonstrate the opposite *duality* underlying any physical phenomenon, investigated the invisible radiation beyond the extremity violet spectrum, choosing to use as indicators-instead of thermometers-the effects of chemical reactions.

Ritter placed paper soaked in silver chloride in the path of a scattered solar ray and observed that, if the reducing action of violet rays was significant, this was even greater in the portion of the sheet just beyond the violet end of the spectrum.

In 1814 Joseph Von Fraunhofer $(1787-1826)$, a German optician who worked at a Bavarian glass factory known for producing lenses with virtually no internal irregularities, saw an opportunity to discover and eliminate the causes of chromatic aberration due to refraction.

The problem of the correction of chromatic aberration tormented the manufacturers of optical instruments forcing them to laborious empirical procedures in the combination of different lenses. Fraunhofer tried to obtain a monochromatic light through the production of colored flames; needing a fairly intense source, he fixed his attention on a yellow-orange line that was

present in the spectrum of all the flames. Since sunlight was evidently the strongest source at the time, he looked for the same line in the sunlight and to his surprise found a black line. Such an accurate analysis required an instrument for measuring the angle of refraction and therefore placed the prism in the center of a theodolite, that is, a telescope capable of moving on a graduated circle.

Furthermore, as an expert builder of experimental apparatus that he was, he perfected the gap to be placed between the source and the prism observing that this were supposed to be as thin as possible but that diffraction placed a limit on the reduction of the width.This device will form the basic structure of all spectrometers for many decades to come. With this instrument, Fraunhofer began to analyze the solar spectrum by identifying hundreds of other dark lines.

He also devised an alphabetic system for labeling some reference lines by assigning A to a line near the red end of the spectrum, the letter D to the pair of dark lines associated with the bright orange line he had observed in the spectrum of the flame, the one-line letter H near the violet end of the visible and the one-line letter I in the ultraviolet.

For decades, opticians had been forced to assemble near achromatic lens systems, using glasses with complementary dispersion properties, but the complex procedure was fraught with much trial and error. Fraunhofer went in search of a monochromatic light source to contain the number of variables involved. He observed that each colored flame produced a broad spectrum of colors, instead of the monochromatic signal he needed and his attention was drawn to a bright and well-defined orange line that seemed common to all the spectra of the flames.

In an attempt to locate a similar bright line in the sunlight, he collimated the light with a narrow slit parallel to the edges of the prism and observed the spectrum outside the prism with a telescope. A more accurate analysis allowed him to ascertain that the solar spectrum was interrupted by as many as 576 dark lines in the solar spectrum-which seemed attributable to the action of some absorption process-managing to accurately determine the relative positions of many of them.

Fraunhofer also introduced a change in the instrumental configuration used in prismatic analysis, which would have consequences for future research in this area. Instead of observing the spectrum with the naked eye, he placed a theodolite in the path of the refracted beam, thus creating an observation

and measuring instrument that was in fact the forerunner of the modern spectroscope.

Unfortunately, however, the ubiquity of Fraunhofer's D lines and the complexity of spectral characteristics remained an embarrassing conundrum for both optics professionals and theorists until more than four decades after the publication of his spectral maps.

Although scholars attributed the dark interruptions of the solar spectrum to the action of some absorption process, there was no agreement on the identification of the cause of it, and there was no physical theory capable of explaining its marked selectivity. Attempts to derive, from the set of experimental data, a coherent explanation about the presence and cause of the lines, proceeded through the search for monochromatic light sources, the analysis of the spectrum of sunlight transmitted through glasses and colored vapors and the study of flame spectra of various substances.

The interpretative schemes remained ineffective until it was possible to demonstrate, in a reproducible way, that a certain spectral scheme obtained in the laboratory was uniquely associated with a certain substance. Furthermore, in order for theorists to formulate similar principles, it was necessary to demonstrate with certainty the direct correspondence between the spectral patterns obtained in the laboratory and those of the Fraunhofer's lines. The crucial insight dates back to 1857 by Scotsman William Swan ($1818 - 1894$).

In hopes of unraveling the mechanisms which produce light other than sunlight, he observed the spectra of hydrocarbons placed in the colorless flame produced by a new laboratory burner, being attracted to the fact that the outer part of the lamp flame emanated colorful glows when it was crossed by corpuscles of matter. To determine the minimum amount of substance needed to produce a colored spectrum, he dissolved a small amount of common table salt in plenty of water and found that less than one millionth of a grain of salt ($64.8mg$) was able to color the flame bright yellow.

From this experience it emerged clearly that the spectroscopic analysis was an extremely sensitive method of analysis but, at the same time, it was necessary to ensure that the sample to be analyzed was completely homogeneous.

Drawing on these experiences, Robert Wilhelm Eberhard Bunsen ($1811 - 1899$) and Gustav Robert Kirchhoff ($1824 - 1887$) studied the light spectra of flames and sparks generated by highly purified samples of different salts. Their observations confirmed what physicists had long suspected: each individual metal, by burning, produced its own characteristic sequence of bright

spectral lines.
Conversely, they observed that when intense light passes through a cold cloud of vapor of the same substance, the usual rainbow of white light is interrupted by dark absorption lines, arranged in exactly the same way as that substance's characteristic spectral pattern. Continuing these experiments, Kirchhoff also made observations of the solar spectrum, concluding that the dark Fraunhofer lines in the solar spectrum existed due to the presence, in the incandescent atmosphere of the Sun, of the same substances which in the spectrum of the flame produce light lines in the same position. On October 20 1859 Kirchhoff presented the fruits of his work to the Berlin Academy, sparking off a heated controversy in the scientific community.
Some scholars wondered if the lines were not due to the absorption of sunlight by the Earth's atmosphere; others objected that the studies carried out on the spectra of known terrestrial elements were insufficient to draw definitive conclusions. Despite these reservations, the scientific community was in the majority willing to accept the idea of a physical link between the spectra of metals and the Fraunhofer lines in the solar spectrum.
The discovery, by means of spectroscopic methods, of three new elements (cesium, rubidium and thallium) greatly increased interest in the experimental value of spectral analysis capable of producing new information and promoting new discoveries.
The further evolution of Spectroscopy - which covers more than a hundred years of history - is one of the most interesting demonstrations of the dialectic between theory and experiment at the basis of scientific progress. This dialectic proceeds through the proposition of models to be compared with experimental measures which, in turn, undermine the existing models and lead to the search for further theoretical proposals.
Therefore, once ascertained that any substance, if inflamed, emitted colors characteristic of the substance itself and that one way to stimulate the emission of light from a gaseous substance is to make it pass through an electric spark, the Sweden Anders Jonas Ångstrom $(1814-1874)$, one of the founders of modern spectroscopy, measured the emission spectrum of hydrogen with great precision in 1852, finding four colors with respective wavelengths equal to 6562.852, 4861.33, 4340.47 and 4101.74 one hundred millionths of a centimeter. The lines - three in the visible and one in the near ultraviolet - corresponded to a red, a green, an indigo and a violet.
Based on the studies of Kirchhoff and Ångstrom, the Swiss mathematician

Johann Jakob Balmer ($1825 - 1898$) began the study of the emission and absorption spectra of gases, establishing the relationship between the frequencies of the lines in the spectrum of hydrogen. He discovered that it was possible to analytically represent the series of lines then known, in the visible (we speak of series since these lines thicken as their length decreases until they become an insoluble continuum). The wavelengths in the visible spectrum of the hydrogen atom satisfy the formula

$$\lambda = B\left(\frac{m^2}{m^2 - 2^2}\right) \tag{1.18}$$

where B is a constant and $m > 2$ an integer. Three years later, Johannes Rydberg (1854–1919) generalized Balmer's formula for all lines of the spectrum

$$\frac{1}{\lambda} = R\left(\frac{1}{n_1^2} - \frac{1}{n_2^2}\right) \tag{1.19}$$

where R is the Rydberg's constant, n_1 and n_2 integers, with $n_2 > n_1$; the constant R is an empirical constant and is worth approximately $1.097 \cdot 10^7 m^{-1}$. Other series of lines were discovered by Friedrich Paschen ($1865 - 1947$) in the infrared in 1908 and by Theodore Lyman ($1874 - 1954$) in the ultraviolet in 1906.

Rydberg's formula continued to be verified, obviously with the appropriate pairs of integers n for each row: Lyman's series had $n_1 = 1$, Balmer's $n_1 = 2$ and that Paschen's $n_1 = 3$; later other series were found, with n_1 greater but the formula continued to be verified.

It was evident that the phenomenon of the emission and absorption of light was electromagnetic in nature and, starting with the discovery of the electron by Joseph John Thomson ($1856 - 1940$) in 1898, it became increasingly accepted that the atom was formed by negative and positive particles and therefore able to interact with the electromagnetic field by absorbing and emitting energy, but it was not at all clear why this only occurred at very precise wavelengths and moreover dependent on integers.

Maxwell's equations, which govern all electromagnetic phenomena, were now a pillar of physics; they are continuous equations whose solutions necessarily give values capable of varying continuously and therefore cannot in any way give results in the discrete. However, the experiments gave indisputably discrete values and, moreover, a function of integers rationalized them perfectly: it was not an explanation of the phenomenon, but in any case the formula was correct.

The explanation was necessarily linked to the internal structure of the atom which, in the decades between the XIX and XX centuries, was losing the concept of an indivisible particle.

1.6 Radiation-matter Interaction

As previously mentioned, in 1859 Gustav Kirchhoff studied a system in thermal equilibrium at the temperature T with the radiation which surrounds it. The system had to convert all the energy it absorbed into thermal energy. He defined the emissive power and the absorbing power as the quantity of energy emitted or absorbed per surface unit and per time unit in a given infinitesimal range of frequencies. An analytical function was expected that also depended on typical body features; on the contrary, he obtained an universal function depending on frequency and temperature only.
Following this discovery, Kirchhoff introduced the definition of an ideal black body to indicate a body that completely absorbed the incident radiation; in this way, an ideal black body had an emissive power equal to the function he previously conjectured and the problem consisted precisely in determining this function.
In the following years, many physicists tried their hand at solving this question, but without success. We recall that in those years the electromagnetic theory was not yet complete and there were also problems in creating experimental equipment which reproduced the ideality required for the black body. Taking up the definition given by Kirchhoff years earlier, in 1884 it was discovered that a very small hole in a cavity with walls at a homogeneous temperature and which did not allow the passage of radiation, then the radiation emitted by the hole was a black body radiation.
In 1900 Max Planck ($1858-1947$), based on the work of some of his predecessors such as Ludwig Boltzmann ($1844-1906$) and Wilhelm Wien ($1864-1928$), formulated a theoretical hypothesis in which radiation is schematized as harmonic oscillators: the energy, absorbed or emitted by the hypothetical matter oscillators constituting the wall, instead of being infinitely divisible, can be decomposed into a number of elements determined by the natural constant $\hbar$.
Planck's work not only solved the black body problem but was important for a variety of reasons: the constant he introduced changed the way of un-

derstanding phase space. From a precise description we passed to a space composed of cells of well-defined volume.
Furthermore, through the use of the energy quantum, he formulated the first discretization of energy, a quantity which until then had always been considered continuous.
Note that Planck's constant has the dimensions of an action, hence the name quantum of action, and that this is in agreement both with the position-by-moment product relative to the phase space and with the energy-time product used in the definition of the quantum of energy. Thus a completely revolutionary process of discretization and quantization of physics began leading to the birth of the old quantum theory first and then of quantum mechanics.
In 1905, the Annus Mirabilis of physics, Albert Einstein $(1979 - 1955)$ published six works within seven months, including an article explaining the photoelectric effect that had been discovered in the previous century by Heinrich Rudolf Hertz $(1856-1894)$. This effect involves the emission of electrons from a metal surface when an electromagnetic wave of "high enough" frequency was affected; subsequently Philipp Eduard Anton von Lenard $(1862 - 1947)$ had learned that the energy of the electron emitted in the procedure did not depend on the intensity of the wave, as one would classically expect, but only on the frequency.
Einstein was able to explain the photoelectric effect based on the composition of the electromagnetic radiation of discrete quanta of energy, according to the concept hypothesized by Planck. In practice, he generalized the idea of quantizing energy to the electromagnetic field and not only to the radiation emitted or absorbed by the hypothetical oscillators of the cavity walls.
If the energy in an electromagnetic beam is no longer uniformly distributed, but is concentrated in small regions of space, then the phenomenon can be analyzed as a collision between photons, quanta of light of energy $h\nu$, and the electrons of the metal surface. This explains both the very short time with which the photoelectric effect occurs, and why the electrons emitted following the impact have energy proportional to the frequency.
Einstein's proposal according to which light was composed of very small particles found new confirmations thanks to new experimental evidences; among these, the Arthur Compton's effect $(1892 - 1962)$ proved the idea of a light particle-matter particle collision, in which the photon, although without a mass, transfers a fraction of his energy to the electron by changing its trajectory.

After the impact, therefore, the photon, having lost energy, is described with a new frequency and wavelength, different from the initial one.
The beginning of the XX century was therefore characterized by the coexistence of two theories as regards electromagnetic phenomena: in some cases a wave description was convenient while in other ones a particle framework seems necessary. This raised doubts on the fact that the vice versa was also possible, that is, also matter in specific situations could manifest a wave behavior.
The scientific community was torn as to what the atomic structure was: within two decades, numerous models were developed to explain the hardness of atoms.
There have been several pre-quantum atomic models, many more than we commonly remember; some of them contained innovative scientific intuitions. Today those “erroneous” models are revived in fresh physical theories.
For further details, the Appendix 1 describes ”winning” and ”loser” models, while here we will limit ourselves to analyze the works of Thomson, Ernest Rutherford I Baron o Nelson ($1871 - 1937$) and Niels Bohr ($1885 - 1962$).

1.6.1 Atomic models-Thomson and Rutherford

Thomson performed his experiments using cathode rays, beams of negatively charged particles. These are produced by means of vacuum glass tubes, in which two electrodes, an anode and a cathode are positioned. By applying a high voltage, an invisible radiation is emitted which is directed to the opposite electrode.
The detection apparatus consists of a wall coated with a fluorescent material which, once hit by the radiation, emits an intense brightness. If a solid object obstructs the cathode rays, it casts a shadow on the tube wall.
In practice it is evident that the rays travel in a straight line and that they can be easily blocked. By means of these observations, Thomson postulated the existence of subatomic particles. At that time, this atomic model could fully explain the behavior of chemicals. However, it should be kept in mind that Thomson did not actually call his particles ”*electrons*”, although the term was previously coined by George Johnstone Stoney ($1826 - 1911$).
It is relevant to point out at the time, the other two fundamental particles, the proton and the neutron, had not yet been discovered. It seemed plausible that the positive charge in the atom was distributed in it not in the form of

a carrier particle.
Another important detail is that only in 1906 Robert Andrews Millikan $(1868-1953)$ was able to determine the exact values of the charges of protons and electrons.
Experimentally, Thomson postulated an atomic structure with the following characteristics:
- The atom is an electrically neutral solid sphere, with an approximate radius of $10^{-10}m$;
- The positive charge is distributed more or less uniformly throughout the sphere;
- The atom contains negatively charged "*corpuscles*", which guarantee its neutrality;
- These corpuscles are the same for all matter;
- When the atom is in equilibrium, there are n corpuscles regularly arranged within the positively charged sphere;
- The mass of the atom is uniformly distributed;
- Most important, Thomson "pancake" satisfies the fundamental request coming from experimental observations: the existence of well defined discrete lines in the atomic spectra. This is the signature of a resonance phenomenon, associated to a harmonic oscillating dipole: the uniform positive charge distribution is ideal for creating a restoring force, mimicking a mass-spring interaction,
In a short time the model was found manifestly incorrect, as a result of the Rutherford's diffusion experiments.
In 1909, Rutherford, together with his assistants Johannes Hans Wilhelm Geiger $(1882-1945)$ and Ernest Marsden $(1889-1970)$, devised an experiment destined to change the history of nuclear physics forever. In the collision of a beam of Helium nuclei with a thin slice of gold, the projectiles were deflected at angles much greater than expected; a few particles were even repelled backwards. If Thomson's model was correct, the α particles would have had to cross the foil almost undisturbed by virtue of their mass far greater than that of the electrons they would have encountered.
The interpretation that Rutherford gave to this experiment was that the definition of a model in which the atom was constituted by a nucleus of positive charge, where the entire mass was concentrated, and by an adequate number of electrons to make the system neutral. By calculating the cross section, he found that the dimensions of the nucleus were five orders of magnitude

lower than those of the entire atom; this meant that most of the volume of an atom is empty.
This model was not stable because electrons accelerated in motion would classically emit radiation with the consequence that they would spiral towards the nucleus, collapsing in a short time. Therefore, no classical model can satisfactorily give an image of the atom and explain the stability of matter.

1.6.2 Bohr's model

In 1921 the most advanced quantum theory was the Bohr's model. Bohr qualitatively "solved" the energy loss dilemma by assuming that electrons can orbit on circular trajectories on which they do not emit radiation; the radiation is due to the passage of an electron from a stationary state with higher energy to one with lower energy only.
The excitation of an electron by a photon of suitable energy causes transitions towards an excited state, that is, towards an outermost orbit. In the transition from an outermost to an innermost orbit, on the other hand, a de-excitation occurs and the atom loses energy, yielding it to a photon generated in the transition and emitting radiation.
Bohr's postulates are as follows:
1 - An atom cannot assume all the classically possible energy values, but only a series of discrete values $E_1, E_2, ...E_n$;
2 - The states corresponding to these energies are stationary so there is no emission of electromagnetic radiation;
3 - The emission or absorption occurs only in the transition of the atom from one stationary state to another.
In this case, photons of energy equal to will be emitted or absorbed

$$h\nu = E_n - E_m \tag{1.20}$$

4 - The correspondence principle is established, i.e. the result of a quantum theory is as close to the classical result as higher the quantum number.
The great merit of this model was that of giving a theoretical foundation to Balmer's experimental results, subsequently expanded by Rydberg, on the spectrum of the hydrogen atom. Let's recall the formula obtained in 1884 by Balmer, which allowed to calculate some lines of the emission spectrum

of the hydrogen atom

$$\lambda = (364.6nm)\frac{n^2}{n^2-4} \tag{1.21}$$

and its generalization, that is, the empirical law of Rydberg-Ritz

$$\nu = R_H\left(\frac{1}{n^2} - \frac{1}{m^2}\right) \tag{1.22}$$

If we analyze this formula in the light of Bohr's first two postulates, we can identify the energy values of the atomic states with those of the spectral terms multiplied by hc. Once this is done we get

$$h\nu = R_H hc\left(\frac{1}{n^2} - \frac{1}{m^2}\right) \tag{1.23}$$

which, compared with the previous expression of the energy of the emitted or absorbed photon, returns

$$E_n = -\frac{R_H hc}{n^2} \tag{1.24}$$

where $n = 1, 2, ...$

This explains the series in the emission spectrum of the hydrogen atom: the lines of a given series correspond to the energy emitted in the transition from energy states E_m towards the same energy state E_n with $E_m > E_n$.

Using Bohr's first three postulates it is possible to relate the spectral terms with the energy levels. With the fourth postulate it is also possible to derive, with only theoretical considerations, an expression of the Rydberg constant whose numerical value perfectly reproduces the experimental data. As previously mentioned, the quantum result approaches the classical one as the quantum number increases and therefore, in our case, for $n \to \infty$.

For very large n the energy levels are very close, so we can approximate the energy of the photon created in the $E_n \to E_m$ transition with that of a $E_n \to E_{n-1}$ transition. With this assumption, the expression of the transition frequency will be

$$\nu_q = R_H c\left(\frac{1}{(n-1)^2} - \frac{1}{n^2}\right) = R_H c\frac{2n-1}{n^2(n-1)^2} \tag{1.25}$$

Then remembering that $n \to \infty$ we can rewrite it as

$$\nu_q = \frac{2R_H c}{n^3} \tag{1.26}$$

Finally, remembering the expression of E_n, we will have

$$\nu_q = 2\sqrt{\frac{|E|^3}{h^3 c R_H}} \tag{1.27}$$

From the classical point of view, the electron is subject to the Coulomb attraction of the nucleus with a force in modulus equal to

$$F = k\frac{q_c^2}{r^2} \tag{1.28}$$

Knowing that the centripetal acceleration is $a_c = v^2/r$, using the fundamental law of dynamics we will have that

$$m\frac{v^2}{r} = F = k\frac{q_e^2}{r^2} \tag{1.29}$$

from which it can be derived

$$v = \sqrt{\frac{kq_e^2}{mr}} \tag{1.30}$$

Substituting in the formula of the energy of the system

$$E = \frac{1}{2}mv^2 - k\frac{q_e^2}{r} \tag{1.31}$$

you get that

$$E = -k\frac{q_2^2}{2r} \tag{1.32}$$

hence $r = kq2e/2|E|$. Recalling that the frequency in a uniform circular motion is given by $\nu_c = \omega/2\pi$, we will obtain, for the frequency calculated classically

$$\nu_c = \frac{q_e}{2\pi}\sqrt{\frac{k}{mr^3}} = \frac{1}{\pi q_e^2}\sqrt{\frac{2|E|^3}{mk^2}} \tag{1.33}$$

Using at this point the fourth postulate, namely that the quantum result must coincide with the classical one as the quantum number increases, we can equate the two expressions. By replacing the expression of $k = 1/(4\pi\epsilon_0)$ we get

$$R_H = \frac{qe^4 m}{8\epsilon_0^2 h^3 c} \tag{1.34}$$

Substituting the numerical values of the constants, we find that R_H is worth 109661.28 cm^{-1} and for the experimental ones 109677.28 cm^{-1}.
According to Bohr, since the experimental data are detected by macroscopic

apparatuses described by classical laws, the description of quantum objects must also use the language of classical physics, so he hypothesized that in stationary states the electrons obeyed Newtonian mechanics. The rays of the orbits, which represent the energies allowed to electrons, are quantized

$$r_n = n^2 \frac{h^2}{4k\pi^2 m q_e^2} \tag{1.35}$$

These orbits depend on the value of the so-called principal quantum number n on which the energy value of the allowed orbits also depends. The quantized speed

$$v_n = \frac{q_e^2 k}{n\hbar} \tag{1.36}$$

with $\hbar = h/2\pi$. For the angular moment we have

$$L = m v_n r_n = \hbar n \tag{1.37}$$

The results of this model can also be extended to hydrogen atoms.

1.6.3 Sommerfeld's corrections

The model described so far is unsuitable for representing the data inherent in the spectroscopic behavior of multi electron atoms, starting with helium. In fact, it can be observed that, in the helium spectrum, there are lines not foreseen by the Bohr's model.

In addition, advances in the field of high-resolution spectroscopy led to the discovery of the fine structure: the lines of the emission spectrum of atoms such as hydrogen were not single, as predicted by Bohr's theory, but were actually made up of several lines with very tight spacing.

The following calculus is reported in countless scientific textbooks.

In 1915 Arnold Sommerfeld $(1871 - 1937)$ modified Bohr's planetary model by introducing elliptical orbits in which the nucleus occupies one of the two foci. According to his hypotheses, while in the first level the electron can only travel a circular orbit, in the second level it can also travel an elliptical orbit whose major axis size coincides with the diameter of the circular orbit. There are two variables to consider:

1 - The distance of the electron from the nucleus;

2 - The variation of the angular position, in the plane of the orbit, of the electron with respect to the nucleus. Sommerfeld then introduced two quantum numbers:

1 - The quantum number n_0, called the principal quantum number, derived from Bohr's theory, which is related to the size of the major axis of the orbit;
2 - The orbital quantum number l, which is related to the dimension of the minor axis of the orbit and therefore characterizes the geometry of the orbital, assuming the values $l = 0, 1, ..., n' - 1$. According to this model, for each principal quantum number n' there are n' possible orbits of variable eccentricity. Since the eccentricity of an ellipse is given by

$$e = \sqrt{1 - \left(\frac{b}{a}\right)^2} \tag{1.38}$$

with a, b semimajor and semiminor axis lengths, respectively. The eccentricity will depend on

$$\frac{b}{a} = \frac{l+1}{n'} \tag{1.39}$$

It can therefore be noted that, among these orbits, one is circular while the other $n' - 1$ are elliptical. The orbits had to be quantized also with regard to their spatial orientation in relation to a certain coordinate system.
Sommerfeld then postulated the existence of a third quantum number n, the space quantum number, and further differentiated it into n_1 and n_2 in order to satisfy the condition

$$n_1 + n_2 = n \tag{1.40}$$

For $n = 1$ there are only two positions of the orbital planes, the one perpendicular ($n_1 = 0$, $n_2 = 1$) and the one parallel ($n_1 = 1$, $n_2 = 0$) to the equatorial plane. With arbitrary n, the number of quantized positions is $2n$; always including parallel and perpendicular positions. This phenomenon of quantization of the orbital planes of the electron-the *Richtungsquantelung*- is normally translated as "crushing of the orbit".
Sommerfeld calculated the relationship between the speed of the electron on the first orbit of the Bohr atom and the speed of light in vacuum,

$$\alpha = \frac{{q_e}^2}{4\pi\epsilon_0\hbar c} \simeq \frac{1}{137} \tag{1.41}$$

which is defined as a fine structure constant.
The energy correction of the levels of the hydrogen atoms appears to be

$$E = -\frac{mZ^2q_e^4}{(4\pi\epsilon_0)2n^2\hbar^2}\left[1 + \frac{\alpha^2Z^2}{n}\left(\frac{1}{l+1} - \frac{3}{4n}\right)\right] \tag{1.42}$$

Sommerfeld also introduced relativistic corrections in the Bohr model by virtue of the fact that the speed of the electron in its orbital motion is not

so close to the velocity of light, but for precise spectroscopy measurements we also need to take into account special relativity. Furthermore, when the electron is in an elliptical orbit, it will have a higher speed when it is closer to the nucleus and a slower speed when it is further away.
From the relativistic formula of energy

$$E = \sqrt{p^2c^2 + m_0^3c^2} \tag{1.43}$$

with $p = \gamma m_0 v$ it can be understood how elliptical orbits with different eccentricity have energy values slightly different from those of the circular orbit of the level they belong to. Consequently, in the energy correction of the levels there is an explicit dependence on l which takes into account the ellipticity of the orbits. This modification to the model partially manages to explain the fine structure of the spectral lines, but it also has its problems.
In fact, if we consider alkali metals we would expect that the electron responsible for the shape of the spectrum must move on a high radius orbit at low speed and therefore the relativistic variation of the mass is small. However, the splitting due to the fine structure was found to be greater than that of hydrogen, which raised doubts about the validity of Sommerfeld's explanation of the fine structure.
Furthermore, the Bohr-Sommerfeld's model does not solve another problem, that of the so-called anomalous Zeeman's effect.

1.6.4 Zeeman's effect

This effect was first observed in 1896 by Pieter Zeeman ($1865-1943$) who was performing experiments on the effects of an external magnetic field applied to emitting matter: observing the radiation which comes from a discharge lamp, it can be observed that a spectral line, in the simplest case, separates into three components. If ν_0 is the central resonance frequency of the unperturbed line, the three components will have frequencies respectively equal to $\nu_0 - \nu_L$, ν_0 and $\nu_0 + \nu_L$, where ν_L has been calculated by Joseph Larmor ($1857-1942$)

$$\nu_L = \frac{q_e B}{4\pi mc} = 1.3996 \cdot 10^{-6} BHz \tag{1.44}$$

where B indicates the magnetic field intensity in Gauss units.
The polarization of the emitted light varies depending on the direction of observation: the radiation emitted along the direction of the field gives rise to two lines, circularly polarized, one with right polarization and the other

with left polarization, with the disappearance of the central component; the radiation emitted perpendicularly to the field gives rise to three linearly polarized lines, of which the central one is polarized in the direction of the field and the lateral ones are polarized in the perpendicular direction. This phenomenon occurs because electrons are charged particles confined in energy levels characterized by a quantum number of angular momentum; they also have a semi-integer spin angular momentum and therefore a magnetic moment which interacts with the external magnetic field oriented along, for example, the z axis. The interaction can be described by adding a perturbative term to the system's Hamiltonian. This Thesis is focused on atomic magnetometers, so we will consider only the electronic moments.
In a multielectron atom, we can indicate with $\mathbf{L}$ the orbital angular momentum operator, with $\mathbf{S}$ the angular momentum of spin operator and with $\mathbf{J} = \mathbf{L} + \mathbf{S}$ the total angular momentum operator. We now distinguish two cases:
1 - The singlet case ($\mathbf{S} = 0$). In this situation we will have that the total angular momentum $\mathbf{J}$ coincides with the orbital angular momentum $\mathbf{L}$. In analogy to the classical case we can define a magnetic moment operator

$$\mu_L = -\frac{\mu_B}{\hbar}\mathbf{L_z} \tag{1.45}$$

where μ_B indicates the Bohr's magneton. The interaction will therefore be

$$E = -\mu \cdot \mathbf{B} \tag{1.46}$$

we will have that the perturbative term to be added to the Hamiltonian is

$$H^1 = -\frac{\mu_\mathbf{B}}{\hbar} \cdot \mathbf{L_z} B \tag{1.47}$$

with separation between the levels equal to

$$H^1 = -\frac{\mu_B}{\hbar}\mathbf{L_z} \tag{1.48}$$

with m_l eigenvalues of L_z. Since we have $2l+1$ values of m_l, each spectral line will split into $2l + 1$ lines. This phenomenon is called the normal Zeeman's effect.
2 - In case $S \neq 0$ things get complicated due to the presence of the spin. Assuming that the atom has angular momentum L and spin S, the total angular momentum will be

$$\mathbf{J} = \mathbf{L} + \mathbf{S} \tag{1.49}$$

and the operator associated with the magnetic moment will have to be modified

$$\mu = -g_l \mu_B \frac{\mathbf{L}}{\hbar} - g_s \mu_B \frac{\mathbf{S}}{\hbar} \tag{1.50}$$

where g_l is the gyromagnetic factor relating to the angular momentum and g_s is the gyromagnetic factor relating to the spin.

1.6.4.1 The classical interpretation

Let's quantitatively discuss Thomson's model, with the correction given by Hendrick Antoon Lorentz $(1853-1928)$, and let us apply it to the Zeeman's effect. To explain the emission of a line at a frequency ν_0, it is assumed that the elastic constant is such as to give an oscillator resonance frequency equal to ν_0.

Let x be the coordinate of the charge; in the absence of external perturbations we have

$$\frac{d^2\mathbf{x}}{dt^2} = -4\pi^2 \nu_0^2 \mathbf{x} \tag{1.51}$$

By introducing a magnetic field, the equation is changed due to the presence of the Lorentz's force.

Using an electron of mass m as an oscillating charge and a charge $-|e|$ we obtain:

$$\frac{d^2\mathbf{x}}{dt^2} = -4\pi^2 \nu_0^2 \mathbf{x} - \frac{|e|\mathbf{v}}{m} \times \mathbf{B} \tag{1.52}$$

If we decompose the vector $\mathbf{x}$ into its Cartesian components, we will obtain coupled differential equations, so it is convenient to consider the components of $\mathbf{x}$ on the three directions identified by the versors $\mathbf{u}_{-1}$, $\mathbf{u}_0$, $\mathbf{u}_1$

$$\mathbf{u}_{-1} = \frac{1}{\sqrt{2}}(\mathbf{i} + i\mathbf{j}) \tag{1.53}$$

$$\mathbf{u}_0 = \mathbf{k} \tag{1.54}$$

$$\mathbf{u}_1 = \frac{1}{\sqrt{2}}(-\mathbf{i} + i\mathbf{j}) \tag{1.55}$$

where $(\mathbf{i}, \mathbf{j}, \mathbf{k})$ are the versors of an orthogonal Cartesian triple and $\mathbf{k}$ is the direction of the magnetic field. Thus placing $\mathbf{x} = \sum_\alpha x_\alpha \mathbf{x}_\alpha$ and observing that

$$\mathbf{u}_\alpha \times \mathbf{B} = B\mathbf{u}_\alpha \times \mathbf{u_0} = -iB_\alpha \mathbf{u}_\alpha \tag{1.56}$$

with $(\alpha = -1, 0, 1)$ the decoupled equations are obtained

$$\frac{d^2 x_\alpha}{dt^2} = -4\pi^2 \nu_0^2 x_\alpha + 4\pi i \alpha \nu_L \frac{dx_\alpha}{dt} \tag{1.57}$$

where $\nu_L = \frac{q_e B}{4\pi mc}$ is the Larmor frequency. Looking for the solution in the form

$$x_\alpha = A_\alpha e^{-2\pi\nu_\alpha t} \tag{1.58}$$

with A_α constant, you get a second degree algebraic equation for ν_α

$$\nu_\alpha^2 + 2\alpha\nu_\alpha\nu_L - \alpha\nu_0^2 = 0 \tag{1.59}$$

Experimentally, $\nu_L \ll \nu_0$ is obtained

$$\nu_\alpha = \nu_0 - \alpha\nu_L \tag{1.60}$$

Under the action of a magnetic field, three distinct oscillators are obtained having frequencies ν_0, ν_0-ν_L, ν_0+ν_L.

1.6.4.2 Quantum treatement of Zeeman's effect

In hydrogen-like atoms the energy of the electron E_n can be quantized in discrete orbits and the angular momentum of the electron $\mathbf{p}$ is equally quantized. Assuming to introduce a privileged direction into space, for example through a magnetic field, the orbital angular momentum vector can assume only certain orientations with respect to it. The $\mathbf{p}$ component along the axis introduced can only assume discrete values. The Hamiltonian of a hydrogen-like atom is given by

$$H = -\frac{\hbar}{22m - \frac{e^2}{4\pi\varepsilon_0 r}} \tag{1.61}$$

In spherical polar coordinates, the Laplacian results

$$\nabla^2 = \frac{1}{r^2 \sin\vartheta}\left[\sin\vartheta\frac{\partial}{\partial}\left(r^2\frac{\partial}{\partial r}\right) + \frac{\partial}{\partial\vartheta}\left(\sin\vartheta\frac{\partial}{\partial\vartheta}\right) + \frac{1}{\sin\phi}\frac{\partial^2}{\partial^2}\right] \tag{1.62}$$

The Hamiltonian has, as solutions, standing wave functions that can be factored into a radial and an angular part

$$\Psi(r,\vartheta,\phi) = R_{n,l}(r)Y_{l,m_l}(\vartheta,\phi) \tag{1.63}$$

where n is the principal quantum number, l is the quantum number associated with the discrete values of the orbital angular momentum and m_l is the quantum number associated with the spatial quantization of l. It is possible to further factor the angular part of the wave function

$$Y_{lm_l}(\vartheta\phi) = (2\pi)^{-1/2}\Phi_{lm_l}e^{im_\phi} \tag{1.64}$$

The solution of the Schrödinger equation for the radial part is calculated using particular functions obtained by the mathematician Edmond Nicolas Laguerre $(1834 - 1886)$

$$P_l = [l(l+1)]^{1/2}\hbar \tag{1.65}$$

with $l = 0, 1, 2, ..., (n-1)$.
The quantized value of the orbital angular momentum is given by

$$(P_l)_z = m_l\hbar \tag{1.66}$$

where $m_l = 0, \pm 1, \pm 2, ..., \pm l$. By introducing a spatial quantization axis for the angular momentum, for example along the axis z, the vector P having P_l, can only assume the orientations such that the component $(P_l)_z$ along l quantization axis becomes

$$P_s = [s(s+1)]^{1/2}\hbar \tag{1.67}$$

with $s = 1/2$ and

$$(P_s)_z = m_s\hbar \tag{1.68}$$

where $m_s = \pm 1/2$.
Sommerfeld, in 1916, developed a quantum model of the Zeeman's effect for one-electron atoms in which, by solving the equation of motion of an electron in a magnetic field, the frequencies of the hydrogen spectral lines had shifted by an amount equal to

$$\Delta\nu = \frac{f}{4\pi}\Delta n \tag{1.69}$$

where is

$$f = \frac{q_e}{m_e c}|\mathbf{B}| \tag{1.70}$$

and Δn denotes the difference between the spatial quantum numbers in the initial and final state, respectively. It follows, therefore, that we will always find ourselves in the presence of a splitting in an odd number of lines. However, while the Zeeman's effect in some atoms shows an equally spaced triplet, in other atoms the magnetic field separates the spectral lines and some triplets show a wider spacing than expected.
This phenomenon, called the anomalous Zeeman's effect, was thus explained by Sommerfeld:
1 - The singlet lines of hydrogen atoms show a normal Zeeman's effect, while their triplet lines approach it for very intense magnetic fields;

2 - In low-intensity magnetic fields the spectral doublets and triplets of non-hydrogenic atoms show an anomalous Zeeman's effect.
Sommerfeld's conjecture was that it is the outermost electrons of the atom that determine the character of the Zeeman's effect and in particular their magnetic fields as long as they are kept lower than the external magnetic field.

1.6.5 The introduction of spin

In 1925, Samuel Abraham Goudsmit (1902 – 1978) and George Eugene Uhlenbeck (1900 – 1988) proposed that the electron had an intrinsic angular momentum and a magnetic dipole moment, whose z components are specified by a fourth quantum number, called m_s, which can only take values $\pm 1/2$.
The splitting of atomic energy levels would thus be due to the orientation energy of the magnetic dipole in the magnetic field present inside the atom, which is due to the fact that the latter contains moving charges. The energy would therefore, being dependent on the sign of m_s, positive or negative based on the orientation of the spin ("*up*" or "*down*") with respect to the direction of the magnetic field inside the atom.
The idea that the electron was endowed with an intrinsic angular momentum was not introduced by Goudsmit and Uhlenbeck, but appears for the first time in Arthur Compton's work of 1921, in which he ends by writing: "I can therefore conclude that the electron itself, spinning like a small gyroscope, is probably the ultimate magnetic particle." The idea originated precisely from Pauli's work on the exclusion principle, in which he proposed the use of four quantum numbers for the electron.
However, the description was of a formal nature and seemed to have no connections with anything concrete: given that the electron is considered point-like, and each quantum number is associated with a degree of freedom, it is difficult to imagine a fourth.
The idea of Goudsmit and Uhlenbeck was that the fourth degree of freedom was linked to the rotation of the electron on itself. The idea of an angular momentum intrinsic to the electron presents many problems:
1 - The speed of rotation on the surface of the electron should be equal to many times that of light;
2 - According to the calculations of Lorentz, to which Goudsmit and Uh-

lenbeck had turned, the magnetic energy would be so great that, using the equivalence between mass and energy, the electron would have a mass greater than that of the proton. The problem of what spin is dramatically arose: classically, three degrees of freedom are allowed but it was not possible to describe all the properties of the electron using classical mechanics.
On the other hand, quantum mechanics based on the Schroedinger equation does not predict spin, but this is compatible with the theory; instead, in relativistic quantum mechanics developed by Dirac, spin was a product of the theory.
Another aspect of the non-classical character of spin can be seen from the fact that the quantum number $\mathbf{s}$, which specifies the amplitude of the angular momentum of spin $\mathbf{S}$, can only take values $\pm 1/2$ and it is therefore not possible to bring $\mathbf{S}$ to its classic limit by making $s \to \infty$ as it is possible to do for the amplitude of the orbital angular momentum. In formulas

$$\mu_{\mathbf{s}} = g_s \mu_B \mathbf{S} \tag{1.71}$$

.

1.6.5.1 Stern-Gerlach's experiment

To arrive at a complete theory of the Zeeman's effect in the case of non-hydrogen-like atoms, it was necessary to understand the reason for the multiplicity of spectral lines. These questions prompted two young researchers, Otto Stern $(1889 - 1969)$ and Walther Gerlach $(1889 - 1979)$ to conceive a famous experiment.
A bundle of silver atoms which heated in an oven with a small slit, was passed through a collimator and finally exposed to the action of a magnetic field. This magnetic field was directed along the $\widehat{z}$ axis and not uniform with respect to the variations referred to z.

$$\frac{\partial B_z}{\partial x} = 0; \tag{1.72}$$

$$\frac{\partial B_z}{\partial y} = 0; \tag{1.73}$$

$$\frac{\partial B_z}{\partial z} \neq 0. \tag{1.74}$$

The silver atom-composed of a nucleus and 47 electrons-was modeled as an asymmetric electron cloud with no overall angular momentum and an "isolated" electron in the $5S$ orbital. The angular momentum of the entire atom

depends only on the spin of this single electron.
The following relationship gives proportionality between the magnetic moment of the atom μ and the spin moment of the electron

$$\mu_{\mathbf{S}} = \frac{q_e}{mc}\mathbf{S} \tag{1.75}$$

The interaction energy of the magnetic moment of each atom with the magnetic field in action can be expressed as $\propto -\mu{\cdot}\mathbf{B}$ therefore the long component z of the reaching force at which the atom is subject itself can be written as

$$F_z = \frac{\partial}{\partial z}(\mu \cdot \mathbf{B}) \simeq \mu_z \frac{\partial B_z}{\partial z} \tag{1.76}$$

If we assimilated the atom is the forty-seventh electron to a classical magnetic dipole, it would be possible to predict the extremes of the range of values that the average magnetic moment can assume

$$-\frac{q_e}{2mc}|\mathbf{L}| \leq \overline{\mu} \leq \frac{q_e}{2mc}|\mathbf{L}| \tag{1.77}$$

It was obviously necessary to suppose that the apparatus was able to measure the component of $\mathbf{S}$ up to a factor of proportionality.
On the basis of the classical theory, a continuous band should have appeared to the detector while it was noticed that the atomic beam was splitting into two distinct components, without there being a continuous distribution of beams emerging from the device. In practice, a spatial quantization of the angular momentum of spin was carried out, for which only two were the possible values

$$S_{z+} = \frac{\hbar}{2} \tag{1.78}$$

$$S_{z-} = -\frac{\hbar}{2} \tag{1.79}$$

The relation which expresses the quantization of the angular momentum of the electron spin can be written more compactly

$$\mathbf{S} = \frac{\hbar}{2}\sigma \tag{1.80}$$

where σ are Wolfgang Ernst Pauli's matrices $(1900 - 1958)$

$$\sigma_x = \begin{pmatrix} 0 & 1 \\ 1 & 0 \end{pmatrix} \tag{1.81}$$

$$\sigma_y = \begin{pmatrix} 0 & -j \\ j & 0 \end{pmatrix} \tag{1.82}$$

$$\sigma_z = \begin{pmatrix} 1 & 0 \\ 0 & -1 \end{pmatrix} \tag{1.83}$$

It might be thought that the introduction of the spin hypothesis immediately led to a reinterpretation of the experiment: this did not happen until 1927, the year in which J. Fraser discovered that the orbital angular momentum in the fundamental state, and therefore the associated magnetic moment, for silver, hydrogen and sodium is zero.
In the same year, Thomas Erwin Phypps and J.B. Taylor reproduced the Stern and Gerlach experiment with hydrogen atoms in the ground state, obtaining the same results and consequently generalizing the theories about electronic spin to atoms other than those of silver that had been used by Stern and Gerlach [120], [119]. See Appendix 2 for details.

1.6.6 Magnetic Resonance

At the base of any atomic magnetometer is the physical phenomenon of magnetic resonance. Observation of magnetic resonances in atoms can be performed by means of many different spectroscopic techniques exploring the interaction of electronic or nuclear angular momenta, with each other and with the external magnetic field.
The first experiment demonstrating high resolution spectroscopy of atomic magnetic resonance was made by Isidor Isaac Rabi (1898 – 1988) in 1938 [124], who investigated a $LiCl$ molecular beam crossing a magnetic field sufficiently strong to decouple completely the nuclear spins from one another and from the molecular rotation. The beam was spatially spread by an inhomogeneous magnetic field and then refocused by a second inhomogeneous field of opposite sign. A detector was placed in the focal point and the beam intensity was monitored.
The notable discovery was that a small radio frequency magnetic field, applied perpendicularly to the static one, produced sharp variation in the beam intensity, in correspondance of the frequencies precession of the particular angular momenta of atoms. The narrow resonance profiles provided for extremely accurate determination of the precession frequencies of Cl and Li.
Rabi probed the hidden interaction between molecular components and magnetic field with the right wavelength radiation while detecting the much stronger signal produced in that particular case by the variation of the beam intensity. Rabi's technique is still at the base of High Sensitive Atomic Mag-

netometry [52].

First realizations of high-resolution magnetic resonance spectroscopy in the optical domain were based on the phenomenon of optical pumping in alkali atomic species [50], [53].

In Optical Pumping, by polarized light near-resonant with an optical transition, a long-lived magnetization of the atomic medium is induced. We use the Larmor's precession frequency ω of atomic spins in a magnetic field $\mathbf{B}$ given by

$$\omega_L = \gamma|\mathbf{B}| \tag{1.84}$$

where the gyromagnetic ratio γ serves as the conversion factor between the frequency and the field strength. This technique will be studied in depth in Chapter 3.

Chapter 2

Applied Magnetometry: a brief history

We will now introduce a description of most used instruments for measuring magnetic fields. The first ones, following the flow of time, are *inclinometers* and *declinometers*, which have found wide applications in the measurement of the Earth's magnetic field.
Only later, during the XIX century, did the use of magnetometers spread, in both research and industry.

2.1 Declinometers

Among the most ancient scientific instruments, deriving directly from the compass, there are the declinometers used to measure the *magnetic declination*, i.e. the angle formed in the horizontal plane between the direction of the horizontal component of the Earth's magnetic field and the geographic meridian which passes through it.
A declinometer consists of a needle resting on a pin or suspended by a thread, which is left free to rotate in a horizontal plane around a vertical axis. Often the needle is combined with a device capable of determining the exact position of the geographic meridian.
The need for an instrument such as the declinometer became evident when it became clear that the geographic North Pole did not coincide with the magnetic North Pole, identified by the point towards which a magnetic needle, free to rotate in a horizontal plane, was directed.
The first indications of the knowledge of declination in Europe appear with

the portable sundials built around the XV century in Nuremberg: a small needle is placed on a line at noon and the magnetic declination is the angle between the geographic meridian and the direction indicated by the north of the needle. Knowledge of magnetic declination and spatial variation is due to Cristoforo Colombo's explorations.

In 1622 Henry Gellibrand $(1597 - 1636)$ discovered that the declination is subjected to a secular variation, while a century later George Graham $(1673 - 1751)$ found that the declension has a diurnal variation.

In the XVIII century, the construction of declinometers to measure the equilibrium position of the needle spread, while until that moment the needle was mainly used as a reference line, like in compasses. In Europe, where the magnetic declination does not exceed $20°$ on each side of the meridian, it was possible to mount the needle in a box placed in the direction of the geographic meridian.

Henry Cavendish $(1731 - 1810)$ described an advanced declinometer model in "Philosophical Transactions" of the Royal Society (1776). The greatest problems were due to the friction between the needle and its support pin, which caused the measurements to be inaccurate. This problem was overcome thanks to Coulomb and the introduction of the wire suspension which we have already mentioned which promised to achieve a high versatility of the instruments. The needle is subject only to the horizontal component of the Earth's magnetic field. The base of the instrument can be aligned in the magnetic meridian during the measurement.

Fundamental part in a declinometer is the *alidada* a goniometer used for identifying the direction of the view. Generally, it consists of a rod equipped with finishing line combined with a rotating graduated circular arc, capable of rotating on a plane parallel to the plane of the arc. Also fundamental for observational purposes are the telescopes and verniers through which the readings on the graduated circle are allowed.

In this case, the alidada is attached to the suspension apparatus, while below, on the base, we find the graduated scale. The magnetic needle, asymmetrical, measures $83.5cm$ and an index finger is screwed onto the tip with a reference line that facilitates the reading process. The needle is counterbalanced by a copper weight on the opposite end. A glass tube insulates the suspension wire. The alidada consisting of a marble bar hinged close to the suspension tube and carrying on the other end a microscope which allows the reading of the vernier and the arc of the stair placed on the bottom of the cassette.

This scale is 0 centered $4° - 0° - 4°$ and is marked each degree and divided into $10'$.
The vernier (an accessory for reading graduated scales) is divided into $0' - 5' - 10'$. Once the needle is placed in an equilibrium position in the magnetic meridian, it is possible to rotate the alidada which contains the microscope until it is placed in the same position as the needle. By making the 0 of the vernier coincide with this position, it is therefore possible to read the value sought in the measurement on the scale. French engineer Riche Prony de Gaspard $(1755 - 1839)$ designed the *magnetic telescope* (Figure 2.1), consisting of a needle and a telescope suspended by a thread, free to rotate around a vertical axis in a horizontal plane. In the wooden box which holds the needle, we can observe a top hole to house the missing torque tube. The lateral surfaces, which carry a meridian line engraved, they are made up of glass plates while two doors slide above. Inside we find three magnetic needles of different lengths suspended so that the face with the largest area is vertical. The needle placed in the middle is suspended by a hook. The three needles are $16.4cm$, $14cm$ and $11.5cm$ long, $0.8cm$ wide and $0.5cm$ thick, respectively. When the telescope is oriented along the direction of the magnetic meridian of the place of observation, the moment due to the Earth's magnetic field and that due to the twisting of the wire, are balanced. The telescope can be inverted by $180°$ with respect to a longitudinal axis, so that it is possible to correct the error caused by the mismatch between the magnetic axis and the geometric axis.
The scale is placed at a certain distance on a wall and it is possible to read the position of the needle by looking through the telescope from which it is suspended. This instrument would prove useful until the time when Christopher Hansteen $(1784 - 1873)$ designed the first magnetometer in 1819 - later made and perfected by Gauss in 1832. From then on, as magnetometers proved capable of providing both declination and value of the field component, the "pure" declinometers were set aside.
The Italian astronomer Giovanni Lodovico Quadri $(1700 - 1748)$ designed another instrument, shown in Figure 2.2. On 4 May 1743 at $08 : 00$ in Bologna a declination of $14°1'$ West was obtained. By measuring the height of the sun at a given time using a dial as a clock, it was possible to obtain the position of the geographic meridian. Finally, we cite here the Gambey's instruments 2.3 On a marble table there are two brass columns $26cm$ high and the box which houses the needle. Above the two columns is a winch which adjusts

Figure 2.1: Prony's declinometer (1783 – 1820). Image courtesy: "Museum "Galileo", ex Institute and Museum of History of Science". (Florence, Italy)

the length of the suspension wires with a twist circle. Above the ends of the needle there are two microscopes free to slide on two scales equipped with vernier. The parallelepiped needle, $51cm$ long, $1.5cm$ wide and $0.4cm$ thick, has a rider to balance the effect due to the magnetic inclination. At the end of the lake ivory blades are mounted on brass brackets divided into 17 divisions with central symmetry. The silver scale on which the microscopes slide is marked $20° - 10° - 0° - 10° - 20°$.

The nonio, subdivided $25 - 0 - 25$, allows to measure up to the hundredth of a millimeter giving the seconds. The needle is closed by two movable wooden lids with a glass window. By the alignment of the instrument is aligned with the magnetic meridian, it is possible to observe the equilibrium positions which the suspended needle assumes gradually.

Once the microscope reticle has been made to coincide with the zero point of the needle, the displacement of the needle with respect to this position can be observed by counting the number of divisions passing under the crucifix of the two microscopes. If, on the other hand, the elongations are greater, the motion is followed by means of the screw which moves the microscope.

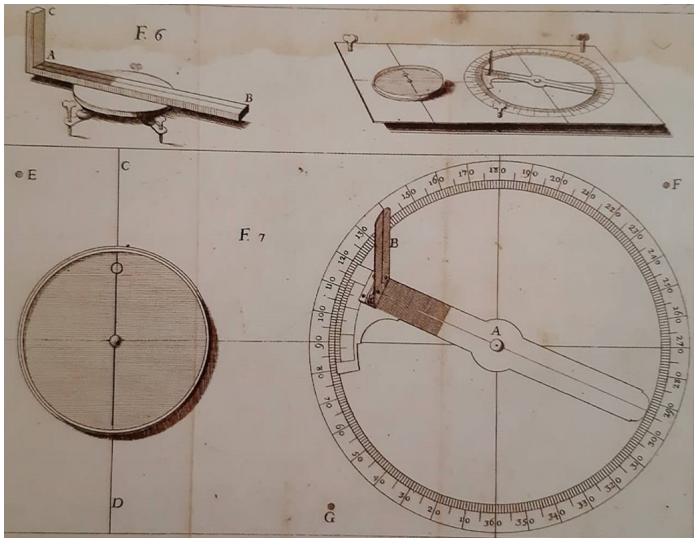

Figure 2.2: The Quadri's declinometer (1733 – 1743). Image coyrtesy: Physics and Astronomy Department of University of Bologna. (Italy)

When the angular value of a scale subdivision is known, the variation of the declination can be measured directly. .

2.2 Inclinometers

The *inclinometers* are useful tools for measuring the angle which the direction identified by the North Pole of a magnetic needle free to move around a horizontal axis in the plane of the magnetic meridian forms with the horizontal plane. Only at the Equator does the needle appear in a perfectly horizontal position while in every other point of the Earth it assumes a position inclined downwards (northern hemisphere) or upwards (southern hemisphere) with an angle value which increases with latitude by becoming vertical at magnetic poles.
The simplest possible instrument of this kind is illustrated in Figure 2.5. It was built in 1847 in the Jest workshop - which used to work for the University of Turin. Due to the poor accuracy, this instrument was usually used for teaching purposes. The needle - 23cm long - is fixed on a circular metal base, which is asymmetrical and can rotate around the horizontal axis thanks to two pins resting on the upper fork. The north tip of the needle constitutes the reading index. The circle is graduated $0° - 90°$, marked every $10°$, divided into degrees with the 0 facing up. It is possible to measure the magnetic

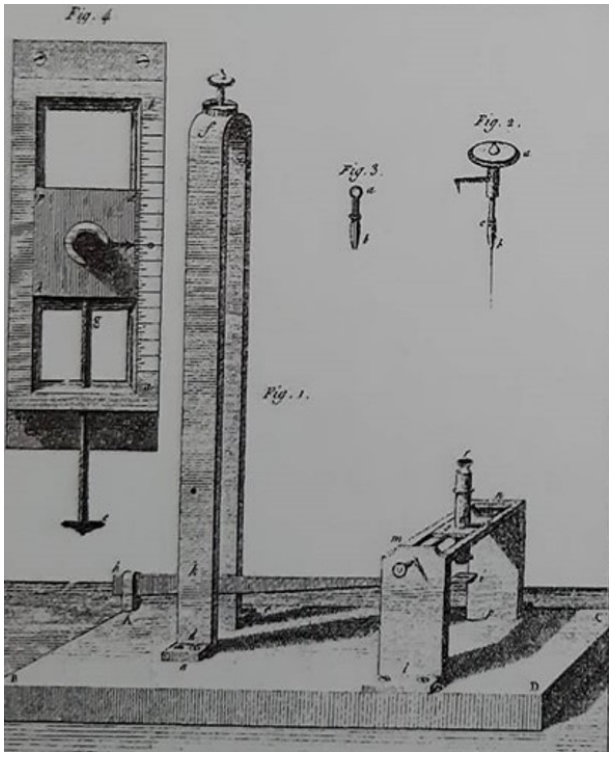

Figure 2.3: Coulomb-Gambey's declinometer (1845) - Image courtesy: Physics Department, University of Genoa. (Italy)

inclination after positioning the needle on the magnetic meridian with the aid of a compass. The basic model of each inclinometer consists of a pointed needle placed within a vertical circle rotates on planes or on agate cups.
In general, an inclinometer provides the inclination directly only when the needle oscillates in a vertical plane coinciding with that of the magnetic meridian by virtue of the sensitivity to the vector magnetic intensity. In any other plane - to measure the inclination - it is necessary to perform two observations: either on two vertical planes placed perpendicularly in two azimuths or in two planes of which the first vertical is perpendicular to the magnetic meridian and the other in the horizontal plane.
The discovery of the magnetic declination is due to the priest Georg Hartmann $(1489 - 1546)$ who was the first, during a trip to Rome in 1510, to measure the declination angle which turned out to be $6°$ towards the East $(6°E)$.
The British sailor Robert Norman $(1560 - 1584)$ in 1576 built the first instrument for measuring the inclination. To avoid errors, conjugate measurements were made and the average value was taken.

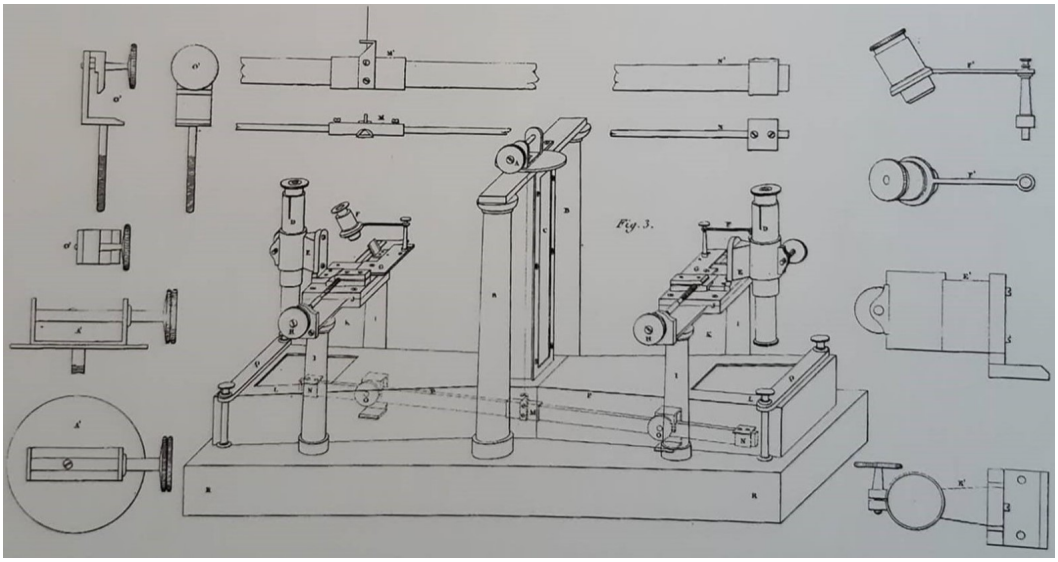

Figure 2.4: Gambey's magnetometer

The main errors were:
1 - The eccentricity of the geometric axis of the needle due to the lack of coincidence between its center and that of the vertical graduated circle;
2 - The non-alignment between the geometric axis and the magnetic axis;
3 - The non-coincidence between the axis of rotation and the center of gravity.
In fact, measurements were made on a plane perpendicular to the magnetic meridian and the ends of the needle were balanced with special weights. The inclination was therefore obtained indirectly, reversing the sense of magnetization and calculating it as the average of the values obtained. However, this procedure was valid only if the magnetic moments of the needle were equal while in reality it is the tangent of the inclination which is the average of the tangents of the values obtained.
To re-magnetize the needle, the method of *separate contact* was used, which was carried out by means of two magnets with which the needle was rubbed from the center to the ends. After the operation was repeated, the magnetic poles aligned in one direction.
In 1743 the French Academy announced a prize aimed precisely at improving inclinometers. In winner, from Daniel Bernoulli $(1700 - 1782)$, proposed an instrument in which a needle had fixed a small graduated center and an index. Before magnetization it was necessary to balance the needle. Subsequently, the magnetic inclination between needle and index finger was determined in different positions.

Figure 2.5: Simple inclinometer (1847). Image courtesy: Real Collegio "Carlo Alberto", Moncalieri (Turin). Italy

Around the 50*s* of the XVIII century, the first measurements of relative intensity were also performed to obtain which it was necessary to swing the needle and measure the period. This type of operation was possible due to the fact that Euler had shown that the square of the period of oscillation of a magnetic needle is inversely proportional to the intensity of the Earth's magnetic field.

In 1778 Jean Charles Borda (1733 – 1799) introduced a method of comparison for measuring the strength of the magnetic field in different locations around the globe. Due to the dependence on the magnetic moment of the needle and the strength of the Earth's field, multiple needles were swung in the same place in order to obtain comparison standards while the same needle was used in multiple locations (Paris, London and Oslo).

Between the end of the XVIII century and the beginning of the XIV century, Alexander Von Humboldt (1769 – 1859) - with a trip to South America and the use of a Jean-Joseph-Étienne Lenoir's (1822 – 1900) inclinometer - was able to demonstrate that the strength of the Earth's magnetic field varied as it moved from the equator, where it was lowest, towards the Poles, where it was highest. Among the most used instruments in this era we find one built by Henry Prudence Gambey (1787 – 1847) for the Astronomical Observatory in Paris which was used for the circumnavigation of the globe by Louise-Isidore Duperrey (1786 – 1865).

In 1834 Robert Ware Fox ($1798 - 1877$) designed an inclinometer capable of measuring total relative intensity and inclination at sea. Later models were built by Henry Barrow ($1790 - 1870$), John Dover ($1824 - 1881$) and Alfred Walter Dover ($1857 - 1920$).
In these models, the graduated circle and the entire measuring apparatus were separated from the magnetic needle and made it possible to perform absolute measurements of the total intensity of the field by applying the Humphrey Lloyd's ($1800 - 1881$) method which, despite deriving from the Gauss method, was less accurate. It was in fact necessary to calibrate the instrument in the observatory due to mechanical friction problems.
In a typical Barrow's magnetometer (as shown in Figure 2.6), the magnetic needle rotates freely around a horizontal axis in a vertical plane. The method of measurement is separated into two operations: the first shows the equilibrium position of the needle in the magnetic meridian under the action of the Earth's magnetic field and the field created by a deflecting needle which is placed frontally in a plane vertical and $90°$ from the first. The center of rotation of the two needles are placed horizontally on the same axis. In this way, the quotient between the magnetic moment of the deflecting needle and the total intensity F of the field can be calculated. As for the second operation, the position of equilibrium of the deviator needle is observed under the action of the Earth's magnetic field and a small weight that serves to balance it. The second operation, on the other hand, provides the product between the magnetic moment and the intensity F. By combining the two equations obtained, the absolute measure of the total intensity can be found.
In 2.6 the model of Barrow's inclinometer conserved in the Collegio Alberoni is shown. This specific instrument contains needles of parallelepiped shape, with size $9cm$ in length, $0.7cm$ wide and $0.1cm$ of thickness. The vertical circle with a diameter of $14cm$, divided into half degrees, is fixed on the same plate of the box. The graduated vertical circle $0° - 90° - 0° - 90°$ and in front of it rotates the so called alidade, i.e. the part dedicated to the angle measurements, supported by a brass pin fixed to the rim itself. This alidade is composed of two perpendicular arms, on the first of which is the reading apparatus. At the ends there is a vernier divided into minutes, marked $0° - 10° - 20° - 30°$ top and bottom $30' - 20'$ and $10' - 0'$. Under each vernier, a microscope adjustable by means of a pressure screw, allows the observation of the position of one of the two points of the needle. On the second arm of the alidade, the deviator needle allows to determine the mag-

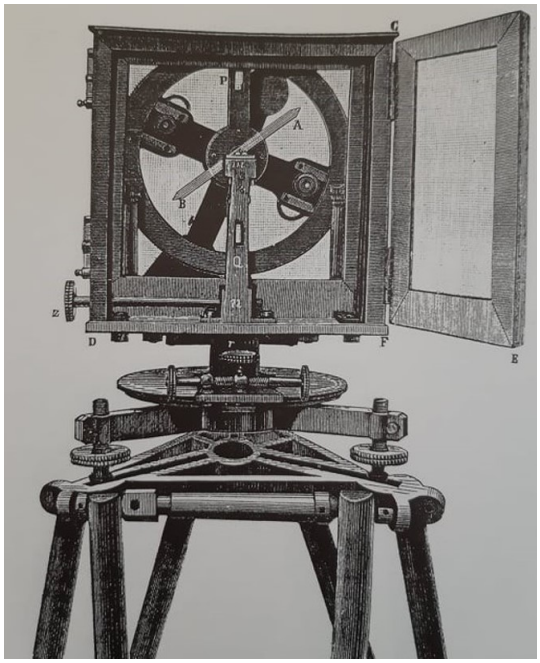

Figure 2.6: The Barrow's inclinometer (1888-1890). Image courtesy: "Collegio Alberoni" (Piacenza). Italy

netic intensity with the Lloyd's method. The wooden tripod has a base on rails which allow an arrangement of Kew's inclinometer and magnetometer. Inside the wooden case, beyond the inclinometer, there is a box in which the needles are arranged during re-magnetization, a metal box which houses a pair of magnets useful for reversing the polarization of the needle, two bone tweezers to lift the needles, some probes and brushes.

Subsequently, particular instruments are the induction inclinometers, which provide a good measurement of the magnetic inclination through the properties of a coil free to rotate in the Earth's magnetic field. The coil can rotate around a diametrical axis in all possible orientations. The measurement consists in finding the orientation of the rotation axis of the coil for which the electromotive force induced in the coil is zero. This condition is reached only when the axis of rotation is parallel to the Earth's magnetic field. The angle that this axis makes with the horizontal plane is the magnetic inclination.

The idea of measuring the field based on the induced currents resulting from the rotation of a coil dates back to Weber but only in the decade $1880-1890$, with the introduction of the null method by Heinrich Wild $(1833-1902)$ and Eléuthère Elie Mascart $(1837-908)$, its application spread.

2.3 Magnetometers

During the XIX century, magnetometers were instruments capable of measuring the intensity of the total Earth magnetic field F or its horizontal H or vertical Z component.
Until 1832, the year in which Gauss designed and built his magnetometer, declinometers and inclinometers were also used to measure the intensity by exploiting the principle according to which the square of the number of oscillations in the unit of time of the magnetic needle of a declinometer or an inclinometer placed perpendicular to the plane of the magnetic meridian is directly proportional respectively to the horizontal component H or to the vertical component Z of the Earth's magnetic field.
In addition to the oscillation method, at the end of the XVII century, another one was introduced, valid for magnetometers that measured the Z component. This mode consisted in balancing the torque due to terrestrial magnetism with a torque due to a weight placed eccentrically on the magnetic needle.
Until the '30 years of the XIX century, the intensity measurements were relative, in fact, the torque acting on a magnetic needle depends on the magnetic moment M of the needle as well as on the Earth magnetic field.
In explorations between 1799 and 1804, Humboldt fixed the F unit intensity of the field by means of an inclinometer whose needle on the Equator swung 211 times in ten minutes while in Paris it swung 245 times.
The first magnetometer specifically designed for indirect and relative intensity measurements is due to Hansteen and was based on the oscillation method, but only with Gauss the procedure which guaranteed the absolute measurement of the Earth magnetic field was developed.
The determination of the Gauss method of the intensity of the Earth's magnetic field implies the simultaneous realization of an oscillation experiment and a deflection experiment using two permanent magnets.
In the first experiment a magnetic needle is made to oscillate: the square of the period of oscillation is inversely proportional to the product MH where M indicates the magnetic moment of the needle and H the horizontal component of the Earth's magnetic field.
In the second experiment, instead, the magnet which previously oscillated is replaced with another magnet whose deviation is measured under the action of the deflecting magnet of the Earth's magnetic field. Gauss succeeded in

demonstrating that this action proportional to the M/H ratio depends on the distance between two magnets. This method is known as the *tangent method* [73].

In addition, Gauss fine-tuned the measurement procedure to minimize possible sources of error such as the moment of inertia of the needle, the non-zero twisting of the suspension wire, the variation in temperature during the measurement and the influence of the observer on the instrument. The shortcomings of this method were due to the fact that it did not take into account the Earth's magnetic induction on the needles and also the time required to perform the measurement, which was about 45 minutes: the result does not take into account the time variation of the field.

The fundamental modification to these methods was introduced by Johann von Lamont, (1805−1879) who, in his procedure, required the deflecting magnet to be held perpendicular to the deflecting magnet. With this method, known as *Gauss-Lamont's method* or *Sine Method*, used for example in the Kew's magnetometer, it is not necessary to take into account the twist of the wire.

Another method developed in the XIX century for the absolute measurement of the Earth's magnetic field involved the use of soft iron bars magnetized by the Earth's field which caused the deviation of a magnetic needle. By measuring the deviation it was possible to trace the value of the field that had determined it. The methods based on the use of electric current did not find many applications due to the difficulties of current measurement, in fact, the *Compass of Sinus* or *Tangent Compasses*, typical of the XIV century are instruments which measure the current once known the Earth's magnetic field. See Appendix 3 for other details.

It was necessary to wait for the technological improvements of the XX century to overcome all these difficulties.

A particular type of magnetometers, of which we report the images below, are the variometers, instruments capable of providing the temporal or spatial variations of the components of the Earth's magnetic field with respect to a reference value.

Readiness is the key feature of the variometers whose first example was the two-wire variometer built in 1837 by Gauss. The equilibrium condition of the needle is obtained when the moment of the horizontal component of the Earth's magnetic field is equal to the torque which, once known, allows to obtain the intensity value. The spinning lake is suspended by two symmetri-

cal vertical threads with respect to the center of gravity. The greater is the distance between the two wires and the center of gravity, the greater is the torque.
In the original apparatus, Gauss used a magnet $11kg$ heavy, $1m$ long and suspended from two steel cables $5m$ long each. The main problems were due to the temperature and although conceptually the bifilar was able to provide the absolute declination of the horizontal intensity of the respective variations, it was used only for the latter purpose.
In 1842 Humphrey Lloyd designed his balance in which a magnetic needle is free to move in a vertical plane around a horizontal pivot passing through the center of gravity. This is a very delicate instrument because the suspension rests on hard stone plates, therefore sensitive to temperature variations. The introduction of photographic recording constitutes the beginning of a new phase for the study of the variation of the field.
Starting from magnetometers for the temporal variation, spatial variometers have been developed, providing the ratio of the same component of the Earth's magnetic field in two different places. These devices are mainly used for geophysical prospecting.
In 1915 Adolph Smith $(1860 - 1944)$ designed his balance and also used primarily for geophysical prospecting. In this case the magnetic bar was easily transportable and the addition of a photoelectric cell to the scale-which took place after World War II-also made photographic recording possible.
Also worth mentioning is the La Cour's BMZ (Balance Magnetometer Zero) [64] in which the needle is brought into a horizontal position by the magnetic force exerted by compensating magnets and not by a weight force. Such an instrument can be used in any azimuth, but it basically depends on the characteristics of the compensating magnets. A further technical achievement was the realization of suspension wires with a high torsion coefficient which made it possible to do without the two-wire suspension.
The QHM La Cour, [64] designed in 1936, is a single-line variometer useful for measuring the variation of the horizontal component of the Earth's magnetic field. The torque balanced by the moment of the horizontal component of the Earth's magnetic field can provide comparison measures of the horizontal component.
Using a single quartz wire Hans Dietrich Haalck $(1894 - 1969)$ designed the GFZ, a highly portable instrument in which the variation of the vertical component of the Earth's magnetic field causes the magnet to deviate from its

horizontal equilibrium position. To bring it back to that position, it is necessary to twist the suspension wires. Once the instrument has been calibrated, by reading the angular variation, the measurement of the vertical component can be obtained.

From the Chasselon industries (Paris), one of the most specialized technology companies in the construction of devices related to the measurement of magnetism, comes the magnetometer shown in Figure 2.7. This instrument is currently kept at the Military Geographical Institute-Museum of Ancient Instruments in Florence. Many parts of the original structure have been lost or are worn. Its peculiarity is the U-shaped alidade which carries on one arm a maneuverable cage with a counterweight and on the other arm a Zenith circle equipped with two microscopes for reading, a level and a telescope under the microscope.

The cage is closed at the two bases by mica screens, at the center of which is fixed a tube which allows reading under the microscope. Inside the cage, in the upper central part, a small tube houses the silk twisting thread. There is also an oscillation damper in bone. A needle holder is attached to one end of the silk thread. There is a small tube in which a thermometer to the tenth of a degree is introduced. The azimuth and zenithal circles have a diameter of $15.0cm$ and $11.0cm$, respectively. In determining the magnetic declination, the geographic meridian was identified by observing the position of the sun in the first vertical. Measurements were always performed with two needles and using the Lamont method. The measure took about 45 minutes. The instrument shown in Figure 2.8 was designed by Hansteen in 1819 and is simply a variation of the Coulomb torsion balance adapted to measure the declination and horizontal component of the Earth's magnetic field. On a triangular wooden base there is a wooden cylinder with four holes, two of which are diametrical while the others are symmetrical with respect to a small telescope. The cylinder can be rotated through an adjustment screw which allows you to follow the movement of the needle with the telescope. Inside the cylinder we find a metal tube containing the silk thread which holds the needle suspended. At the top of the suspension tube, a winch allows to raise and lower the wire.

After using a magnetic bar with the same thick weight as the needle in the initial phase to eliminate the torsion, the needle is diverted from the equilibrium position and the oscillations are counted. The square of the number of oscillations will be directly proportional to both the component of the

Figure 2.7: Magnetometer built at Chasselon (1932). Image courtesy: Military geographical institute of Ancient Instruments (Florence). Italy

Earth's magnetic field and the magnetic moment of the needle. After assuming that the magnetic moment is constant, it is sufficient to calculate the ratio between the squares of the number of oscillations to obtain the relative measurement of the component of the Earth's magnetic field. A Lloyd's balance (Figure 2.9 can provide a measurement of the variation in the vertical component of the Earth's magnetic field. This instrument consists of a magnetic needle free to rotate in a vertical plane around a horizontally fixed pin passing through its center of gravity. The needle is placed in a horizontal position and is held by weights. If it is placed on a vertical plane perpendicular to the magnetic meridian, the opposing action between the weight force of the weights and that of the vertical component of the Earth's magnetic field alone keep it in balance. The horizontal component of the Earth's magnetic field is in fact balanced by the constraint constituted by the horizontal pivot suspension.

Any displacement with respect to the equilibrium position is proportional to the sole variation of the vertical component. Assuming to place the bar in the magnetic meridian, the equilibrium position will also depend on the horizontal component. In this particular situation the variation of the angular position will depend on the vertical component of the average magnetic inclination of the Earth's field. In Figure 2.10, a picture of the Weber's magnetometer is reported. This instrument can work in two different ways. The

Figure 2.8: Hansteen's magnetometer (1819-1838). Image courtesy: Museum "Galileo", ex Institute and Museum of History of Science. (Florence). Italy

Figure 2.9: Lloyd's balance (1859). Image courtesy: Astronomical Observatory, Monte Porzio Catone (Rome). Italy

first is the Gauss' method, through which the period of oscillation of a needle suspended from the thread can be measured and then the deviations which this in turn induces on a second needle suspended in its place are measured. For this second operation it is necessary to associate the Weber's compass to the magnetometer.
The second operating principle is instead obtained by passing an unknown electric current in the coil, so that the needle is affected by the action of two magnetic fields. Through the deviation that the needle undergoes with respect to the initial position, it is possible to trace the value of the current. This instrument (Figure 2.11) designed by Ciro Chistoni (1852 – 1927) [34]

Figure 2.10: Weber's magnetometer (1832). Image courtesy: National Museum of Science and Technology "Leonardo Da Vinci" (Milan). Italy

is composed of a base and various attachments, including a movable wooden box, the torsion tube, a diverter bar, a magnet holder trolley to make the relationship between the magnetic field H and M, a trolley for measuring the induction coefficient and other magnets. The base consists of a graduated circle placed on a tripod with leveling screws. This circle is graduated from 0° to 360°. Internally the alidada can be blocked by means of a screw. The verniers are read with a microscope: they are divided into 20″ and are marked $0' - 5' - 10'$. On the base there are two levels and two diametrically opposite stops used to block the metric bar. Two outgoing brackets are placed perpendicular to the bar, on one of which the telescope is placed while the mirror used to send light into the box is housed on the other. With this

instrument, the magnetic declination, the component of the Earth's magnetic field and various magnetic constants can be determined.
The measurement procedure is based on the calculation of the astronomical meridian through the telescope. The magnetic meridian is determined by finding the equilibrium position of the freely suspended magnet and inverting the needle by 180° to avoid errors of mismatch between the geometric axis and magnetic axis. The Adolph William Schmidt's $(1904-2000)$ instrument

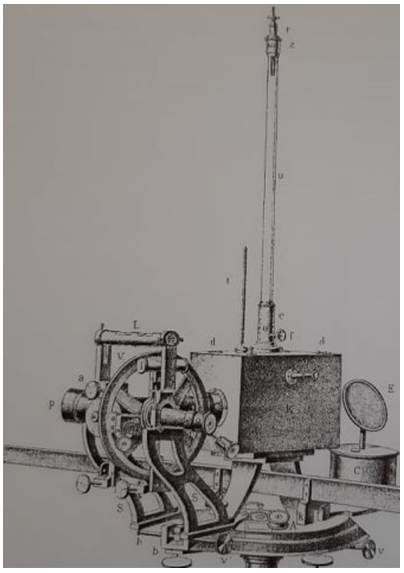

Figure 2.11: Chistoni's magnetometer (1893) National Museum of Science and Technology "Leonardo Da Vinci" (Milan). Italy

(Figure 2.12) consists of a cruciform theodolite and an oscillation box. . The theodolite is placed on a pin and also has a device capable of controlling fine adjustments. The pin is supported by a tripod with leveling screws, while the azimuth circle has a diameter of approximately $27.0cm$. The scale is marked every $1/15°$ and allows angle readings with an accuracy of $2''$. The torsion tube is equipped with a torsion head graduated every $0.5mm$. The suspension wire is controlled by a stop device mounted on its lower part. The entire torsion tube adapts to the base plane of the tripod and is equipped with a torsion circle which allows it to rotate around the axis of the instrument. This device can be used for minimal torsion measurements.
The deflection magnet housings are placed on a small graduated circle $0° - 360°$ free to rotate around a vertical axis. A comparator allows the calibration of the position of the diverter magnets. The oscillation box, made of non-metallic material, is separate and houses the magnet which rests on a

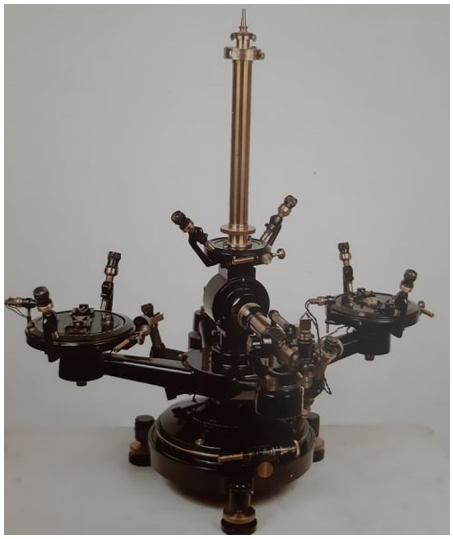

Figure 2.12: Schmidt's teodolite

bracket with double mirror. A particular device limits the magnitude of the oscillations of the magnet. The suspension wire is contained in the torsion tube, the lower part of which is equipped with a device to stop the wire itself. The torsion drum is divided into 60 divisions and leveling is conducted via repeated measurements made with a telescope. The measurements are carried out by checking the vertical position of the image of the scale placed above the telescope, which is used to read the point of passage of the magnet and the amplitude of the oscillations. The telescope is equipped with a swivel arm that can rotate 180°. Among the annexes of the theodolite we can list: a cylindrical bronze rod of 70cm and 1.6cm in diameter; a perforated magnetic cylinder 7.5cm, 1.6cm in outer diameter and 0.8cm in inner diameter; two cylindrical-shaped diverter magnets 7.5cm long, 1.6cm in outside diameter and 8.5cm in inside; a magnet with four cross-placed mirrors, 4.6cm long by 1.2cm in diameter a magnetic disc; a two-mirror non-magnetic cylinder 6.7cm long and 1.5cm in diameter; two declination magnets with two mirrors of high and low magnetic moment, respectively 7.6cm and having a diameter of 1.2cm. This theodolite is designed for research and above all for the determination of the parameters of the magnets used in the measurements itself, its particularity is that the deflecting magnets have the possibility of assuming any azimuth position with respect to the deflected magnet.
Furthermore, this instrument is equipped with a comparator to check the distance of the diverter magnets. It provides a measurement accuracy of

$0.05'$ for the declination and for the horizontal H intensity of $1/\gamma$ range. It was used for absolute measurements.

2.4 Recent instruments based on classical physics

Starting in the mid-XIX century, magnetometers became increasingly used instruments for measuring magnetic fields, for calibrating electromagnets and for determining the magnetization of materials.
Magnetometers are generally characterized by their accuracy and sensitivity, which determine the precision of the device. This characteristic can be thought as the smallest change in the field level which the sensor can discern, or as the size of the smallest field which it can detect.

2.4.1 Hall's effect magnetometers

Among the magnetometers which have the widest technological applications, there are Hall's effect probes, widely used above all for the detection of metal samples in the subsoil. They are based on the phenomenon discovered by the American physicist Edwin Herbert Hall ($1855 - 1938$) who noticed how a transverse potential difference occurred in a conductor crossed by electric current longitudinally when subjected to a perpendicular magnetic field [90].
The Hall's element is formed by a strip of material which can conduct electricity, usually a conducting metal or a semiconductor. The thickness of the strip is negligible compared to the other two dimensions. A current is made to flow by applying an electrical voltage across it.
The Lorentz's force acts on the conduction electrons, which move and are affected by the magnetic field

$$\mathbf{F} = q_e \mathbf{v} \times \mathbf{B} \tag{2.1}$$

This is orthogonal both to the direction of the magnetic field and to the direction of motion of the charge carriers.
By imposing the equilibrium conditions, in which the Lorentz's force is compensated by the force that originates from the transverse electric field, it is possible to obtain the formula for calculating the voltage

$$V_H = \frac{I_z B_z}{n t q_e} \tag{2.2}$$

where I is the current, n is the density of the carriers, t the width of the material.
The Hall's voltage is proportional to the current and to the intensity of the magnetic field, but inversely proportional to the density of the carriers and to the width of the material, consequently, to obtain measurable values it is necessary to use thin metal samples. The dependence on the number of carriers causes a very small effect in conductive materials and a more pronounced effect in semiconductor materials, which have fewer charge carriers. This effect is used for the construction of sensors for measuring the magnetic field.
Hall's sensors, compact, robust and inexpensive, generally have measurement ranges from a few mT up to over $1T$; they are usually provided with an analogue output whose value is proportional to the magnetic field on the basis of a proportionality constant which determines its sensitivity.

2.4.2 Fluxgate magnetometers

Fluxgate magnetometers have been widely used since the $1930s$ in various fields of applications, and are the best choice for low intensity magnetic field measurements, usually in the pico-Tesla range. These dispositives measure the intensity and orientation of magnetic flux lines and are vector devices, i.e. sensitive to the direction of the field.
They prove particularly efficient in geological prospecting, in aerospace, land and underwater navigation, as well as in localization methods such as the Global Positioning System (GPS).
The basis structure has a circuit, usually consisting of a ring of material with high magnetic permeability, to which two coils of conducting wire are wound. A periodic current of very high intensity is injected into the wire. The current brings the core close to saturation, from where it begins to show its non-linear behavior.
The basic idea is that, if with the current injected in one direction the non-linearities appear earlier than in the opposite direction, it means that an external magnetic field is superimposed. In practice, another coil is wound around the magnetic core, so that the current induced in it is zero in the absence of external fields, as the coil does not intercept the magnetic circuit, but becomes appreciable in the presence of an external field, which reinforces the magnetic field in one direction and therefore the non-linearities.

It will therefore be seen, in the circuit, an induced current having the same period as the injected one, with superimposed higher order harmonics, the more intense the closer the core is to saturation. Since the proximity to saturation is induced by the external field, a measurement of this is obtained by canceling the main frequency of the induced signal and measuring how much remains, to have a measurement of the external magnetic field.
In the realization of this type of magnetometers, it is necessary to pay close attention to the materials used in the assembly of the components.
The resolution of $100pT$ [93] and the absolute precision of $10nT$ are standard in commercial devices, but can achieve a resolution of $10pT$ and $1nT$ long-term stability. In general, when a resolution in the nanotesla range is required, Fluxgates are the best choice [121]; they are robust, low power, affordable, and available as integrated circuit.

2.4.3 Inductive coils

Inductive pick-up coils operate by Faraday's law of induction [142]. Pick-up coils are simple, robust and cheap, finding numerous high-frequency applications, such as the modern Magnetic Resonance Induction method. Just to compare this simple instrument with the ultimate technological findings, their fundamental sensitivity limit is 10^7 times worse than an Atomic Magnetometer of the same volume [132].

2.5 Recent developments in Magnetometry

Hans Georg Dehmelt ($1922-2017$) [50] originally proposed the observation of precessing alkali spins in order to determine the strength of a field, Robert Edward Bell ($1918-1992$) and Arnold Lapin Bloom (1923) in 1957 provided the first experimental demonstration [15]. Nowadays the use of neutral atoms as very precise and absolute "meters" of the physical constants is diffused in every research centre and physics laboratories. The property of any atomic system of undergoing internal structure modification when immersed into an external Magnetic Field, makes it possible to transfer the high precision, typical of atomic frequency measurements, into the field of Magnetometry. Sensitive magnetometers, therefore, traditionally have used large vapor cells and operated at low density, typically at or near room temperature. The difficulty in developing high-sensitivity magnetometers is to construct the oven

out of completely nonmagnetic materials, so as not to introduce additional magnetic noise into the measurement.
In the last years, also thanks to the development of diode lasers technology and the improvements in the realization of atomic media with very long atomic spin-orientation relaxation-times ([4], [30], [31]) many research groups have addressed their interests to the field of magneto-optical effects in atoms. A new generation of optical magnetometers was born and excellent results in terms of sensitivity, temporal and spatial resolution, robustness and compactness were achieved. A very detailed description of the possible applications of optical magnetometers is given in many review articles [15], [50], [32], [29], [133]. For example, G. Bison, R. Wynands and A. Weis obtained the first mapping of the cardiomagnetic field with a Rubidium double-resonance magnetometer and demonstrated good agreement with the magnetocardiogram obtained by a SQUID magnetocardiograph [20]. In addition, the optical Magnetometry can detect such weak magnetic fields (few hundreds fT) as those produced by the human brain activity [151].

2.5.1 Atomic magnetometers

Atomic magnetometers (AMs) allow a quantum approach to the ultra-sensitive detection of static and oscillating magnetic fields, [26], [15]. In recent technological developments these surpass super conducting quantum interference devices (SQUIDs) as the most sensitive magnetic field sensors available.
Different designs often operate in measurement regimes and each of these has intrinsic advantages and drawbacks. A brief roundup is here presented.
The spin-exchange relaxation-free magnetometer (SERF), operating in high-density, low magnetic field regime, is capable to eliminate the loss of coherence due to spin exchange collisions. These devices are immune to decoherence caused by spin exchange in measuring of the average atomic spin. They are only applicable to low-frequency measurements, for instance, zero-field nuclear magnetic resonance (ZFNMR).
Radio-frequency atomic magnetometers (RF-AMs) detect oscillating magnetic fields by bringing them into resonance with Zeeman transitions in the ground state and by the control of the bias field. Inversely, a DC field can be measured by detecting the resonant frequency. Importantly, RF-AMs can maintain high-sensitivities without such shielding [35]. The operating frequency can be tuned over a wide range, from near DC to the MHz band

[46].
Alternative schemes have demonstrated operation in the GHz band [82]. Non-linear magneto-optical rotation (NMOR) [89], employs a parallel pump and probe beam arrangement to determine the magnetic field along the propagation direction; these devices do not require magnetic field excitation. NMOR based magnetometers have demonstrated sub-picotesla levels of sensitivity to both DC and oscillating magnetic fields [123], [98].
Coherent Population Trapping (CPT) effect plays a central role in Magnetometry. In fact, a class of magnetometers is based on this quantum interference effect [3], [100]. The push-pull magnetometers are based on the push-pull optical pumping technique.

2.5.2 Applications of AMs

There are numerous applications for AMs in a wide range of fields. For example, medical applications include magnetoencephalography [24], [151], magnetocardiography and foetal-magnetocardiography, [150], [86], the detection the magnetic fields produced by nerve pulses [84], and magnetic resonance imaging (MRI) [130].
AMs have been used in detection of low-field NMR signals [131], [132], [17], [18], Nuclear Quantum Resonance NQR signals and magnetic nano-particles suspended in fluids [25]. Another application includes aiding archaeological excavations [110] and the mapping of geophysical anomalies [39]. In addition, AMs can be used in tests of fundamental physics and exploring physics of Standard Model [122]. Important progress has been made in portability and power consumption and portable devices are now commercially available [14], [122], [65].

2.5.3 MIT and EMI

Magnetic Induction Tomography (MIT) is a technique for probing electromagnetic properties of samples [94], [99], [68], [71]. It can provide direct non-contact, non-invasive maps of all three passive electromagnetic properties, the conductivity σ, the relative permittivity ϵ_r and the relative permeability μ_r.
In MIT an oscillating magnetic field referred to as the primary field is applied from an excitation coil to induce eddy currents in a sample. These eddy

currents generate an additional magnetic field component in which details of the sample's electromagnetic properties are imprinted into the properties of this field. The detection and imaging of changes in the dielectric properties finds applications in a wide range of fields. Potential examples include the detection and diagnosis of cardiac arrhythmias [109], [43], related to the abnormal generation and conduction of heart pulses [109].
Further examples of conditions which Electromagnetic Induction i.e. EMI could be applicable to include: the detection of cerebral diseases [151], [86], [154] and the detection of cancerous tissues [71], [87], [134], [37], [63].
Aside from medical imaging, EMI has a broad range of industrial applications, including the detection and location of foreign bodies, the security scanning of cargo, batch quality control, the detection of defects in components, the investigation of the structural integrity and the detection of corrosion in pipelines, etc [46], [43], [107], [106], [108], [83].

2.5.4 An EMI system based on Atomic Magnetometers

The performance of an EMI system is ultimately determined by the choice of the magnetic field sensors. In general, the sensitivity limits the detection level, the sensing volume limits the spatial resolution and the frequency tunability determines the kind of samples and the penetration depth of images. EMI systems rely on inductive coupling with pick-up coil, or set of coils, to detect the secondary fields: this choice places severe limitations on the overall performance, particularly regarding the sensitivity and the spatial resolution. For low-conductivity MIT measurements, coil-based systems typically have sensor coils around $50mm$ in diameter.
Eddy currents must be excited in volumes exceeding $1000cm^3$ to generate a detectable signal [69], [69], [147].
There are a number of advantages in using RF-AMs as the magnetic field sensor [148] because the sensitivity of AMs across the frequency band relevant for EMI is spanning $100Hz$ to several MHz. This overcomes the limitation of classical systems, i.e. the low-frequency sensitivity of pick-up coils. The size of the laser beams controls the active sensing volume.
The limits on the spatial resolution depends on the samples geometry, on the excited coil dimension and on the sensor dimension.
Tunability across the frequency band ensures the ability to adapt to a wide

range of samples and provides control over the penetration depth.
Generally, in coil-based systems, an unwanted capacitive coupling exists between the excitation and detection coils. To ensure that only eddy current effects are recorded, this must be suppressed [71], [94],[69]. In contrast, no capacitive coupling is present in EMI-AM. An important advantage is that no physical connection is required between the sensor, the control and read out electronics or the sample.

2.5.5 Atomic magnetometers vs SQUID

A number of technologies compete with AMs in the ultra-sensitive measurements of magnetic fields.
Superconducting Quantum Interference Device (SQUID) based magnetometers are employed for high sensitive magnetometry applications [46], [19], [106].
A simple SQUID is a loop of superconducting material containing one or two Josephson junctions. The magnetic field is inferred from the voltage across the loop, which is dependent on the number of magnetic flux quanta threading the loop [60].
SQUIDs operate at cryogenic temperatures and require magnetic shielding. Detection systems tend to be unfeasible for many portable applications. The sensitivities are below $1fT \cong pHz$.

Chapter 3

Generalities on RF Magnetometry

3.1 Atomic energy levels

The use of alkali metal atoms is a practice very diffused in physical sciences. The variety of applications depends on the possibility to approximate the energy of the atom by considering only the valence electron and the nucleus and properly treating the effects of the others electrons in the inner energy shells [27]. The valence electron has spin modulus $S = 1/2$, the ground state is an s shell with orbital angular momentum $L = 0$ while the total electron angular momentum modulus is $J = L + S = L - S = 1/2$. The first excited state is a p shell with $L = 1$, splitted by the fine structure into the $^2P_{1/2}$ and $^2P_{3/2}$ levels. The superscript denotes the spin multiplicity $2S + 1$ and the subscript denotes the total angular momentum J, so, the ground state is $^2S_{1/2}$.

The quantum jump from the ground state to the level $^2P_{1/2}$ is referred to as D1 transition and the one to the level $^2P_{3/2}$ is referred to as the D2 transition. Alkali metal isotopes have non-zero nuclear spin I. The hyperfine interaction between the electron and nuclear spins splits the atomic energy levels into states with the new total atomic angular momentum $F = I + J$. By Wigner-Eckart's theorem, the electron angular momentum vector J can be expressed in terms of the total atomic angular momentum vector F.

The $^2S_{1/2}$ and $^2P_{1/2}$ states are split into levels with $F = I \pm 1/2$. These levels, separated by the hyperfine energy splitting E_{hf}, can be considered of as states with the atomic and nuclear spins lying parallel to one another and the

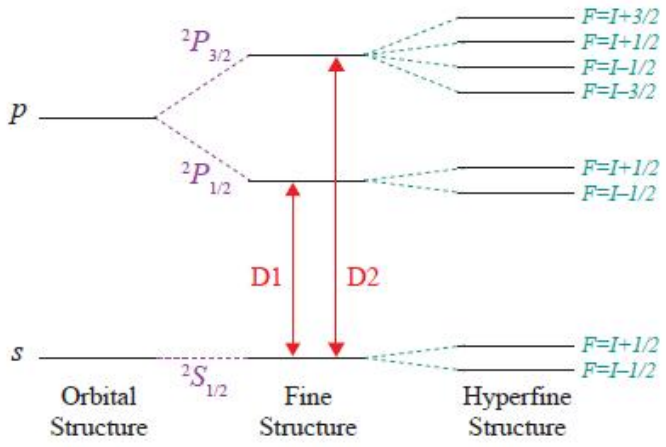

Figure 3.1: Energy level splitting of the ground state and first excited state of an alkali metal atom. The fine structure splits the first excited state into levels with $J = 1/2$ and $J = 3/2$, and the hyperfine structure further splits the energy levels due to the nonzero nuclear spin. Image courtesy: S.J. Seltzer, Princeton University. PhD Thesis (2008).

electron spin either parallel $F = I+1/2$ or anti-parallel ($F = I-1/2$) to both. The $^2P_{3/2}$ state is split into levels with $F = (I-3/2, I-1/2, I+1/2, I+3/2)$. The degeneracy between different Zeeman's sublevels with projection $m_F = (-F, -F+1, ..., F-1, F)$ of the atomic angular momentum along some quantization axis, is lifted by interaction with an eventual external magnetic field. The energy splitting ΔE_{m_F} depends on the strength of the field.
In Larmor's spin precession formula γ is the gyromagnetic ratio of the atomic spin. The valence electron couples much more strongly than the nuclear spin to an external field.
The gyromagnetic ratio is that of a bare electron, excepting for the fact that the electron spin must drag the nuclear spin along as it precesses. Then $\gamma \approx \pm 2\pi \times (2,8MHz/G)/(2I+1)$, where the sign depends on the hyperfine level $F = I \pm 1/2$.
In atomic magnetometers it is necessary to have resonant or near-resonant light to both polarize the alkali atoms and probe their spin orientation. The rate $R_{abs}(\nu)$ at which an atom absorbs photons of frequency ν is

$$R_{abs}(\nu) = \sum_{res} \sigma(\nu)\Phi(\nu) \tag{3.1}$$

where $\Phi(\nu)$ is the total flux of photons of frequency ν incident on the atom

in units of number of photons per area per time. The sum is made over all atomic resonances.

If we use lasers with line-width which is much narrower than those associated with the atomic D1 and D2 transitions, the incident light can be treated as monochromatic. To calculate the absorption cross-section $\sigma(\nu)$, it is necessary to know the atomic frequency response about the resonance frequency ν_0. This depends on the lifetime of the excited state, the pressure broadening due to collisions with other gas species and the Doppler broadening due to thermal motion of the alkali atoms. The integral of the absorption cross-section associated with a given resonance

$$\int_0^{+\infty} \sigma(\nu) d\nu = \pi r_e c f_{res} \tag{3.2}$$

where r_e =2.82×10^{-15} is the classical electron radius and c =$3\times10^8 m/s$ is the speed of light, is a constant.

The oscillator strength f_{res} is the fraction of the total classical integrated cross-section associated with the given resonance and is given by $f_{D2} \approx 2/3$ for alkali atoms. The heavier elements have values which deviate slightly, because of the spin-orbit interaction and core-valence electron correlation.

The experimental setup described in this Thesis uses - as sensor - a vapor cell containing a ^{85}Rb-^{87}Rb mixing, excited both on D1 and D2 line. The respective relative abundances are of 0.7217 and 0.2783 [139]

For optical pumping and the detection of atomic precession we use optical transitions between ground and excited hyperfine levels, in particular electric dipole transitions. These respect the selection rules $\Delta F = \pm1, \Delta m_F = 0, \pm1$ (ΔF labels changes of the F quantum number and Δm_F of the magnetic quantum number, $m_F = [-F, -(F-1), ..., +(F-1), +F]$). Zeeman's transitions drive the atomic precession.

The abundance of Rb at a given temperature follows the approximated vapor-pressure equations, respectively for solid phase, $t \ll 39.3C$ and for liquid phase, $t \gg 39.3C$

$$\log_{10}\left(\frac{P_{85,87}}{\mu_{85,87}}\right) = 2.881 + 4.857 - \frac{4215}{T} \tag{3.3}$$

$$\log_{10}\left(\frac{P_{85,87}}{\mu_{85,87}}\right) = 2.881 + 4.312 - \frac{4240}{T} \tag{3.4}$$

where $P_{85,87}$ is the pressure in $Torr$ of the given Rb isotope, $\mu_{85,87}$ is the relative abundance of that isotope, and T is the temperature in Kelvin. At

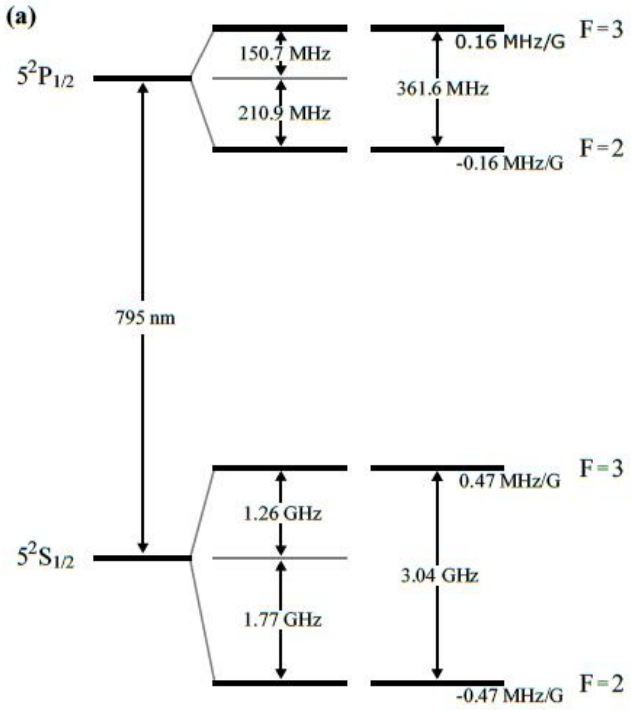

Figure 3.2: Rubidium 85 hyperfine energy level structure for the D1 transition - Image courtesy: C. Deans, Department of Physics and Astronomy, UCL - PhD Thesis (2018).

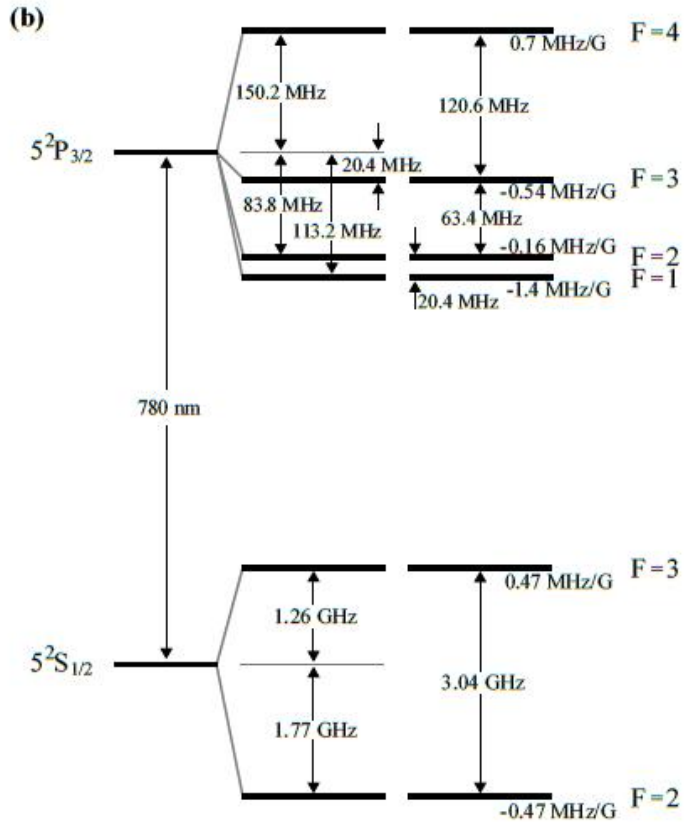

Figure 3.3: Rubidium 85 hyperfine energy level structure for the D2 transition - Image courtesy: C. Deans, Department of Physics and Astronomy, UCL - PhD Thesis (2018).

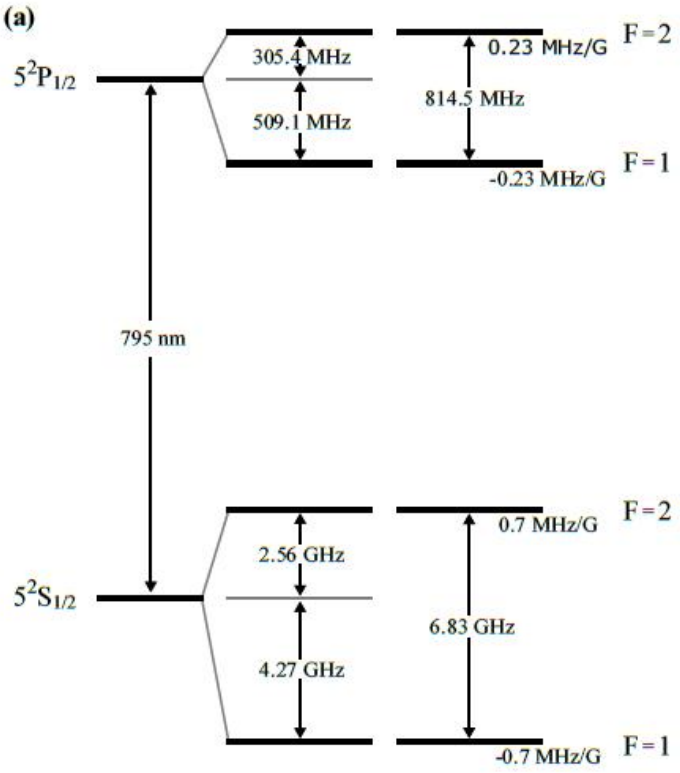

Figure 3.4: Rubidium 85 hyperfine energy level structure for the D1 transition - Image courtesy: C. Deans, Department of Physics and Astronomy, UCL - PhD Thesis (2018).

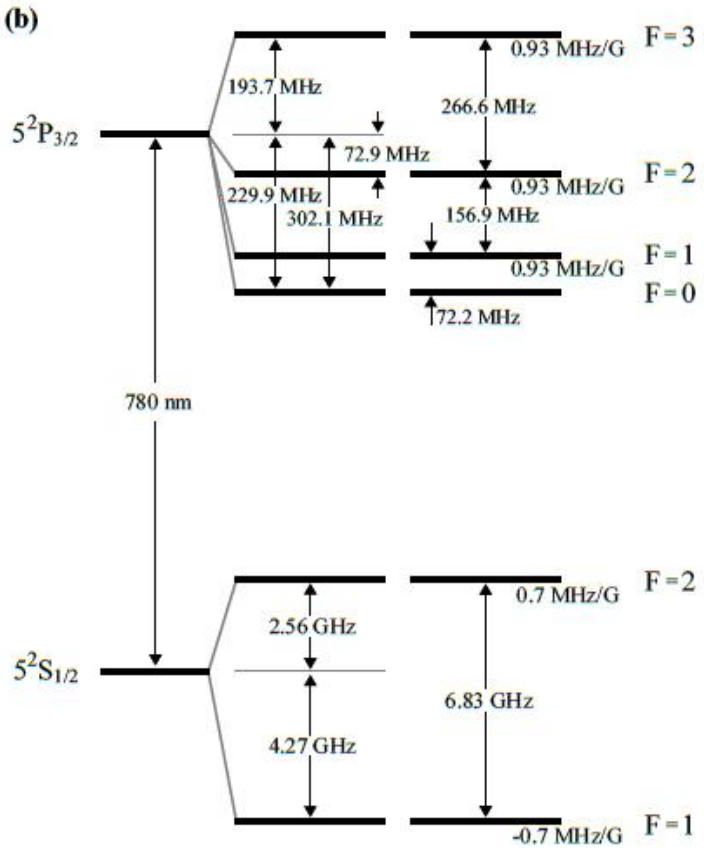

Figure 3.5: Rubidium 85 hyperfine energy level structure for the D2 transition - Image courtesy: C. Deans, Department of Physics and Astronomy, UCL - PhD Thesis (2018).

atmospheric pressure, these two equations represent the phases either side of the melting point at $39.3C$.
The vapor density from the ideal gas law

$$n_{85,87} = \mu_{85,87}\frac{133.3P_{85,87}}{k_B T} \tag{3.5}$$

k_B is the Boltzmann constant and the multiplication factor is for conversion to SI units.
In general, the sensitivity of an AM increases with an increasing number of contributing atoms. For details about Optical Absorption and Doppler Broadening, see Appendix 1.

3.2 Hyperfine splitting of the optical resonance

Consider separately the individual resonances $F \to F'$, in cases where the ground and/or excited state hyperfine splitting are comparable to or larger than the optical linewidth. Being the allowed transitions characterized by $F - F' = 0, \pm 1$ and by using Wigner-Eckart's theorem, the matrix element for the dipole transition between the ground state $|F, m_F\rangle$ and the excited state $|F', m'_F\rangle$ is written as

$$\langle F|\widehat{\epsilon}\cdot\mathbf{r}|F'\rangle^2 = \langle F\|\widehat{\epsilon}\cdot\mathbf{r}\|F'\rangle(2F+1)\begin{pmatrix} F' & 1 & F \\ m'_F & m_F - m'_F & -m_F \end{pmatrix}^2$$

where $\langle F\|\widehat{\epsilon}\cdot\mathbf{r}\|F'\rangle$ is a reduced matrix element, $\widehat{\epsilon}$ is the polarization of incident light and $q\mathbf{r}$ is the dipole moment of the atom while the parentheses denote the Wigner $3-j$ symbol.
The states are equally weighted when the vapor is unpolarized.
In case of the transition $F \to F'$ and for a given value $m_F - m'_F = \{0 \pm 1\}$, we can apply a sum rule

$$\sum_{m_F, m'_F}\begin{pmatrix} F' & 1 & F \\ m'_F & m_F - m'_F & -m_F \end{pmatrix}^2 = \frac{1}{3'} \tag{3.6}$$

Indicating with the curly brackets the Wigner $6-j$ symbol and applying for

a second time the Wigner-Eckart's theorem

$$\langle F|\widehat{\epsilon}\cdot\mathbf{r}|F'\rangle^2 = \langle J|\hat{\epsilon}\cdot\mathbf{r}|J'\rangle^2 =$$

$$= \frac{(2F+1)(2F'+1)(2J+1)}{3}\begin{pmatrix} J & J' & 1 \\ F' & F & I \end{pmatrix}^2 \tag{3.7}$$

For $J = 1/2$ and a particular value of $J' = 1/2, 3/2$, corresponding to the D1 or D2 transitions, there is the sum rule,

$$\sum_{F,F'}(2F+1)(2F'+1)\begin{pmatrix} J & J' & 1 \\ F' & F & I \end{pmatrix}^2 = 2I+1 \tag{3.8}$$

Considering only the individual hyperfine transitions $F \to F'$ within either the D1 or D2 resonances, the relative strength $A_{F,F'}$ of the transition in the normalized form

$$A_{F,F'} = \frac{(2F+1)(2F'+1)}{2I+1}\begin{pmatrix} J & J' & 1 \\ F' & F & I \end{pmatrix}^2 = 2I+1 \tag{3.9}$$

where the sum of the strengths $\sum_{F,F'} A_{F,F'} = 1$.
During collisions between atoms or molecules, energy levels vary slightly. This perturbation depends both on the electronic configuration of the particles and on the speed of the collisions. A further broadening of the spectral lines is obtained which depends on the gas temperature and pressure.

3.3 Optical pumping

In sensitive magnetometers is necessary a large atomic spin polarization. The thermal polarization of an ensemble of alkali atoms is

$$P_{ther} = \tanh\left(\frac{\frac{1}{2}g_s\mu_B B}{k_B T}\right) \tag{3.10}$$

where $g_s \approx 2$ is the electron g-factor and $\mu_B = 9.274 \times 10^{-24}$ is the Bohr's magneton. This is too small to allow for magnetometry measurements.
The optimal degree of polarization, generally on the order of unity, depends on the specific type of magnetometer.

Let us consider a pump beam resonant with the D1 transition, circularly polarized. The photons have the same spin projection along the direction of the beam propagation i.e. $\widehat{z}$ axis. For $\sigma+$ polarized light, all photons have angular momentum of $+1$ along this axis, in units of the electron spin angular momentum $\hbar$. An atom in the $m_J = -1/2$ sublevel of the ground state may absorb a photon.

The conservation of angular momentum requires it to absorb the photon angular momentum and be excited to the $m_J = +1/2$ sublevel of the $^2P_{1/2}$ state. An atom in the $m_J = +1/2$ sublevel of the ground state is forbidden from absorbing a photon. In fact there is no level in the excited state with an additional angular moment of $+1$. As we already said in a previous chapter, an inert buffer gas is usually added to the cell in order to prevent wall collisions; unfortunately, collisions with the buffer gas atoms depolarize the alkali atoms. Because of the coupling of the orbital angular moment of the p-shell electrons with the rotation of the formed molecules during the collisions, the scattering cross-section in the excited state is larger than in the ground state.

There is the very rapid collisional mixing between the Zeeman's levels of the excited state so the populations of the levels are equalized.

Atoms which spontaneously decay back to the ground state emit photon a randomly polarized and resonant that can depolarize another atom if reabsorbed.

The probability of absorption in very dense alkali vapor becomes large: this phenomenon is known as radiation trapping and can occur when reabsorption of spontaneously emitted photons limits the polarization of the alkali vapor.

In the presence of buffer gas, there is an equal probability of decaying to the two Zeeman's levels of the ground state. Atoms which decay to the $m_J = +1/2$ sublevel must remain there because they are not allowed to absorb another photon from the pump beam, while at the same time, atoms which decay to the $m_J = -1/2$ sublevel, may absorb another photon and get excited to the $^2P_{1/2}$ state again.

In the absence of relaxation mechanisms, all atoms are placed into the $m_J = +1/2$ sublevel so the alkali vapor is fully polarized with angular momentum $+1/2$ along the $\widehat{z}$ axis.

In similar way, pumping with $\sigma-$ light results in polarization with angular momentum $-1/2$ and so we can define the optical pumping rate R_{OP} as the

average rate at which an unpolarized atom absorbs a photon from the pump beam.
The rate with which an atom in the $m_J = -1/2$ sublevel of the ground state absorbs a $\sigma-$ photon is $2R_{OP}$, since atoms in the $m_J = +1/2$ are unable to absorb photons.
The amplitude A of the decay channel from the excited state $|J' = 1/2, m'_J\rangle$ to the ground state $|J = 1/2, m_J\rangle$ is given by

$$A \propto \langle J, m_J | \widehat{\epsilon} \cdot \widehat{\mathbf{r}} | J', m'_J \rangle \tag{3.11}$$

where $\widehat{\epsilon}$ is the polarization of the emitted light.
The Clebsch-Gordan's coefficients give us the branching ratios (BR) of the decay channels

$$BR = \langle J, m_J, 1, \Delta m_J | J' m_J \rangle^2 \tag{3.12}$$

All excited atoms remain in the $m_J = 1/2$ sublevel of the $^2P_{1/2}$ state and decay to the $m_J = -1/2$ and $m_J = +1/2$ sublevels of the ground state with, respectively, branching ratios of 2/3 and 1/3, in the absence of buffer and quenching gases. Each absorbed photon adds to the atom $+1/3$ angular momentum. In the presence of sufficient buffer gas pressure there is collisional mixing in the excited state and the number densities of Zeeman's levels result equal.
The atoms then "democratically" decay to the ground state with equal probability of decaying to the $m_J = -1/2$ and $m_J = +1/2$ sublevels, and on average each absorbed photon adds 1/2 angular momentum to the atom.
Defining the number densities $\rho_{-1/2}$ and $\rho_{+1/2}$ of atoms with $m_J = -1/2$ and $m_J = +1/2$ in the ground state, respectively, we can write the rates of change of these number densities:

$$\frac{d}{dt}\rho_{+1/2} = +2aR_{OP}\rho_{-1/2} \tag{3.13}$$

$$\frac{d}{dt}\rho_{-1/2} = -2R_{OP}\rho_{-1/2} + 2(1-a)R_{OP}\rho_{+1/2} \tag{3.14}$$

The total density is constant, in other words $\rho_{-1/2}+\rho_{+1/2} = 1$, since the atoms spend significantly more time in the ground state than in the excited state. With this formalism $\rho_{-1/2}$ and $\rho_{+1/2}$ can be interpreted as the occupational probabilities of the $m_J = -1/2$ and $m_J = +1/2$ sublevels of the ground

state.
The spin polarization of the atoms $\langle S_z \rangle$ is given by

$$\langle S_z \rangle = \frac{1}{2} \left[\rho_{+1/2} - \rho_{-1/2} \right] \tag{3.15}$$

while its rate of change is

$$\frac{d}{dt} \langle S_z \rangle = 2aR_{OP}\rho_{-1/2} = aR_{OP}(1 - 2\langle S_z \rangle) \tag{3.16}$$

The average photon absorption rate per atom is

$$\langle \Gamma_{OP} \rangle = 2R_{OP}\rho \left(-\frac{1}{2} \right) = R_{OP}(1 - 2\langle S_z \rangle) \tag{3.17}$$

For a boundary condition of no polarization, $\langle S_z \rangle = 0$ at time $t = 0$, we have

$$\langle S_z \rangle = \frac{1}{2} \left(1 - e^{-2aR_{OP}t} \right) \tag{3.18}$$

3.4 Faraday's rotation

Magneto-optics was born in 1845 with an experiment performed by Faraday on the interaction between light and magnetic field within a medium. Let's consider the propagation effects of an electromagnetic wave when a static and external $\mathbf{B}_0$ magnetic field is present. For the electrons we have

$$\omega = \frac{eB}{m_e c} \tag{3.19}$$

defined as the frequency of rotation of an electron around the field lines. Along the direction of the field, an electron will experience a force equal to

$$m_e \frac{d\mathbf{v}}{dt} = -e \left(\mathbf{E} + \frac{\mathbf{v}}{c} \times \mathbf{B_0} \right) \tag{3.20}$$

If the electromagnetic wave is sinusoidal and circularly polarized, we find

$$\mathbf{E}(t) = E_0 e^{-i\omega t} (\varepsilon_1 \pm \varepsilon_2) \tag{3.21}$$

in which the signs $-$ and $+$ correspond respectively to left circular polarization (LCP) and right circular polarization (RCP). In this case the dielectric constant is not a scalar but a tensor whose value depends on the direction

of the waves. Assuming that the wave travels along the direction of the magnetic field, we have

$$\mathbf{v}(t) = -\frac{ie}{m_e(\omega \pm \omega_B)}\mathbf{E}(t) \tag{3.22}$$

through which it is possible to obtain a dielectric constant value equal to

$$\varepsilon_{RL} = 1 - \frac{\omega_p^2}{\omega(\omega \pm \omega_B)}\mathbf{E}(t) \tag{3.23}$$

In the presence of a magnetic field, the medium discriminates between the polarization directions and the two values of the dielectric constant will provide two different refractive indices

$$(n_r)_R L = \sqrt{1 - \left(\frac{v_p}{v}\right)^2 \frac{1}{1 \pm (v_B/v)} \cos\vartheta} \tag{3.24}$$

where ϑ represents the angle between the wave propagation direction and the magnetic field. There are two different speeds for each of the orthogonal modes and furthermore, being a polarized plane wave, a linear superposition of waves with left and right circular polarization, it will have a polarization plane that does not remain constant but rotates together with the wave due to the Faraday's effect. The electric vector of the circularly polarized wave, traveling for a distance d, rotates by a phase angle $\Phi = \mathbf{k} \cdot \mathbf{d}$. If the wave number k is not constant, the phase angle between the two polarization directions turns out to be

$$\Phi_R, L = \int_0^d k_R, L dl = \int_0^d \frac{w}{c}\sqrt{\varepsilon_R, L} \tag{3.25}$$

If we assume ωB and ωp, it is possible to approximate the wave number along the two polarization directions as

$$K_R, L \approx \frac{\omega}{c}\left[1 - \frac{\omega_p^2}{2\omega^2}\left(1 \mp \frac{\omega_B}{\omega}\right)\right] \tag{3.26}$$

A polarized plane wave will be rotated by an angle $\Delta\vartheta$, having a value equal to half ϕ_R, L:

$$\Delta\vartheta = \frac{1}{2}\Phi_R L = \frac{2\pi^3}{m_e^2 c^2 \omega^2}\int_0^d n_l B_{||} dl \tag{3.27}$$

We define the measure of rotation as the following quantities

$$\Delta\vartheta \approx \lambda^2 R.M. \tag{3.28}$$

From which a rotation angle value of approx

$$\langle H_{||} \rangle \propto \frac{R.M.}{D.M.} \propto \frac{\int n_e B_{||} dl}{\int n_e dl} \tag{3.29}$$

The magnetic field can be determined by means of the rotation measurement.

3.5 Optical polarization rotation

Measuring the Larmor's precession frequency of the atomic spins in a magnetometer, the amplitude of the ambient magnetic field is given by

$$B = \frac{\omega_L}{\gamma} \tag{3.30}$$

An oscillating radio-frequency (RF) magnetic field applied transverse to the static ambient field will induce resonant, coherent precession of the polarized atomic spins if the oscillation frequency is approximately equal to the Larmor's frequency [21]. In particular, in scalar magnetometers, we do not find appreciable effects when the orientation changes, except for the so called heading errors and dead zones, effects that are related to particular orientation of the setup respect to the static field.
The magnetometer response should be linear in the amplitude.
We must apply the rotating wave approximation and consider the spin response in the co-rotating reference frame.
An oscillating field $\mathbf{B}' = B' \cos(\omega t)\widehat{y}$ has two counter-propagating rotational components at frequencies $\pm\omega$ with amplitudes B_0.
The ambient magnetic field is given by

$$\mathbf{B}_0 = \frac{\omega_0}{\gamma}\widehat{z} \tag{3.31}$$

We assume that the magnetic linewidth is smaller than the resonance frequency, $\Delta\omega \ll \omega_0$ and the oscillation frequency ω is closer to $+\omega_0$ than to $-\omega_0$. In the reference frame, which is co-rotating with the precessing spin, three effects can be detected:
1 - We may make the rotating wave approximation and neglect all oscillations which are at frequencies far from the rotation frequency, including particularly the counter-rotating component of the oscillating field at $-\omega$.
2 - The static field $\mathbf{B}_0$ is replaced by an effective field

$$\widetilde{\mathbf{B}}_0 = \left(B_0 - \frac{\omega}{\gamma}\right)\widehat{z} \tag{3.32}$$

3 - The co-rotating component of the oscillating field is static in this reference frame.
The total effective magnetic field is

$$\widetilde{\mathbf{B}}_0 = \frac{(\omega_0 - \omega)}{\gamma}\widetilde{z} + \frac{B'}{2}\widetilde{\mathbf{y}} \tag{3.33}$$

The Bloch's equation in this reference frame is

$$\frac{d}{dt}\widetilde{\mathbf{S}} = \gamma\widetilde{\mathbf{B}} \times \widetilde{\mathbf{S}} - \widetilde{\mathbf{B}}_0 =$$

$$\frac{(\omega_0 - \omega)}{\gamma}\widetilde{z} + \frac{B_0}{2}\widetilde{y} \tag{3.34}$$

where T_1 and T_2 are the longitudinal and transverse spin coherence lifetimes and $S_0 = S_0\widehat{z}$ is the equilibrium atomic spin polarization in the absence of the oscillating excitation field. The steady state solution for the three individual components is given by

$$\widetilde{S}_x = \frac{S_0(\frac{\gamma B'}{2})T_2}{1 + (\frac{\gamma B'}{2})^2 T_1 T_2(\omega - \omega_0)^2 T_2^2} \tag{3.35}$$

$$\widetilde{S}_y = \frac{-S_0(\omega - \omega_0)(\frac{\gamma B'}{2})T^2}{1 + (\frac{\gamma B'}{2})^2 T_1 T_2(\omega - \omega_0)^2 T_2^2} \tag{3.36}$$

$$S_z = \frac{S_0(1 + (\omega - \omega_0 T_2^2)^2)}{1 + (\frac{\gamma B'}{2})^2 T_1 T_2 + (\omega - \omega_0)^2 T_2^2} \tag{3.37}$$

The probe beam signal is proportional to S_x as measured in the lab frame. The amplitude of the transverse polarization is proportional to the strength of the applied RF field, and large fields are necessary to measure the coherence frequency precisely. The magnetic linewidth is given by

$$\Delta\omega = r \tag{3.38}$$

Large RF excitation amplitudes lead to broadening of the resonance line and decreased magnetometer sensitivity. The amplitude should therefore be chosen to enable a large coherence signal without greatly affecting the linewidth. The magnetometer response is proportional to the polarization S_0 along the magnetic field direction. The signal is largest when the pumping axis and magnetic field are parallel, and it drops to zero as the axis and field become orthogonal.

3.6 The effect of hyperfine splitting

As illustrated in the next paragraph, a high sensitivity magnetometry requires detection of extremely small optical rotation angles. Suppose that the ground and excited-state hyperfine splitting are optically resolved. It is possible to calculate the optical rotation signal resulting from each of the transitions $F \to F'$ for the optical absorption cross-section.

On or near resonant light slightly shifts the atomic Zeeman's energy levels as a result of two effects, the light shifts due to virtual transitions and real transitions. We can observe the AC Stark's shift due to the oscillating electric field of the light wave.

The Hamiltonian describing atomic interaction with the light is

$$\delta H = \Delta E_v - \frac{i\hbar}{2}\langle\Gamma\rangle = -\mathbf{E}^* \cdot \alpha(\nu)\mathbf{E} \tag{3.39}$$

where ΔE_v is the energy level shift, and $\alpha(\nu)$ is the atomic polarizability.

The polarizability is complex and its real and imaginary components are Kramers-Kronig's transforms of each other.

This equation for arbitrary direction of light propagation becomes

$$\langle\Gamma\rangle = \sigma(\nu)\Phi(1 - 2\mathbf{s}\cdot\mathbf{S}) \tag{3.40}$$

where $\mathbf{s}$ is the photon spin vector, $\mathbf{S}$ is the atomic spin vector, Φ is the photon flux, and $\sigma(\nu)$ is the absorption cross-section.

By the Kramers-Kronig's relations for the energy shift, we obtain

$$\begin{aligned}\Delta E_v &= \frac{\hbar}{2}\Phi(1 - 2\mathbf{s}\cdot\mathbf{S})\frac{1}{\pi}\mathcal{P}\int_{\infty}^{\infty}\frac{\pi r_e c f Re[\mathcal{V}(\nu' - \nu_0)]}{\nu' - \nu}d\nu' \\ &= \frac{\hbar}{2}\pi r_e c f \Phi(1 - 2\mathbf{s}\cdot\mathbf{S})Im[\mathcal{V}(\nu - \nu_0)]\end{aligned} \tag{3.41}$$

Treating the AC Stark's shift as if it were due to a fictitious magnetic field $\mathbf{B}_{LS}$ in the direction of the photon spin and ignoring constant terms, the energy shift is

$$\Delta E_\nu = \hbar\gamma^e \mathbf{B}_{LS}\cdot\mathbf{S} \tag{3.42}$$

where $\gamma^e = g_s\frac{\mu_B}{\hbar}$ is the gyromagnetic ratio of the electron, and the fictitious magnetic field is

$$\mathbf{B}_{LS} = \frac{-\pi r_e c f \Phi}{\gamma^e}Im[\mathcal{V}(\nu - \nu_0)]\mathbf{s} \tag{3.43}$$

The alkali atoms respond to the field $\mathbf{B}_{LS}$ as if it were a real magnetic field. In fact, they precess about the total effective field $\mathbf{B} = \mathbf{B}_0 + \mathbf{B}_{LS}$, where $\mathbf{B}_0$

is the ambient field.
The probe beam is linearly polarized, so that $s = 0$ and the AC Stark's shift is indeed eliminated.
By observing the response of the alkali spins to the field, we can characterize a magnetic field. The coupling of the electron spin to a magnetic field is given by the Hamiltonian

$$\mathcal{H} = \gamma\hbar\mathbf{B}\cdot\mathbf{S} \tag{3.44}$$

The response of the spin to the magnetic field is

$$\frac{d}{dt}\mathbf{S} = \frac{i}{\hbar}[\mathbf{H},\mathbf{S}] \tag{3.45}$$

Due to commutation rules of the components of S:

$$\frac{d}{dt}S_z = \frac{i}{\hbar}\gamma\hbar B_x[S_x,S_z] + B_y[S_y,S_z]) = i\gamma(-iB_xS_x + iB_yS_x) \tag{3.46}$$

with similar equations for S_x and S_y.
By the formula of classical equation for a dipole in a magnetic field, the spin precession is given by

$$\frac{d}{dt}\mathbf{S} = \gamma\mathbf{B}\times\mathbf{S} \tag{3.47}$$

The electron spins, forced to drag the nuclear spin along with it as it precesses, and nuclear spins of the atom act as coupled oscillators. In this way a slower precession occurs respect to a bare electron

$$\gamma = \frac{\gamma^e}{2I+1} \tag{3.48}$$

where $\gamma^e g_s\mu_B = 2\pi\times 2.8\frac{MHz}{G}$ is the gyromagnetic ratio of the bare electron.
The Bloch's equation describes the evolution of the atomic spin

$$\frac{d}{dt}\mathbf{S} = \gamma\mathbf{B}\times\mathbf{S} + \frac{1}{q}\left[R_{OP}\left(\frac{1}{2}s\widehat{z} - \mathbf{S}\right) - \mathbf{R}_{rel}\mathbf{S}\right] \tag{3.49}$$

there q is the nuclear slowing-down factor, which depends on the polarization of the sample and tends to $2I+1$ for perfect polarization. The second term describes the effect of optical pumping to polarize the spin along the $\hat{z}$ axis and the third term describes the effect of spin relaxation to depolarize the spin.
The equilibrium of spin polarization S_0, in absence of any magnetic field, is

$$S_0 = \frac{sR_{OP}}{2(R_{OP}+R_{rel})} \tag{3.50}$$

In order to optimize the magnetometer sensitivity, we maximize the spin polarization lifetime, so it is possible to minimize the magnetic linewidth.

3.7 Optical polarimetry

Consider for our purpose the case of either D1 or D2 transition. In the D1 line the optical pumping with light of arbitrary polarization $\hat{\epsilon}$, the average photon spin s is given by

$$\mathbf{s} = i\widehat{\epsilon} \times \widehat{\epsilon}^* \tag{3.51}$$

It is convenient to characterize the light polarization by the photon spin component along the pumping direction, $s = \mathbf{s} \cdot \widehat{z}$; s ranges from -1 to $+1$, where $s = -1$ corresponds to $\sigma-$ light, $s = 0$ corresponds to linearly polarized p light, and $s = +1$ corresponds to $\sigma+$ light.
The absorption rate for an unpolarized atom is $R = \sigma(\nu)\Phi$, while the optical pumping rate equations are

$$\frac{d}{dt}\rho_{-1/2} = \\ = -(1+s)R\rho_{-1/2} + (1-a)(1+s)R\rho_{-1/2} + a(1-s)R\rho_{+1/2} \tag{3.52}$$

$$\frac{d}{dt}\rho_{+1/2} = \\ = -(1-s)R\rho_{+1/2} + (1-a)(1-s)R\rho_{+1/2} + a(1+s)R\rho_{-1/2} \tag{3.53}$$

where a is the optical pumping efficiency.
The evolution of the spin can be written as

$$\frac{d}{dt}\langle S_z\rangle = aR(s - 2\langle S_z\rangle) - R_{rel}\langle S_z\rangle \tag{3.54}$$

and the solution for an initially unpolarized atom is

$$\langle S_z\rangle = s\frac{aR}{2aR + R_{rel}}\left(1 - e^{-\frac{2aR+R_{rel}}{t}}\right) \tag{3.55}$$

The average photon absorption rate per atom is given by

$$\langle\Gamma\rangle = R\left[(1+s)\rho_{-1/2} + (1-s)\rho_{+1/2}\right] = R\left(1 - 2s\langle S_z\rangle\right) \tag{3.56}$$

and for case D2 light is

$$\langle\Gamma\rangle_{D2} = R\left[1 - \frac{1}{2}s\rho_{-1/2} + \left(1 + \frac{1}{2}s\right)\rho_{+1/2}\right] = R\left(1 + s\langle S_z\rangle\right) \tag{3.57}$$

The photon becomes partially or completely absorbed by the alkali vapor, as on or near-resonant light propagates through the vapor cell. The attenuation of the light results in non-uniform polarization throughout the cell and thus reduce the sensitivity of the magnetometer. Monitoring the spin precession due to the field is required to detection of a magnetic field.
The probe beam propagates along the $\widehat{\mathbf{x}}$ direction, orthogonal to the pump beam. Its plane of polarization rotates by an angle $\vartheta \propto \langle S_x \rangle$ due to a difference in the indices of refraction $n_+(\nu)$ and $n_-(\nu)$ experienced by $\sigma+$ and $\sigma-$ light, respectively.
The polarization of the light is compared before and after traveling through the cell, yielding a measurement of the projection of the atomic spin along the propagation direction. This method works better with the electron spin S_x. See Appendix 3 for more details.

3.8 Spin relaxations

Spin-relaxation mechanisms are due to collisions with buffer gas atoms, quenching gas molecules, and other alkali atoms.
A RF-AM measure is based on the changes in the precession generated by Zeeman's transitions.
Suppose the total magnetic field $\mathbf{B}$ lies along the $\widehat{z}$ axis such the polarization lifetime can be characterized by the lifetime T_1 of the longitudinal component $\langle F_z \rangle$ and the lifetime T_2 of the transverse components $\langle F_x \rangle$ and $\langle F_y \rangle$.
The general rate for a collision is

$$R = n\sigma\overline{v} \tag{3.58}$$

where n, σ and v are, respectively, the density of the other gas species, the effective collisional cross-section and the relative thermal velocity.
Coherence destruction causes spin relaxation; we are interested in measuring the spin coherence of precessing atoms.
Most spin-relaxation mechanisms cause depolarization of the electron spin while leaving the nuclear spin unaffected.
The maintaining total atomic spin is characterized by the nuclear slowing-down factor q, which depends on the polarization of the ensemble. Magnetic field is arbitrarily oriented respect to the pumping and probing axes.
The longitudinal lifetime is given by the rates of the various mechanisms

which affect the expectation value of the spin component along the quantization axis. It is defined by the direction of the magnetic field

$$\frac{1}{T_1} = \frac{1}{q}\left(R_{SD} + R_{OP} + R_{pr}\right) + R_{wall} \tag{3.59}$$

so we obtain the rate of relaxation due to spin-destruction collisions

$$R_{SD} = R_{SD}^{Self} \tag{3.60}$$

where the term on the right is due to collision with other alkali atoms.
Probe photons are polarized along a direction orthogonal to the pump beam. The polarization of an atom is destroyed upon absorption because the individual photons have arbitrary helicity.
The transverse components of the atomic spin precess in the magnetic field. Any mechanisms that cause de-phasing between precessing atoms, contribute to relaxation of the average transverse polarization of the ensemble, without affecting the longitudinal component.
The mechanisms which relax the longitudinal component also relax the transverse components because they randomize the spin direction. The transverse polarization lifetime is

$$\frac{1}{T_2} = \frac{1}{T_1} + \frac{R_{SE}}{q_{SE}} + R_{gr} \tag{3.61}$$

where R_{SE} is the rate of spin-exchange collisions between alkali atoms, and R_{gr} is the broadening due to the magnetic field gradient across the vapor cell; q_{SE} is the broadening factor, which characterizes the contribution of spin-exchange collisions to the polarization lifetime T_2.
The spin-exchange collisions between alkali atoms are the dominant cause of spin relaxation, at high alkali densities.
In a collision, the direction of the electron spins of the two atoms can be reversed while the total spin is conserved, i.e.

$$A(\uparrow) + B(\downarrow) \Rightarrow A(\downarrow) + B(\uparrow) \tag{3.62}$$

Spin-exchange collisions are sudden with respect to the hyperfine interaction and so do not affect the nuclear spin of the colliding atoms. As a result of the collision, atoms may change hyperfine states.
Spin exchange collisions provoke a redistribution of the atoms among the atomic m_F Zeeman's sublevels while preserving the total atomic spin.

Atoms in the two ground-state hyperfine levels precess with approximately the same frequency, but in opposite directions

$$\omega_+ = \gamma|\mathbf{B}| = -\omega_- \tag{3.63}$$

where the subscripts denote the hyperfine levels $F = I \pm 1/2$.
Therefore, the populations of the two hyperfine levels de-cohere as they precess, causing relaxation of the transverse spin components. The broadening factor q_{SE} at high magnetic field becomes

$$\frac{1}{q_{SE}} = \frac{2I(2I-1)}{3(2I+1)^2} \tag{3.64}$$

When the alkali vapor density is high enough that the spin-exchange rate is much larger than the optical pumping rate or other spin-relaxation mechanisms, the atomic spins arrive at an equilibrium state described by the spin-temperature distribution. A very important mechanism for spin relaxation is spin-destruction collisions.
Collisions between alkali atoms transfer spin angular momentum to the rotational angular momentum of the colliding pair of atoms. The alkali-alkali spin destruction collision in which spin-polarisation of the vapor is not conserved can be described by this simple expression:

$$A(\uparrow) + B(\downarrow) \Rightarrow A(\downarrow) + B(\downarrow) \tag{3.65}$$

3.8.1 Wall collisions

When alkali atoms encounter the cell wall, they are adsorbed into the glass surface for a limited time before being ejected back.
The atoms experiences the large local electric and magnetic fields produced by ions and molecules within the glass; these are variable in time.
Wall collisions are completely depolarizing and can dominate all other spin-relaxation mechanisms unless suppressed.
The atoms move in straight lines in between collisions with the cell walls.
Indicating with m the mass of the atom, the average thermal velocity is

$$\overline{v} = \sqrt{\frac{8k_BT}{\pi m}} \tag{3.66}$$

while the average time between collisions with the cell walls is

$$T_{wall} = \frac{4V}{\overline{v}A} \tag{3.67}$$

with V is the cell volume and A is the surface area.
In smaller cells, the effect of wall depolarization are more pronounced, as the lifetime scales linearly with the characteristic length of the cell.

3.9 Bloch's equations description

Consider the total atomic spin vector, $F = [F_x, F_y, F_z]$, indicating with F the sum of all the individual atomic spins that contribute to the magnetometer signal. Assuming that any transverse perturbations to the field are small compared to the static field, the evolution of $\mathbf{F}$ in an external magnetic field $\mathbf{B}$ is given by

$$\frac{d\mathbf{F}}{dt} = \gamma \mathbf{F} \wedge \mathbf{B} - \frac{F_x \widehat{\mathbf{x}} + F_y \widehat{\mathbf{y}}}{T_2} - \frac{F_z - F_0}{T_1} \widehat{\mathbf{z}} \tag{3.68}$$

where $\widehat{\mathbf{x}}$,$\widehat{\mathbf{y}}$, $\widehat{\mathbf{z}}$ are the unit vectors in the laboratory frame and γ is the gyromagnetic ratio.
The terms on the right hand side of Equation 3.68 are, respectively, the equation of motion for free spins, the decay of any transverse spin components at a rate $1/T_2$. With T_2 we indicate the transverse relaxation time, and the trend towards an equilibrium value ($F_z = F_0$) in the z-direction, at a rate $1/T_1$, while T_1 is the longitudinal relaxation time.
In this Thesis, we assume T_2 as the transverse spin relaxation time, affected by a number of processes.
The total field is the sum of the static bias field and the RF field $-\mathbf{B} = \mathbf{B}_{bias} + \mathbf{B}_{RF}$; a resonant Zeeman transition frequency ω_0 via the Zeeman effect results.
Consider the RF field applied along y-direction to be linearly polarised and oscillating at a frequency ω with an amplitude $2B_1 = 2\omega_L/\gamma$ (i.e. $\mathbf{B}_{RF} = 2B_1 \cos \omega t$).
Moving to the rotating frame, about $\widehat{\mathbf{z}}$ at frequency ω, the total effective field is

$$\mathbf{B_{eff}} = \left(B_{bias} \widehat{\mathbf{z}} + \frac{\omega}{\gamma} \right) \widehat{\widetilde{\mathbf{z}}} + B_1 \widehat{\widetilde{\mathbf{y}}} = \frac{\Delta\omega \widehat{\widetilde{\mathbf{z}}} + \omega_1 \widehat{\widetilde{\mathbf{z}}}}{\gamma} \tag{3.69}$$

where $\Delta\omega = (\omega - \omega_0)$ is the detuning of the RF field from the resonance and the unit vectors in the rotating frame are $\widehat{\widetilde{\mathbf{x}}}, \widehat{\widetilde{\mathbf{y}}}, \widehat{\widetilde{\mathbf{z}}} = \widehat{\mathbf{z}}$. Bloch's equation in the rotating frame becomes

$$\frac{d\widetilde{\mathbf{F}}}{dt} = \gamma \widetilde{\mathbf{F}} \wedge \mathbf{B_{eff}} - \frac{\widetilde{F}_x \widehat{\widetilde{x}} + \widetilde{F}_y \widehat{\widetilde{y}}}{T_2} \frac{\widetilde{F}_z - F_0}{T_1} \widehat{\widetilde{\mathbf{z}}} \tag{3.70}$$

where the tilde terms $\sim$ are the spin components.
By combining the two last equations, we find

$$\begin{pmatrix} \frac{d\widetilde{F}_x}{dt} \\ \frac{d\widetilde{F}_y}{dt} \\ \frac{d\widetilde{F}_z}{dt} \end{pmatrix} = \begin{pmatrix} -\frac{1}{T_2} & \Delta\omega & -\omega_1 \\ -\Delta\omega & -\frac{1}{T_2} & 0 \\ \omega_1 & 0 & -\frac{1}{T_1} \end{pmatrix} \begin{pmatrix} \widetilde{F}_x \\ \widetilde{F}_y \\ \widetilde{F}_z \end{pmatrix} = \begin{pmatrix} 0 \\ 0 \\ \frac{F_0}{T_1} \end{pmatrix} \tag{3.71}$$

The general solution is given by a series of exponential terms of the form $\widetilde{\mathbf{F}} = \mathbf{v}e^{\lambda t} + \mathbf{c}(t)$, where λ and $\mathbf{v}$ are the eigenvalues and eigenvectors of the matrix.

3.9.1 Steady-state solutions to the Bloch's equations

Assuming that sufficient time has elapsed to consider the steady-state solution of the Bloch's equations, it results

$$\frac{d\widetilde{F}_x}{dt} = \frac{d\widetilde{F}_y}{dt} = \frac{d\widetilde{F}_z}{dt} = 0 \tag{3.72}$$

The resulting linear system is

$$\widetilde{F}_x = \frac{\omega_1 T_2}{1 + \omega_1^2 T_1 t_2 + \Delta\omega^2 T_2^2} F_0 \tag{3.73}$$

$$\widetilde{F}_y = \frac{-\omega_1 \Delta\omega T_2^2}{1 + \omega_1^2 T_1 T_2 + \Delta\omega^2 T_2^2} F_0 \tag{3.74}$$

$$\widetilde{F}_z = \frac{1 + \Delta\omega^2 T_2^2}{1 + \omega_1^2 T_1 T_2 + \Delta\omega^2 T_2^2} F_0 \tag{3.75}$$

Substituting $\omega_1 = \gamma B_1$ we find

$$\widetilde{F}_x = \frac{\gamma B_1 T_2}{1 + \gamma^2 B_1^2 T_1 T_2 + \Delta\omega^2 T_2^2} F_0 \tag{3.76}$$

$$\widetilde{F}_y = \frac{-\gamma \Delta\omega B_1 T_2^2}{1 + \gamma^2 B_1^2 T_1 T_2 + \Delta\omega^2 T_2^2} F_0 \tag{3.77}$$

$$\widetilde{F}_z = \frac{1\Delta\omega^2 T_2^2}{1 + \gamma^2 B_1^2 T_1 T_2 + \Delta\omega^2 T_2^2} F_0 \tag{3.78}$$

3.10 Predicted resonance line shapes

By the probe beam, we detect the spin component $\widetilde{F}_x = \widetilde{F}_x \cos(\omega t) + \widetilde{F}_y \cos(\omega t)$. A dual-phase lock-in amplifier, referenced to the driving RF field at ω, is able to extract these two components from the probe beam: the term $(\widetilde{F}_x)$ is absorptive contribution while the term $(\widetilde{F}_y)$ is dispersive contribution.
The resonant line shapes refer to the shape of the components e $\widetilde{F}_x$ and e $\widetilde{F}_y$ as the driving RF field (ω) moves through the resonant frequency (ω_0).
By defining the full-width-half-maximum (FWHM),

$$\Gamma = \frac{2}{T_2}\sqrt{1 + \gamma^2 B_1^2 T_1 T_2} \tag{3.79}$$

the line shapes are given by Lorentzian distributions of the form

$$\widetilde{F}_x(\omega) = \frac{2A}{\pi}\left[\frac{\Gamma}{4(\omega - \omega_0)^2} + \Gamma^2\right] \tag{3.80}$$

and

$$\widetilde{F}_y(\omega) = \frac{2A}{\pi}\left[\frac{\Gamma(\omega - \omega_0)}{4(\omega - \omega_0)^2} + \Gamma^2\right] \tag{3.81}$$

which are centred at the resonant frequency $-\omega$.
The absorptive $(\widetilde{F}_x)$ component is a Lorentzian, whereas the dispersive e $(\widetilde{F}_y)$ component is an anti-Lorentzian function. As we have just said, the sensitivity of an RF-AM is inversely proportional to the gradient of the dispersive curve.
It is clear that this gradient, and therefore the sensitivity, is maximised at resonance. The maximum value is given by

$$\frac{d\widetilde{F}_y}{d\omega}|_{\omega=\omega_0} = \frac{-\gamma B_1 T_2^2 F_0}{(1 + \gamma^2 B_1^2 T_1 T_2)} \tag{3.82}$$

From this it is easy to show that the optimum RF field amplitude, that maximises the gradient, is $B_1 = B_{ideal}$, where

$$B_{ideal} = \frac{1}{\gamma\sqrt{T_1 T_2}} \tag{3.83}$$

At this point the maximum dispersive gradient is d e F_y

$$\frac{d\widetilde{F}_y}{d\omega}|_{\omega=\omega_0,max} = \frac{-F_0 T_2^{\frac{3}{2}}}{2\sqrt{T_1}} \tag{3.84}$$

3.10.1 RF-AM linewidth

The FWHM (Equation 3.79) increases with RF field amplitude.
At B_{ideal}, the FWHM reduces to

$$\Gamma = \frac{2\sqrt{2}}{T_2} \tag{3.85}$$

Therefore, the linewidth of the magnetometer response, at the position of peak sensitivity, is narrowed by increasing the lifetime of the transverse spin component.
Maximum peak of the absorptive profile occurs at resonance ($Dw = 0$),

$$max(\widetilde{F}_x) = \frac{\gamma B_1 T_2 F_0}{1 + \gamma^2 B_1^2 T_1 T_2} \tag{3.86}$$

The B_{ideal} is

$$max(\widetilde{F}_x) = \frac{F_0}{2}\sqrt{\frac{T_2}{T_1}} \tag{3.87}$$

Below B_{ideal} the amplitude of the absorptive peak increases towards the maximum.
Beyond it, the amplitude steadily decays towards zero in the asymptotic limit.
The peaks of the dispersive profile are found at the turning points of e $\widetilde{F}_y(\omega)$.
These are given by

$$\Delta\omega = \pm\frac{1}{T_2}\sqrt{1 + \gamma^2 B_1^2 T_1 T_2} = \pm\frac{\Gamma}{2} \tag{3.88}$$

The amplitudes at these points are found to be

$$\pm\frac{\gamma B_1 F_0}{\Gamma} \tag{3.89}$$

In contrast to the absorptive profile, the peaks of the dispersive profile continue increasing with RF amplitude to an asymptotic limit. This limit has the same value as Equation 3.87. It can be found by substituting for G in Equation 3.89, pulling out the square-root and applying the power rule

$$\lim_{B_1 \to \infty}(\pm\sqrt{\frac{\gamma^2 B_1^2 T_2^2 F_0^2}{4(1 + \gamma^2 B_1^2 T_1 T_2)}}) = \pm\frac{F_0}{2}\sqrt{\frac{T_2}{T_1}} \tag{3.90}$$

3.11 The Density Matrix Formalism

In atomic Magnetometry, to model the evolution of so many independent wave-functions, we usually determine the statistical average of the spin operator. The N atoms of an ensemble are in a mixed state, so it is possible to use an overall wave-function.
By the Density Matrix we may characterize the populations of the ground-state levels and the coherences between the levels [61], [11].
The density operator is

$$\rho = \frac{1}{N}\sum_n |\phi_n\rangle\langle\phi_n| \tag{3.91}$$

In basis of state $\langle j|j\rangle$, the normalized total population

$$\sum_j \langle j|j\rangle = \sum_j |j\rangle\langle j| = 1 \tag{3.92}$$

Considering an observable X, the average value over the ensemble is

$$\langle X\rangle = \frac{1}{N}\sum_n \langle\phi_n|X|\phi_n\rangle = \frac{1}{N}\sum_n\sum_j \langle\phi_n|X|j\rangle\langle j|\phi_n\rangle =$$

$$= Tr[X\rho] = Tr[\rho X] \tag{3.93}$$

The evolution of the atomic wave function may be written as

$$i\hbar\frac{d}{dt}|\phi_n\rangle = \mathcal{H}|\phi_n\rangle \tag{3.94}$$

$$-i\hbar\frac{d}{dt}\langle\phi_n| = \langle\phi_n|\mathcal{H} \tag{3.95}$$

$\mathcal{H}$ is the atomic Hamiltonian.
The time evolution of the density matrix is given by Liouville's equation

$$\frac{d}{dt}\rho = \frac{1}{N}\sum_n \frac{d}{dt}|\phi_n\rangle\langle\phi_n| = \frac{1}{N}\sum_n \left[(\frac{d}{dt}|\phi_n\rangle)\langle\phi_n| + |\phi_n\rangle(\frac{d}{dt}\langle\phi_n|)\right]$$

$$= \frac{1}{N}\sum_n \left[\frac{1}{i\hbar}\mathcal{H}|\phi_n\rangle\langle\phi_n| - \frac{1}{i\hbar}|\phi_n\rangle\langle\phi_n|\mathcal{H}\right] = \frac{1}{i\hbar}[\mathcal{H},\rho] \tag{3.96}$$

in which we have the commutator $[\mathcal{H},\rho] = \mathcal{H} - \rho - \rho\mathcal{H}$.
The density operator is given by

$$\rho_{jk} = \langle k|\rho|j\rangle = \frac{1}{N}\sum_n \langle k|\phi_n\rangle\langle\phi_n|j\rangle \tag{3.97}$$

We can consider the wave-function of a spin $-1/2$ particle in spinorial for

$$|\psi\rangle = \begin{pmatrix} c_1 \\ c_2 \end{pmatrix} \tag{3.98}$$

$$\langle\psi| = \begin{pmatrix} |c_1| & c_1^* \end{pmatrix} \tag{3.99}$$

The density matrix is

$$|\phi\rangle = \begin{pmatrix} |c_1|^2 & c_1 c_2^* \\ c_1^* c_2 & |c_2|^2 \end{pmatrix} \tag{3.100}$$

The diagonal element $\rho_{ij} = \langle j|\rho|j\rangle$ is the population of the state $|j\rangle$.
$Tr[\rho] = 1$ so that the total population of all states is normalized.
The ground-state sublevel number densities $\rho_{\pm 1/2}$ are given by the matrix elements $\rho_{\pm 1/2,\pm 1/2} = \langle \pm 1/2|\rho| \pm 1/2\rangle$.
The off diagonal elements ρ_{jk} characterize the coherence between states $|j\rangle$ and $|k\rangle$.
In the normal operating regime, the Zeeman's splitting is much smaller than the hyperfine splitting, $\hbar\omega_L \ll E_{hf}$, so the electron and nuclear spins are strongly coupled to the atomic state.
The Dr. Scott Jeffrey Seltzer's PhD, published in 2008 with the title of "Developments in alkali-metal atomic magnetometry", was particularly useful for the detailed understanding of the phenomena described in here [136]. Other calculation details in Appendix 2.

3.12 Fundamental noise limits

Technological improvements have seen AMs overcome many experimental limitations to their sensitivity.
As a result, devices have begun to approach the fundamental limits of sensitivity imposed by quantum mechanics.
These are related to quantum fluctuations in the atomic vapour and probe beam.
This section describes these limitations following the analysis [133].
Here we present an analysis which considers three sources of quantum noise:
1 - The spin-projection noise δB_{spn} due to the finite number of alkali atoms used in the measurement;

2 - The photon shot noise δB_{psn} due to the finite number of probe photons used;
3 - The light-shift noise δB_{lsn} due to fluctuations in the polarization of the probe beam.
The total noise in the magnetic field measurement is given by the quadrature sum of the three individual sources of noise

$$\delta B = \sqrt{\delta B_{spn}^2 + \delta B_{psn}^2 + \delta B_{lsn}^2} \tag{3.101}$$

3.12.1 Spin-projection noise

The quantum mechanical uncertainty of projecting a spin-polarised atom during measurement causes spin-projection noise.
When the measurement basis is orthogonal to the direction of polarisation then the result of the measurement is random.
If the complete spin polarisation is along z, the atomic ensemble can be described as an eigenstate of F_z. The traverse components of atomic spin do not commute

$$[F_x, F_y] = iF_z \tag{3.102}$$

so they experience fluctuations arising from Heisenberg's principle

$$\sigma^2(F_z)\sigma^2(F_y) \geq \frac{|F_z|^2}{4} \tag{3.103}$$

Repeating measurements on an ensemble of N atoms and considering that the alignment of the atoms is destroyed, we can't consider uncorrelated all measurements of polarization rotation. During the interaction with a probe beam, the alignment of an atom is destroyed so the alignment of an atom is destroyed [133] so the spin-projection contribution is

$$\delta B_{spn} = \frac{1}{\gamma}\sqrt{\frac{8}{F_z n V T_2}} \tag{3.104}$$

where V is the effective sensor volume and n is the atomic vapor density.

3.12.2 Photon-shot noise

Photon-shot noise is associated with the measurement of the angle of rotation of the probe beam with a finite number of photons.
For a balanced polarimeter it arises from the uncertainty in the number of

photons in each detection arm. In a balanced polarimeter, the total flux of photons Φ' results as

$$\Phi' = \int_A \Phi dA \tag{3.105}$$

where Φ is taken over the whole area of the probe beam
The optical rotation angle in terms of the fluxes Φ'_1 and Φ'_2 in the two arms of the polarimeter is

$$\theta = \frac{\Phi'_1 - \Phi'_2}{2(\Phi'_1 + \Phi'_2)} \tag{3.106}$$

and assuming the rotation angle to be small, $\Phi'_1 \approx \Phi'_2$. The quantum fluctuation in the number of photons in each channel is

$$\delta\Phi'_1 = \delta\Phi'_2 = \sqrt{\frac{\Phi'}{2}} \tag{3.107}$$

This results in an uncertainty in the angle of rotation of [32]

$$\delta\theta = \sqrt{\frac{1}{2\Phi\eta}} \tag{3.108}$$

where Φ is the photon flux of the probe beam and η is the quantum efficiency of the photodiode.
For the photon-shot noise contribution we finally find

$$\delta B_{psn} = \frac{2\sqrt{2}}{\pi l r_e c f n \gamma T_2 D(\nu)\sqrt{\Phi\eta}} \tag{3.109}$$

where l is the probe beam path in the vapor, r_e the electron classical radius, f the oscillator strength of the transition, $D(\nu)$ the dispersive optical profile of the probe beam.

3.12.3 Light-Shift Noise

The light-shift noise arises from the polarisation fluctuations of the probe beam. The Stark's effect is the electric equivalent of the Zeeman's effect. In practice, its consequence can be considered as due to the presence of a virtual magnetic field, B_{LS}.
For a probe beam on the D2 line, this field is given by [136]

$$B_{LS} = \frac{\pi r_e c f \Phi D(\nu)}{2\gamma^e A} s_x \tag{3.110}$$

where Φ is again the photon flux of the probe beam and γ^e is the gyromagnetic ratio for an isolated electron, A is the cross-sectional area of the probe

beam and s_x is the degree of circular polarisation of the beam.
For the linearly polarised probe $s_x \approx 0$.
The polarization s of the probe beam is given by the fluxes Φ'_- of σ^- photons and Φ'_+ of σ^+ photons in the beam

$$s = \frac{\Phi'_+ - \Phi'_-}{\Phi'_+ + \Phi'_-} \tag{3.111}$$

For linearly polarized light $\Phi'_- \approx \Phi'_+$,

$$\delta\Phi'_- = \delta\Phi'_+ = \sqrt{\frac{\Phi'}{2}} \tag{3.112}$$

$$\delta s_x = \sqrt{\frac{2}{\Phi}} \tag{3.113}$$

3.13 Sensitivity Limits

The sensitivity of a scalar magnetometer is the fundamental parameter stating the smallest magnetic field the device is capable of detecting. Three sources of quantum fluctuation [138] limit the sensitivity. Under optimal conditions $T_2 \sim (R_{SE}R_{SD})^{-1/2}$, it results

$$\delta B_{min} = \frac{0.94}{\gamma}\sqrt{\frac{\sigma_{SE}\overline{v}}{V}\left(1 + \frac{1}{2\eta}\right)} \tag{3.114}$$

where σ_{SE} is the alkali-alkali spin-exchange cross-section, $\overline{v}$ is the thermal velocity, V is the active measurement volume, and $\eta \sim 0.5$ is the quantum efficiency of the photodiodes used to detect the probe beam.
Scalar magnetometer performance can be improved using light narrowing to partially suppress spin-exchange broadening if the sensitivity is limited by technical noise, but the sensitivity is limited by the spin-exchange rate in spite of how narrow the magnetic linewidth becomes.
A precise measurement of the atomic precession frequency requires a large spin coherence between at least two Zeeman's sublevels.
If the magnetic field lies along an axis orthogonal to the pumping direction, each atom is polarized at different instances in time and so precess incoherently with random phases, but because the precession period is much smaller than the spin lifetime, the ensemble has zero average polarization.
On contrary, when the pumping rate is modulated at nearly the Larmor's

frequency, the atoms are pumped at approximately the same time, so they precess coherently with the same phase, and pumping does not occur again until the atomic spins complete one complete precession and are again aligned with the pumping direction.

3.13.1 Detection of Magnetometer sensitivity

The cell geometry, alkali source and the inclusion of coatings, buffer and quenching gases, are relevant choice in high sensitivity operation of RF-AM. The optical pumping rate and the probe beam perturbation depend on the laser beam frequencies and intensities.
For buffer gas cells, the beam waists also define the effective sensing volume. In addition, the vapor density temperature affects the degree of propagation of the beams through the cell. The impact of the strength of the applied RF field on the magnetometer response and its sensitivity are parameters space to be explored to optimise the performance of the sensor.
For the RF-AMs developed in this work the magnetic field noise is by far the most important limiting effect. The dominant contribution to this noise is the power line noise oscillating at $50Hz$.
The majority of previous RF-AMs implementations feature multiple layers of metal shields enclosing the sensor, in order to protect the sensor against magnetic field noise. This expensive approach is infeasible for many field applications.
The sensitivity of a magnetometer can be expressed in two complementary ways, depending on the mode of operation:
- The DC field sensitivity is used when the magnetometer is used as a scalar DC magnetometer.
- The RF field sensitivity is used when the magnetometer is used as an AC magnetometer. Therefore, unless stated otherwise it is this value that is referred to as the sensitivity.
- The intrinsic DC sensitivity of an RF-AM is the smallest detectable shift in $\mathbf{B}_{bias}$, in relation to the gradient of the dispersive slope at the resonant frequency.
The DC sensitivity, at a given operation frequency, is given by [123]

$$\delta B_{dc} = \frac{\hbar}{g_F \mu_B} \frac{\Gamma}{SNR} \tag{3.115}$$

where $\hbar$ is Planck's constant, μ_B is the Bohr's magneton, g_F is the Landé's g-factor ($g = 1/3$ for ^{85}Rb, $g = 1/2$ for ^{87}Rb ([139] (1), [139] (2)), Γ is the FWHM resonance linewidth, and SNR is the signal-to-noise ratio.
The slope of the dispersive response at the resonance frequency is accurately described by the ratio Γ/SNR which implies the sensitivity is inversely proportional to the gradient of the dispersive profile.
The RF field sensitivity is evaluated by determining the factors contributing to the noise in the spectrum of the magnetometer signal.
The total noise floor represents the minimum detection level of an RF field at the calibration frequency [133], [98], i.e.

$$\delta B_{RF} = \frac{B_{RF}}{SNR} \tag{3.116}$$

In both measurements of sensitivity the unit is $T/\sqrt{Hz}$ because the SNR is computed from the square-root of a power spectrum.

Chapter 4

Fundamentals of EMI

An AC magnetic field B_1, the primary field, is applied to induce eddy currents in a sample.
In a conductive sample, a changing magnetic field generates eddy currents which are closed loops of currents flowing, as a consequence of Faraday's law of induction. The density of these currents depends on the dielectric properties of the sample and its geometry.
The Lenz's law determines that this flow of electrons creates an additional oscillating magnetic field component, the secondary field, B_2, opposing the primary one. Information regarding the properties of the sample is passed to B_2 and determines the behaviour of eddy current flow.
The secondary field perturbs the primary field, so the effects of interaction are combined in the total field B_{tot} detected by a magnetic field sensor. The details of B_2 can be inferred and the electromagnetic properties of the sample extracted. The major difficulty in this process is due to the fact that the magnitude of the secondary field is much smaller than the one of the primary field. The results presented in this Chapter were obtained by Dr. C. Deans in his PhD Thesis "Electromagnetic Induction Imaging with Atomic Magnetometers" (2018) [41].

4.1 Skin effect

The phenomenon of eddy current flow induces in a metal the "skin effect". The current density is concentrated close to the surface and decreases exponentially with depth. This can be described in two related ways:
1 - The flow of eddy currents produces a secondary field response that op-

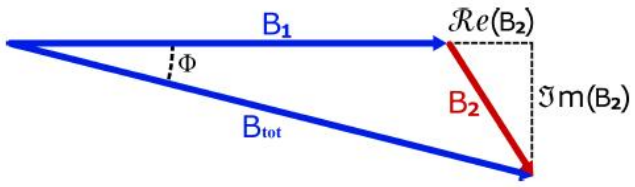

Figure 4.1: Electromagnetic induction imaging. Image courtesy: C. Deans, Department of Physics and Astronomy, UCL - PhD Thesis (2018)

poses the primary field;
2 - It is possible to consider the skin effect as a consequence of the conversion of energy from the primary field into eddy current flow [99]. Suppose the

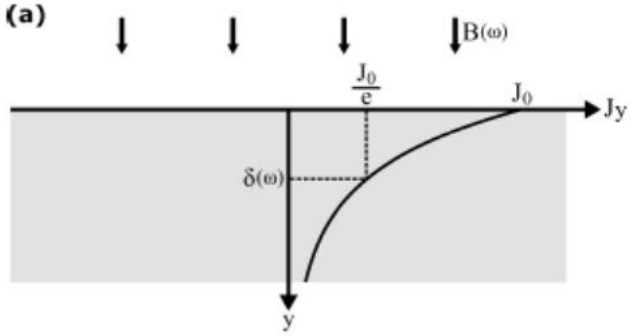

Figure 4.2: Plane wave of angular frequency ω incident on a half-space sample. The current density J_y decays exponentially with depth. The skin depth, $\delta(\omega)$, is the $1/e$ decay length. Image courtesy: C. Deans, Department of Physics and Astronomy, UCL - PhD Thesis (2018)

primary field be related to a plane wave incident with a wave vector parallel to the unit vector of the surface of an infinite half-space sample. At a depth y, the current density, is governed by the

$$J(y) = J(0)e^{-y/\delta(\omega)} \tag{4.1}$$

with $J(0)$ the current density at the surface. The skin depth $\delta(\omega)$ is the distance at which the current density has decreased to $J(0)/e$. In radians, the phase lag Φ between the primary field at the surface and the eddy currents density at a depth y is

$$\Phi = \frac{y}{\delta(\omega)} \tag{4.2}$$

The skin depth is [143]

$$\delta(\omega) = \frac{1}{\omega}\left[\frac{\mu\varepsilon}{2}\left(\sqrt{1+\left(\frac{\sigma}{\omega\varepsilon}\right)^2}-1\right)\right]^{-1/2} \tag{4.3}$$

where $\mu = \mu_r\mu_0$ and $\varepsilon = \varepsilon_r\varepsilon_0$ (ε_0 and μ_0 are the permittivity and permeability of free space, respectively). Equation 4.3 is algebraically equivalent to [51]

$$\delta(\omega) = \sqrt{\frac{2}{\omega\mu\sigma}}\left[\sqrt{1+\left(\frac{\omega\varepsilon}{\sigma}\right)^2}+\frac{\omega\varepsilon}{\sigma}\right]^{1/2} \tag{4.4}$$

The operation frequency must be chosen in order to appropriately set the penetration of the primary field.

4.1.1 Asymptotic Limit of the Skin Depth

The asymptotic limit of the skin depth in the high-frequency, low-conductivity regime can be written as

$$\delta(\omega) = \frac{1}{\sigma}\sqrt{\frac{2\varepsilon}{\mu}}\left[\frac{\sqrt{1+x^2}}{x}+1\right]^{1/2} \tag{4.5}$$

where $x = \omega\varepsilon/\sigma$. For conductive samples and low operation frequencies i.e. $\sigma \gg \omega\varepsilon$, the bracketed term of Equation 4.4 approaches unity. The skin depth equation is

$$\delta(\omega) = \sqrt{\frac{2}{\omega\mu\sigma}} \tag{4.6}$$

For metallic samples the reduction holds for frequencies below $10 \times 10^{18} Hz$, while for doped semiconductors the reduction is valid below $10 \times 10^{12} Hz$. This formula is not valid in all regimes, despite being widely quoted as the "skin depth".

4.2 Perturbation due to eddy currents (1)

Now we will face up to the description of the secondary field contribution due to the induction of eddy currents in a real sample, as given by a conductive, thin (thickness h), uniform disk of radius R under the influence of a very small (point like) RF coil placed on the disk axis, at a distance a. We imagine to place our Magnetometer beneath the disk, again on the geometrical axis of

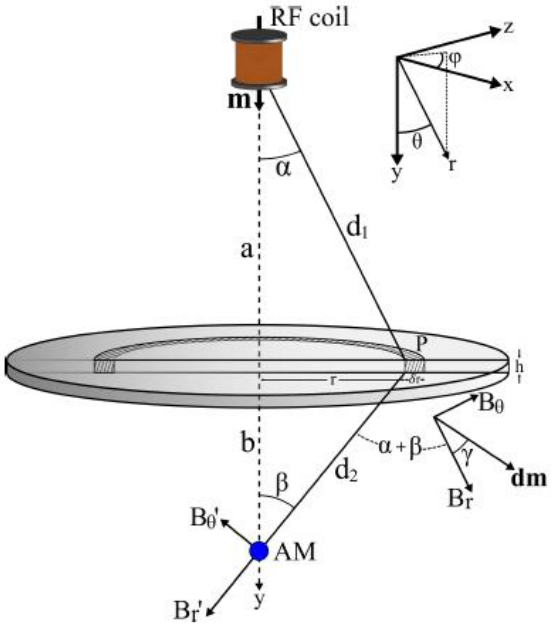

Figure 4.3: EMI configuration with a small RF coil.

symmetry of the setup, at a distance b [41]. We assume that $h \ll a,b,\delta(\omega)$. For the reported calculus, see [41]. Considering the the RF coil as a magnetic dipole m in the y direction, at the point P on the disk, the field is given by

$$B_y = B_r \cos(\alpha) - B_\vartheta \sin(\alpha) = \frac{\mu_0 m}{4\pi}\left(\frac{2a^2 - r^2}{(a^2+r^2)^{5/2}}\right) \tag{4.7}$$

The flux in the loop with radius r is

$$\Phi = \int_S \int B_y dS = 2\pi \int_0^r B_y(r')r'dr' = \frac{\mu_0 m}{2}\frac{r}{(a^2+r^2)^{3/2}} \tag{4.8}$$

so

$$\mathcal{E} = -\frac{d\Phi}{dt} = -i\omega\Phi \tag{4.9}$$

In terms of E_ϕ, we have

$$\mathcal{E} = \int_S \int E_\phi dS = 2\pi \int_0^r E_\phi r'dr' = 2\pi r E_\phi \tag{4.10}$$

and

$$E_\phi = \frac{-i\omega\mu_0 m}{4\pi}\frac{r}{(a^2+r^2)^{3/2}} \tag{4.11}$$

By Ohm's law, the current flowing in an annulus of the disk $[r, r+dr]$ is

$$dI = hdrJ_\phi \tag{4.12}$$

Consider the current uniform throughout the thickness of the disk.
The secondary field contribution of the annulus at the AMs position can be calculated by the Biot-Savart's law

$$dB_2^e = -i\omega\mu_0^2 km\frac{h}{8\pi}\frac{r^3}{(a^2+r^2)^{3/2}(b^2+r^2)^{3/2}} \tag{4.13}$$

$$B_2^e = -i\omega\mu_0^2 km\frac{h}{8\pi}\int_0^R \frac{r^3}{(a^2+r^2)^{3/2}(b^2+r^2)^{3/2}} \tag{4.14}$$

The primary field at the AMs, without the disk, is

$$B_1 = \frac{\mu_0 m}{2\pi(a+b)^3} \tag{4.15}$$

The relationship between the primary field and the eddy current contribution to the secondary field is

$$\frac{B_2^e}{B_1} = -i\omega\mu_0^2 km\frac{h}{8\pi}\int_0^R \frac{r^3}{(a^2+r^2)^{3/2}(b^2+r^2)^{3/2}}dr = A\mu_0\omega\left(\omega\epsilon_0\epsilon_r - i\sigma\right) \tag{4.16}$$

The constant A depends only on the geometry of the system [71]; in the symmetric case ($a = b$) we have, respectively,

$$A = \frac{haR^4}{2(a^2+R^2)^2} \tag{4.17}$$

and for the asymmetric case

$$A = \frac{h(a+b)^3}{2}\left[\frac{ab(ab-(a^2+R^2)^{1/2}(b^2+b^2)^{1/2})+R^2(a^2+b^2)}{(a^2-b^2)^2(a^2+R^2)^{1/2}(b^2+R^2)^{1/2}}\right] \tag{4.18}$$

4.2.1 Perturbation due to permeability (1)

The excitation coil is treated as a magnetic dipole **m** to calculate the field at the point P

$$B_P = |\mathbf{B}| = \frac{\mu_0 m}{4\pi}\frac{(4a^2+r^2)^{1/2}}{d_1^4} \tag{4.19}$$

For a homogeneous medium, the magnetization due to a field B_P is

$$M = \chi_m H = \frac{(\mu_r - 1)}{\mu_0\mu_r}B_P \tag{4.20}$$

where χ_m is the magnetic susceptibility of the medium.
Considering the differential volume element at P, $[r, r+\delta r]\times[\phi, \phi+\delta\phi]$, the magnitude of magnetic dipole induced in this element by B_P is

$$dm_{ind} = MdV = \frac{\mu_r - 1}{\mu_0\mu_r}B_P hrdrd\phi = \frac{\mu_r - 1}{\mu_r}\frac{mh}{4\pi}\frac{r(4a^2+r^2)^{1/2}}{d_1^4} \tag{4.21}$$

The direction of this dipole is displaced by an angle γ from that of B_r.
If d_1 and d_2 are the distances of P from respectively the coil and the AM, from the geometry we can construct the relations

$$\cos(\alpha) = \frac{a}{d_1} \tag{4.22}$$

$$\cos(\beta) = \frac{b}{d_2} \tag{4.23}$$

$$\cos(\gamma) = \frac{B_r}{B_P} = \frac{2a}{(4a^2 + r^2)^{1/2}} \tag{4.24}$$

$$\sin(\alpha) = \frac{r}{d_1} \tag{4.25}$$

$$\sin(\beta) = \frac{r}{d_2} \tag{4.26}$$

$$\sin(\gamma) = \frac{B_\vartheta}{B_P} = \frac{2a}{(4a^2 + r^2)^{1/2}} \tag{4.27}$$

The contribution of each differential dipole element dm_{ind} in the y-direction is

$$dB_2^m = B_r' \cos(\beta) - B_\vartheta' \sin(\beta) = \frac{\mu_0 dm}{4\pi d_2^3}[2\cos(\alpha+\beta+\gamma)\cos(\beta) - \sin(\alpha+\beta+\gamma)\sin(\beta)] \tag{4.28}$$

In the symmetric case, $a = b$, giving, $\alpha = \beta$, $d_1 = d_2$.
For the asymmetric case

$$dB_2^m = \frac{\mu_0 dm_{ind}}{8\pi} \frac{(2a^2 - r^2)(a^2 + r^2)(6a^4 - 27a^2r^2 + 3r^4)}{(4a^2 + r^2)^{1/2}(a^2 + r^2)^3} \tag{4.29}$$

and

$$dB_2^m = \frac{\mu_0 h}{32\pi} \frac{\mu_r - 1}{\mu_r} \frac{2r[4a^4 - 13a^2r^2 + r^4]}{(a^2 + r^2)^5} dr d\phi \tag{4.30}$$

The secondary field due to the magnetization of the disk is given by

$$\begin{aligned} B_2^m &= \frac{\mu_0 h}{32\pi} \frac{(\mu_r - 1)}{\mu_r} \int_0^{2\pi} \int_0^R \frac{2r[4a^4 - 13a^2r^2 + r^4]}{(a^2 + r^2)^5} dr d\phi \\ &= \frac{\mu_0 m h}{32\pi} \frac{(\mu_r - 1)}{\mu_r} \frac{R^2(8a^2 - R^2)}{(a^2 + R^2)^4} \end{aligned} \tag{4.31}$$

For $a = b$

$$B_1 = \frac{\mu_0 m}{16\pi a^3} \tag{4.32}$$

for $a = b$.
The relationship between the primary field and the permeability contribution to the secondary field

$$\frac{B_2^m}{B_1} = B\frac{(\mu_r - 1)}{\mu_r} \tag{4.33}$$

where the constant B depends only on the geometry of the system

$$B = \frac{a^3 h R^2 (8a^2 + R^2)}{2(a^2 + R^2)^4} \tag{4.34}$$

For paramagnetic or diamagnetic samples $\mu_r \approx 1$ so

$$\frac{B_2^m}{B_1} = B(\mu_r - 1) \tag{4.35}$$

4.3 Excitation by Helmholtz's coils

Consider an RF excitation field as applied by a Helmholtz's coil pair of radius R_c.
The AM is positioned at the centre of these coils, where the field is uniform. Again consider a thin, uniform disk of radius R and thickness h positioned centrally, now a distance a above the AM.
As in the previous case, we have an excitation angular frequency ω, a complex conductivity of the disk $k = \sigma + i\omega\varepsilon_0\varepsilon_r$ and a relative permeability of the disk μ_r, and the assumptions: $h \ll a$,R_c and $\delta_r \gg h$. For reference, see again [41].

4.3.1 Perturbation due to eddy currents (2)

The perturbation due to the induction of eddy currents in the disk in the y-direction at the point P, is given by the sum of the contributions from two coils, each found by application of the Biot-Savart's law [148]

$$B_P^y = \frac{\mu_0 N I R_c^2}{2}\left[\frac{1}{(R_c^2 + (a + \frac{R_c}{2})^2)^{3/2}} + \frac{1}{(R_c^2 + (a - \frac{R_c}{2})^2)^{3/2}}\right] \tag{4.36}$$

where I the current and N is the number of turns in each coil.
This field is uniform across the disk,

$$\Phi = B_P^y \int\int dS = \pi r^2 B_P^y \tag{4.37}$$

The relationship between the induced eddy current density and the applied magnetic flux becomes

$$J_\phi = -\frac{i\omega \mathbf{k}}{2\pi r}\Phi = -\frac{i\omega \mathbf{k}}{2\pi r}B_P^y \tag{4.38}$$

The current flowing in an annulus of the disk $[r, r+\delta r]$ (Figure 4.17) is, by following Assumption 2

$$dI = h\delta_r J_\phi \tag{4.39}$$

This contribution calculated by the Biot-Savart's law, is

$$dB_2^e = -i\omega\mu_0 \mathbf{k}\frac{h}{4}\frac{r^3}{(a^2+r^2)^{3/2}}B_P^y dr \tag{4.40}$$

The total eddy current contribution to the secondary field over the entire disk is

$$B_2^e = A\mu_0\omega(\omega\varepsilon_0\varepsilon_r - i\sigma) \tag{4.41}$$

The primary field at the AM (without disk) at the centre point of the coils is given by

$$B_1 = \left(\frac{4}{5}\right)^{3/2}\frac{\mu_0 NI}{R_c} \tag{4.42}$$

This can be seen by taking $a = 0$ in Equation 4.36.
The relationship between the primary field and the eddy current contribution to the secondary field is found by combining Equations 4.41 and 4.42

$$\frac{B_2^e}{B_1} = A\mu_0\omega(\omega\varepsilon_0\varepsilon_r - i\sigma) \tag{4.43}$$

where

$$A = \frac{B_P^y}{B_1}\frac{h}{4}\left[\frac{2a^2+R^2}{(a^2+R^2)^{1/2}} - 2a\right] \tag{4.44}$$

The constant A depends only on the geometry of the system.
In the case where a is small, the Helmholtz current field $B_P^y \approx B_1$ is uniform

$$A = \left(\frac{5}{4}\right)^{3/2}\frac{hR_c^3}{8}\left[\frac{2a^2+R^2}{(a^2R_2)^{1/2}} - 2a\right]\left[\frac{1}{(R_c^2\left(a+\frac{R_c}{2}\right)^2)^{3/2}} + \frac{1}{\left(R_c^2+(a-\frac{R_c}{2})^2\right)^{3/2}}\right] \tag{4.45}$$

4.3.2 Perturbation due to permeability (2)

Finally, the permeability component of the secondary field is derived from the Helmholtz's imaging configuration.

Recall that the field at the point P in the y direction is defined as B_P^y. Considering the differential volume element, $[r, r+\delta r] \times [\phi, \phi+\delta\phi] \times [0, h]$, at P the magnetic of the magnetic dipole induced in this element can be shown to be

$$dm = \frac{(\mu_r - 1)}{\mu_0 \mu_r} B_P^y h r dr d\phi \tag{4.46}$$

The secondary field contribution of this dipole dm at the AM in the y direction is given by

$$dB_2^m = \frac{h}{4\pi} \frac{(\mu_r - 1)}{m u_0 \mu_r} B_P^y \left[\frac{r2a^2 - r^2}{(a^2 + r^2)^{\frac{5}{2}}} \right] dr d\phi \tag{4.47}$$

The total permeability contribution to the secondary field is found by integrating over the volume of the disk

$$B_2^m = \frac{h}{4\pi} \frac{(\mu_r - 1)}{\mu_0 \mu_r} B_P^y \int\int \left[\frac{r2a^2 - r^2}{(a^2 + r^2)^{5/2}} \right] dr d\phi \tag{4.48}$$

Recalling the primary field B_1 in the absence of the disk, the relationship between the primary field and the secondary field contribution is given by

$$\frac{B_2^m}{B_1} = B(\mu_r - 1) \tag{4.49}$$

We assumed that the material is paramagnetic or diamagnetic and defined the constant B as

$$B = \frac{B_P^y}{B_1} \frac{h}{2} \left[\frac{R^2}{(a^2 + R^2)^{3/2}} \right] \tag{4.50}$$

If a is small, $B_P^y \approx B_1$

$$B = \left(\frac{5}{4}\right)^{3/2} \frac{h R_C^3}{4} \left[\frac{R^2}{(a^2 + R^2)^{3/2}} \right] \left[\frac{1}{\left(R_c^2 + \left(a + \frac{R_c}{2} \right)^2 \right)^{3/2}} + \frac{1}{\left(R_c^2 + \left(a - \frac{R_c}{2} \right)^2 \right)^{3/2}} \right] \tag{4.51}$$

For a sample of conductivity σ, relative permittivity ε_r, relative permeability μ_r, and an excitation field frequency ω the relationship between B_1 and B_2 was shown to be

$$\frac{B_2}{B_1} = A\omega\mu_0[\omega\mu_0(\varepsilon_r - 1) - i\sigma] + B(\mu_r - 1) \tag{4.52}$$

where A and B are constants that depend on the geometry of the system. The modification $\varepsilon_r \to (\varepsilon_r - 1)$ has been included.

Without this transformation, in the absence of a sample ($\sigma = 0, \varepsilon_r = 1, \mu_r = 1$) the secondary field includes a contribution from the displacement currents in the air.
The transformation removes this background contribution, shifting it from B_2 to B_1. This ensures that the condition B_2/B_1 holds with no sample present.
The first term on the RHS of Equation 4.52 is due to the induction of eddy currents in the sample (B_2^e).
Whereas the second term arises from the magnetisation of the sample (B_2^m).
The following general observations about the response in EMI can be made:
1 - Changes in the real part of the secondary field are related to changes in the relative permittivity (displacement current density) and relative permeability (magnetization) of the sample.
2 - Changes in the imaginary part of the secondary field are related to changes in the conductivity of the sample (eddy current density).
3 - The presence of an imaginary component results in a phase-lag, F, of the total field with respect to the primary field. A phase sensitive detection scheme is therefore required to correctly characterize the response.
4 - The contribution of B_2^e increases with increasing excitation frequency.
5 - The contribution of B_2^m is not dependent on the excitation frequency. Therefore, it can often be isolated or removed.
It is important to note that point 4 conflicts with Equation 4.6, which states that the penetration distance decreases with ω. The choice of operation frequency therefore determines both the size of the EMI response and the depth at which the sample's properties are probed. This trade off must be carefully examined in view of each desired application

4.4 Copper and Aluminum samples

For conductive samples, in our case Cu and Al, the conductivity of the sample generates an imaginary contribution to the secondary field, leading to a phase-lag.
The permittivity and permeability contributions can be neglected as $\{\varepsilon_r, \varepsilon_r\} \approx 1$.
In practical applications, the operation frequency often dictates that the skin depth is comparable or smaller than the thickness of the object.

In this case Equation 4.52 is no longer valid.
The sample can partially attenuate the primary field which manifests as a negative contribution to the real part of the secondary field.
This effect increases the measured Φ and decreases B_{tot}. At low frequencies, the primary field fully penetrates the sample, and we find the ideal response of Figure 4.4. Only the conductivity component contributes to the signal.

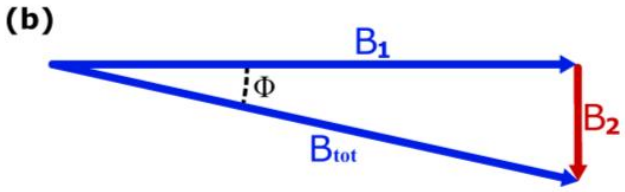

Figure 4.4: Argand's diagram for a conductive sample. Conductive sample where the skin depth is much greater than its thickness. Image courtesy: C. Deans, Department of Physics and Astronomy, UCL - PhD Thesis (2018)

By measuring this value we extracted by Y i.e. the change in the imaginary component of B_{tot} or measuring $\Phi = \arctan(B_2/B_1)$.
For Cu and Al samples the skin depth is comparable to the sample thickness. In contrast, as the conductivity of the sample is lowered one moves towards the regime depicted.

Chapter 5

Experimental Setup

5.1 Introduction

In this Chapter each development of the EMI-AM experimental setup are described. The ability to detect objects concealed underground, underwater or in cargo containers is a key requirement in many surveillance and security applications.

Despite the number of techniques already available, continuously changing scenarios creates a growing demand for new approaches to be developed. In this context, Renzoni's Group at UCL proposed a remote, non invasive detector for conductive objects, based on Optical Atomic Magnetometers (OAMs) operating in the Magnetic Induction Tomography (MIT) modality. It was precisely Renzoni's group that provided us the data sets processed in this Thesis work.

MIT relies on the excitation of eddy currents in the object of interest and on the detection of the magnetic fields produced by them, in order to investigate the electrical and magnetic properties of an object of interest. It was successfully exploited in a large number of non-invasive testing and probing applications including, for example, the investigation of structural integrity in constructions, quality control in industrial processes, and fatigue-induced damage detection.

Recently, the first conventional approach of an MIT system to screening and security was reported, demonstrating the penetration of thick and multi-layered enclosures. However, these systems are limited by the poor sensitivity of pick-up coils at low frequencies, which also limits their maximum range and their response to unexpected operational conditions or targets.

OAMs overcome these limitations: their sensitivity is comparable or even better than state of the art magnetic sensors, and their bandwidth is not limited by intrinsic factors. In addition, OAMs have an enormous potential for miniaturisation, and they do not require calibration, because their output is proportional to the magnetic field through fundamental physical constants only.
Optical atomic magnetometers in magnetic induction configuration therefore provide a path to a new generation of non invasive, remote, active detectors for surveillance and security applications.
Renzoni's group embedded a modular system, in view of different array arrangements, of optically pumped optical atomic magnetometers (OP-OAMs) operating in the MIT modality. An analogous system could in principle be implemented with different kinds of OAMs, but the OP-OAMs allow a reduction of the system's complexity, and therefore of its costs and footprint. The design features the separation of sensor from the electronics and light-generation. The vapor cell is positioned on a marble table supported by a wooden frame.

5.2 Sensor Apparatus

A schematic sketch of the unshielded RF-AM setup is shown in 5.1. The

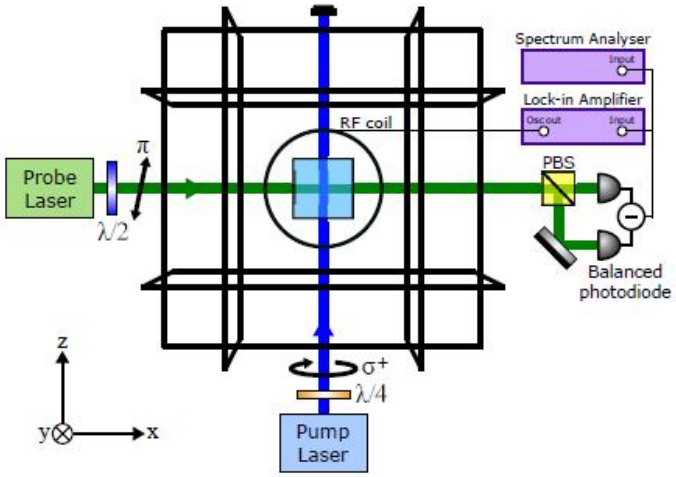

Figure 5.1: Schematic of the general unshielded RF-AM. Image courtesy: C. Deans, Department of Physics and Astronomy, UCL - PhD Thesis (2018)

sensor core is a cell filled with a spin-polarised atomic vapor. The circularly polarisation is obtained by a pump beam and a parallel DC magnetic field, i.e. the bias field B_{BIAS}.
The direction of the pump beam is defined as the z direction. Before the cell, by a quarter wave plate $\lambda/4$, the polarisation σ^+ in provided. The bias field is controlled by a series of Helmholtz coils.
The magnitude of this field sets the operation which the operation frequency can be tuned in view of the desired application.
The magnetometer is y-direction calibrated by a AC magnetic field B_{RF} which excites spin coherences between nearest-neighbour ground state Zeeman's sub levels.
The atomic precession is read out in the cell by the rotation of the plane of polarisation of a linearly polarised probe beam which crossed perpendicular to the pump beam.
By perpendicular arrangement, it is obtained a fine control in the sensing region, which allows a balance between the signal and the spatial resolution of the measurements.
In order to avoid alteration of the atomic polarisation, the probe beam is blue detuned. A half wave plate $\lambda/2$ set the linear polarisation of probe beam in x-direction before the cell.
The polarimeter detects the probe beam polarisation rotation. The output of the photodiode is interrogated by a lock-in amplifier (LIA) and a spectrum analyser.
The LIA extracts four set of data: the in-phase X (absorptive) and out-of-phase Y (dispersive) components of the polarimeter single along with the signal intensity modulus $R \equiv X^2 + Y^2$ and phase ($\Phi \equiv \arctan Y/X$).

5.2.1 Vapor cell

The cubic quartz cell dimensions are $25mm \times 25mm \times 25mm$. The cell contained Rb a natural mixture of ^{85}Rb and ^{87}Rb, or isotopically enriched ^{87}Rb vapour. Furthermore, a ^2N a buffer gas $20Torr$ is added. No anti-relaxation wall coatings are used. Optical windows on four sides arranged in two orthogonal pairs allow access for both beam.

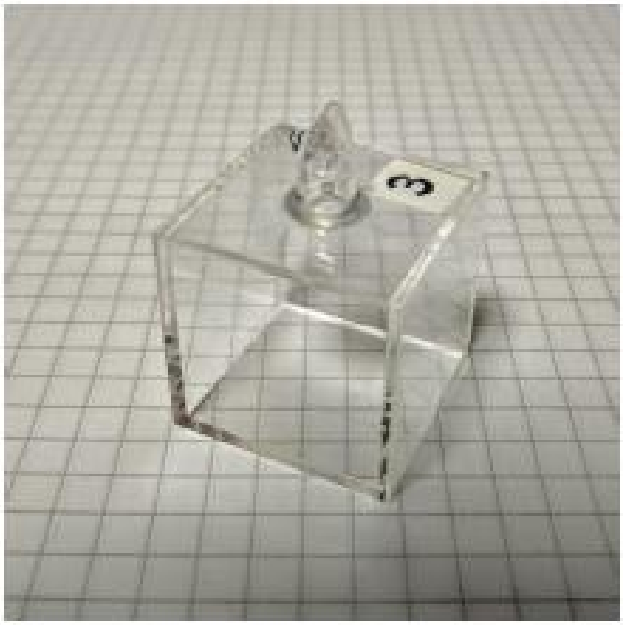

Figure 5.2: Vapor cell. Image courtesy: C. Deans, Department of Physics and Astronomy, UCL - PhD Thesis (2018).

5.2.2 Lasers

The lasers emit on either the D1 or D2 lines for Rb at $795nm$ and $780nm$, respectively; they can be locked to the desired transitions by means of Doppler free dichroic atomic vapor laser lock (DAVLL) or peak locked via frequency modulated saturated absorption spectroscopy.

5.2.3 Measurement method

A general schematic showing the principles of EMI with an RF-AM is provided in Figure 5.3. An excitation coil provides the primary magnetic field B_{RF} oscillating at ω_{RF} in the y direction.
This field excited an eddy current response by the incidence on the sample. The skin effect caused the exponential decays of the eddy currents density along y-direction. A secondary magnetic field B_{EC}, opposing the primary one, is produced by eddy currents and the secondary field perturbation introduces a phase lag (F) between the the total field B_{tot} and B_{RF}. The field B_{tot}, which contains information on the sample's conductivity σ, relative permittivity ε_r, relative permeability μ_r, and its geometry, was detected

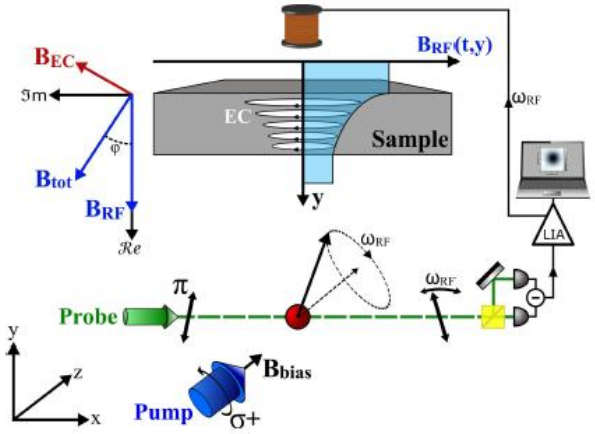

Figure 5.3: AM-based EMI imaging system. Image courtesy: C. Deans, Department of Physics and Astronomy, UCL - PhD Thesis (2018).

by RF-AM. In this way, the characteristics of the sample are imprinted into the precessing motion of the atomic spins. This is passed to the polarisation rotation properties of the probe beam before being extracted by the detection scheme.

By measuring B_{tot} at various positions non-invasive, contactless 2D maps of the sample properties are constructed. These scans are performed by moving the sample relative to the excitation coil exciting ECs in a different location for each measurement.

An x, y stage provides the translational motion for the imaging.

Computer control of the stage motion and measurement system allows the images to be constructed in real time by the laptop.

ECs produce a secondary field perturbation B_{EC} opposing B_{RF} and phase-lagged (by an angle Φ) with respect to it.

5.3 Overview of UCL EMI system

The EMI-AM systems experiment can be split into three major iterations. We will concentrate on the first step of this setup evolution, as the data we have analyzed are related to it.

5.4 EMI-AM I

5.4.1 Optical setup

A sketch of the optical setup is shown in Figure 5.4.
A single laser source is tuned to either the D2 line $F = 2 \rightarrow, F' = 3$ hyperfine transition of ^{87}Rb or to the D2 line $F = 3 \rightarrow, F' = 4$ hyperfine transition of ^{85}Rb.
The beam is then split into two arms, the pump beam and the probe beam. The pump beam has a power of approximately $1mW$ with a beam waist of

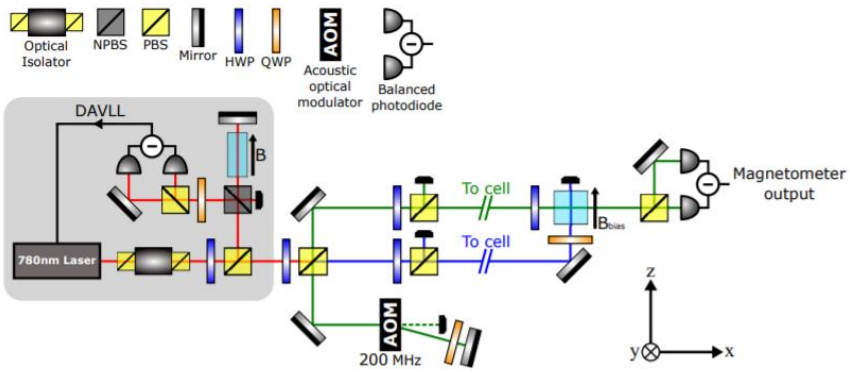

Figure 5.4: In the vapour cell, pump beam (blue) and probe beam (green) cross orthogonally. Beams provided by a single 780nm laser. The gray region represents the dichroic atomic vapour laser lock (DAVLL). HWP is half-wave plate ($\lambda/2$), QWP is a quarterwave plate ($\lambda/4$), NPBS is the non-polarising beam-splitter and PBS is polarising beam-splitter. Image courtesy: C. Deans, Department of Physics and Astronomy, UCL - PhD Thesis (2018).

around $4mm$.
Assuming a uniform distribution, the intensity is therefore $7.9mWcm^{-2}$. This is equivalent to $4.6I_s$, where I_s is the saturation intensity for the pumping transition [139].
The probe beam is blue detuned via a double pass acoustic optical modulator (AOM), with a total detuning of $400MHz$. The probe beam waist is $2.5mm$ with a power of $25\mu W$ equivalent to an intensity of $0.52mWcm^{-2}$.

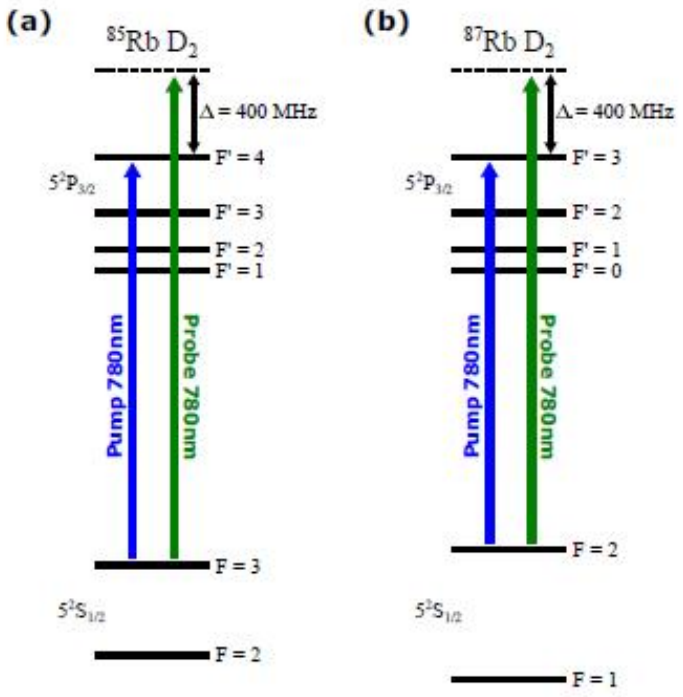

Figure 5.5: EMI-AM I level diagram. Image courtesy: C. Deans, Department of Physics and Astronomy, UCL - PhD Thesis (2018).

5.5 EMI-AM II

5.5.1 Sensor design

A scale model of the sensor unit is shown in following Figures. The bias magnetic field is provided by a pair of Helmholtz coils of diameter $80mm$. The AC magnetic field is supplied by a single small ferrite-core coil (diameter=$7.8mm$, L=$680\mu H$ at $1kHz$) centred on the cell, $63mm$ above the beams. This field both drives atomic precession (when calibrating the sensor) and acts as the EMI primary field. The pump and probe beams were split further to create four such sensors. A number of limitations in the system design are removed. Examples include the basic bias field control limiting the sensitivity and tunability. The EMI-AM II system represents the second iteration of the imaging platform. The modifications and upgrades, which improved the sensing and imaging performance, are described in this section. The EMI-AM II system was used for the results reported in References [43], [107], [46].

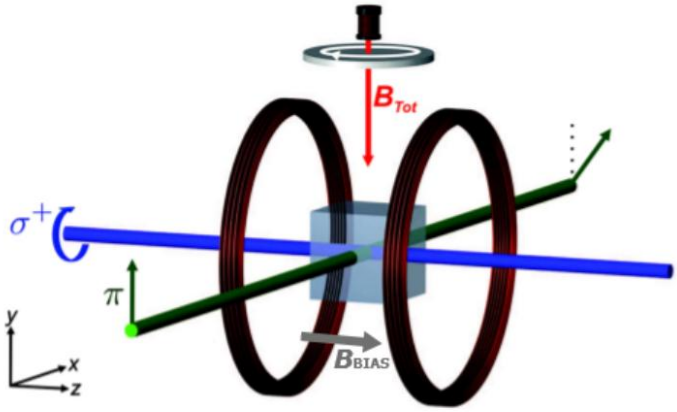

Figure 5.6: EMI-AM I sensor. Image courtesy: C. Deans, Department of Physics and Astronomy (UCL) - PhD Thesis (2018).

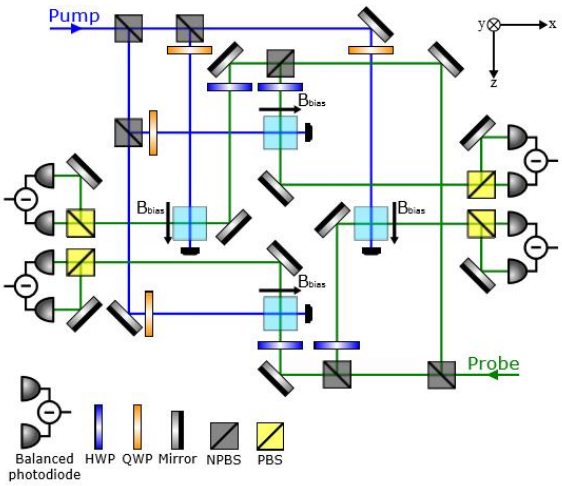

Figure 5.7: EMI-AM I array optical setup: The four sensors operated simultaneously. Cells positioned at the corners of a 105 ×105mm square. HWP: half-wave plate ($\lambda/2$). QWP: quarter-wave plate ($\lambda/4$). NPBS: non-polarising beam-splitter. PBS: polarising beamsplitter. Image courtesy: C. Deans, Department of Physics and Astronomy, UCL. PhD Thesis (2018).

5.5.2 Sensor arrangement

The initial optical arrangement of the system was unchanged although rearranged from the previous design. The beam profiles were modified and additional control on the beam powers added. This is obtained by controlling the modulation depth of the AOM, thus changing the amount of light conveyed to the diffracted order in use. It is possible by exploiting the amplitude modulation of the AOM driver.
This resulted in a pump beam with waist 5mm and an intensity controlled up to a maximum of $214 mW cm^{-2}$.
The probe beam waist is 3mm and its intensity can be controlled up to $18.6 mW cm^{-2}$.
Note that the saturation intensities for the pumping and probing transitions are $1.6 mW cm^{-2}$ and $2.5 mW cm^{-2}$, respectively [139] (1), [139] (2), [85].
The EMI-AM II design is dominated by the active magnetic field compensation system.
The DC magnetic field at the position of the sensor is given by the Earth's magnetic field plus perturbations from other sources. Therefore, it is unlikely that the bias field will be aligned parallel to the pump beam. This means that the field in each axis must be controlled to ensure that the quantisation axis is correctly aligned along the z direction.
The background magnetic field at vapor cell's position is [$171 mG$,$323 mG$,$63 mG$] in the x,y,z basis. Recall that: the pump beam propagates along z, the probe beam along x, and the RF field is applied along y.
For an operation frequency of $400 kHz$ this is equivalent to a misalignment of the quantisation axis by $25.4 - 39.8$ grades from the desired direction for ^{87}Rb and (^{85}Rb), severely limiting the optical pumping efficiency. To account for this, the sensor is surrounded by a $1.3m$ 3-axes square Helmholtz's coil system. This allows compensation of the Earth's magnetic field along all three axes.
The $1.3m$ side length maximizes the region of magnetic homogeneity across the cell. Along z an additional $40cm$ diameter circular Helmholtz's coil (OP_z) provides the bias field for highfield operation. A $1.2m$ square anti-Helmholtz's coil along z further increases the bias field homogeneity by allowing gradient compensation. The RF calibration field is generated by a further Helmholtz's coil pair of diameter $18cm$ (RF_y). This arrangement provides a uniform field across the cell.

For imaging, the 7.8mm ferrite core coil provides the primary field. Eddy currents from conductive elements near the sensor introduce further noise. This effect is reduced by constructing the sensor support and Helmholtz coils from 3D printed PLA components.
The coil cage alone comprises of 200 custom-made pieces. The vapor cell is lifted 650mm above the top of the optical table to further reduce the proximity of metallic components.

5.5.3 Active compensation system

For many practical applications, operation in unshielded environments is required. In this case, magnetic field noise is the major limitation to the sensor performance.
The response of the atomic sample is susceptible to changes in the background magnetic field and to oscillating magnetic field noise. The dominant source of this noise is 50Hz noise arising from mains power lines. For EMI applications these need to be strongly suppressed. This is because a stable magnetometer response is required to reliably image samples. AMs operating in a gradiometric configuration offer an alternative approach to compensating magnetic field noise in unshielded environments [35], [91], [17], [16]. Such approaches can either subtract the signal from two (or more) separate magnetometers cancelling the common noise, or take advantage of the AMs sensitivity to implement the feedback to the coil current. However, gradiometer arrangements are only suitable for measuring local, rapidly decaying fields. Therefore, in the context of EMI, operation with a gradiometer configuration is complicated and yet to be demonstrated. This is because any approach must be capable of decoupling (and suppressing) the magnetic field noise from the perturbations due to the sample that one aims to detect.

5.5.4 Temperature stabilisation

The vapor cell is heated due to the fact that the sensitivity scales with the atomic vapor density as $1/\sqrt{N}$. A thin copper wire (0.22mm diameter) provided the heating.
For EMI, long-term signal stability is required to accurately determine features of the images. The cell temperature is stabilised by switching off a heater once the temperature reaches a controllable set-point. Additionally,

the enabled pin allows the heater to be momentarily paused whilst the atomic precession is probed, completely removing the possibility of any stray magnetic fields affecting the measurements. The system is able to maintain the vapor cell temperature to within $0.1C$.

5.5.5 D1 line optical pumping

An upgrade to the EMI-AM II system included the addition of a second laser emitting at $795nm$ resonant with the Rb D1 line. This laser provided the pump beam in the updated optical setup (Figure 5.8). Pump beam (blue) provided by a D1 line laser at $795nm$. Probe beam (green) provided by a D2 line laser at $780nm$. DAVLL: dichroic atomic vapour laser lock (grey region). HWP: half-wave plate ($\lambda/2$). QWP: quarterwave plate ($\lambda/4$). NPBS: non-polarising beam-splitter. PBS: polarising beam-splitter. This upgrade

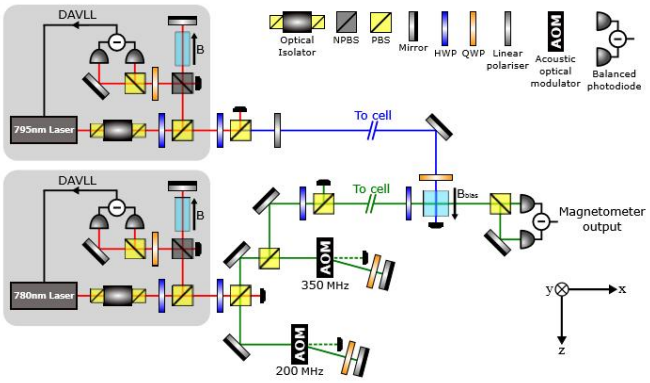

Figure 5.8: EMI-AM II D1 line optical setup. - Image courtesy: C. Deans, Department of Physics and Astronomy, UCL - PhD Thesis (2018).

coincided with an additional double pass $350Mhz$ AOM being included in the probe beam path.

This brings the total blue detuning of the probe to 1.1GHz from the D2 line reference transition, see 5.9. The optical pumping excites most of the atomic population of the sample on the same higher level respect to ground state. After the excitation, the collisional mixing due to thermal agitation destroys the coherence and causes the atoms to decay back to the ground level. The time interval of permanence on the pumped state of row D1 is greater than that of row D2, therefore in the first case performing measurements is

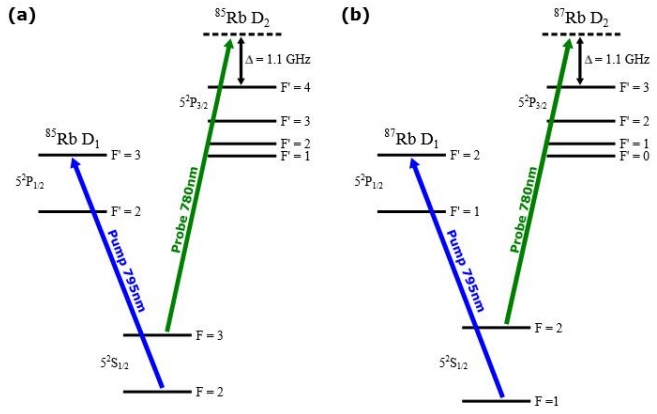

Figure 5.9: EMI-AM II D1 line level diagram: (a) 85^Rb. Pump tuned to the D1 line $F = 2 \rightarrow F' = 3$ transition. Probe blue-detuned by $1.1GHz$ from the D2 line $F = 3 \rightarrow F' = 4$. (b) 87^Rb. Pump tuned to the D1 line $F = 1 \rightarrow F' = 2$ transition. Probe blue-detuned by 1.1 GHz from the D2 line $F = 2 \rightarrow F' = 3$ - Image courtesy: C.Deans, Department of Physics and Astronomy, UCL - PhD Thesis (2018).

favourable.

5.5.6 Magnetic field and gradient suppression

An upgraded Helmholtz's coil system is used to impose the desired bias field, cancel stray magnetic fields, and actively compensate for changes in these fields and oscillating magnetic field noise. In this design anti-Helmholtz's coils are included on all axes to suppress magnetic field gradients. The dimensions of each coil range from $1.3m$ to $1.41m$.

The increased number of turns available in the z direction unlocks higher operation frequencies. Under application of the typical maximum currents the operation frequency is predicted to be around $9.5MHz$. This is achieved despite the removal of the $40cm$ diameter OP_z coil.

The magnetic field homogeneity across the cell is increased with all coils being greater than $1.3m$ and the inclusion of gradient compensation along x and y.

During operation, a fixed DC current is applied to z_1 and-or z_2 to impose the majority of the bias field. The current in z_Δ is then regulated by the PID feedback to lock the field to the desired set-point.

The fields from the traverse compensation coils (x and y) can also be locked

to fix $B_x = B_y = 0$. When not locking these fields, the currents in these coils can be automatically calibrated and set by the control software which takes advantage of the magnetometer response. Further software enables the automatic optimisation of the anti-Helmholtz coils for gradient suppression.

5.6 Performance limitations

The dominant limitation is the reduction of the optical pumping due to the lack of background field cancellation in the transverse directions. In addition, other factors which affect the performance of system are: the homogeneity of the bias field, the magnetic noise, the ability to cycle through the experimental parameter space to optimise performance, the limited efficiency of optical pumping on the D2 line and the control over the cell temperature.

5.7 EMI-AM II performance

In order to remove these limitations, was designed a second-generation EMI-AM II system which achieve a final measured sensitivity of $130 fT/\sqrt{Hz}$ and a HWHM of $104 Hz$. The optimisation requires finding the optimum set of

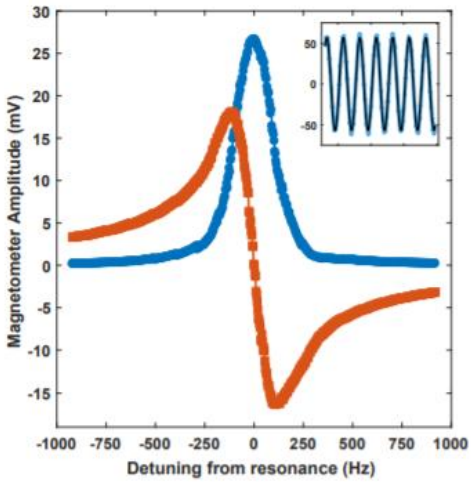

Figure 5.10: Typical profile of the RF-AM response at $100 kHz$ - Image courtesy: C. Deans, Department of Physics and Astronomy, UCL - PhD Thesis (2018).

meter space, so it is necessary to record the effect of each parameter on the

magnetometer response: X, the signal amplitude, the linewidth ($\Gamma/2$) and Y, the gradient, are recorded from the LIA response. Further information is gained by examining the signal amplitude and SNR, along with the contributing factors limiting the noise from the SA. The parameters of interest are the strength of the applied RF field. The operation frequency for optimisation was nominally chosen to be $100kHz$. In the vapour cell was contained an isotopic mixture of ^{85}Rb and ^{87}Rb, at 20 Torr pression and ^{2}N as buffer gas. The pump beam acts on the D1 line of ^{85}Rb and a vapor cell temperature of $45°C$.

Chapter 6

Imaging and Data Analysis

Imaging techniques are a valuable resource in many fields of research, but difficulties in image reconstruction can narrow the field of applications.
This Thesis work presents an alternative approach to imaging based on an Optically Pumped Radio Frequency Atomic Magnetometers (RF-OAM) system, which allows us to combine the advantages of OAMs in terms of sensitivity, with the simplicity, robustness and scalability of this special kind of magnetometers.
In particular, we report on the results obtained by applying imaging techniques to metal objects in an unshielded environment.
The main problem consisted in identifying the edge of the objects, three metal samples whose dimensions were of the order of centimeters. The intent was to create an analysis method that had such a general character as to make it applicable to different physical samples.
This goal has been fully achieved through the elaboration of an algorithm based on the evaluation of simple statistical parameters, so the generality of the procedure is guaranteed. The material of which the samples are made, their geometry and dimensions, are not diriment.
To study the noise we started from the simple assumption that we are in the presence of a Gaussian distribution. The symmetry properties of the Gaussian allowed us to identify the shapes of the objects of study, compatibly with the experimental limits related to the instrumentation.
In addition, all imaging techniques also proceed through significant modifications of the initial data, but in this case it was possible to avoid it: we intervened on the initial data without having had the need for any manipulation.

As will be highlighted in the following paragraphs of this chapter, one of the strengths of the method consists in its reproducibility in future experiments.

6.1 Imaging techniques

During the last few years it has been proved that Atomic Magnetometers represent a valid alternative to traditional imaging techniques.
In the previous Chapters, we discussed the features which make of Electromagnetic induction imaging a non-invasive method to investigate the conductivity or permittivity properties of a medium: they are safer and healthier than X-ray systems, as do not use ionizing radiation; they down scale in magnetic fields for 9 orders of magnitudes, operating at nanoTesla instead of Tesla values, typical of Nuclear Magnetic Resonance (NMR), and allow for the construction of portable sensors/detectors.
OAM have better sensibility and tunability than the non optical magnetometers, they work around room temperature without high costs of maintenance and in addition they do not need metal shielding.
OAM have been used for imaging techniques, but the image reconstruction and the object pattern recognition lacks in terms of quality. In fact, the effect of scattering of electromagnetic signals at low-frequency provides blurred images and does not allow for a clean ray-optics response.
Several methods of edge detection based on changes in brightness or discontinuities in depth, have been developed. These techniques manipulate the original image data causing a loss of information and the derivative-based methods do not provide good performances in the presence of very noisy signals. In fact, any additional smoothing procedure change the original data.

6.2 Electromagnetic induction images.

The object of this Thesis is the elaboration of some data sets we have been kindly provided by Renzoni's group (Dept of Physics and Astronomy-Faculty of Maths and Physical Sciences - UCL).
As we have illustrated in the previous chapters, the experiment concerns the detection of any anomalies in samples of different materials, using regular shapes with simplified geometries.
The UCL magnetometer is all optical and operates in an unshielded, mag-

netically polluted environment, in such a way that the noise sources, as the primary coil size, do not allow for a precise determination of the border of the samples.
By appropriately adjusting the excitation frequency, similar levels of signal change are recorded, despite the large differences in conductivity.
The following figures represent some results obtained by colleagues at UCL.

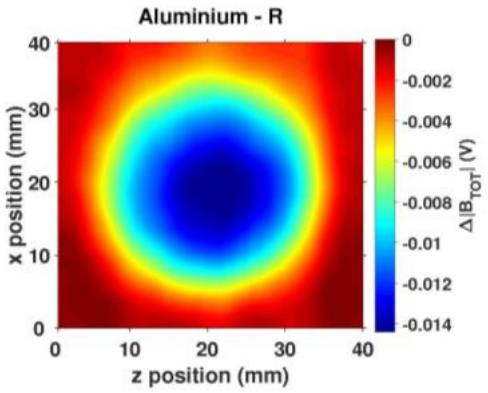

Figure 6.1: The two-dimensional map of the set R relative to the 50mm aluminum square is shown. The image presents problems in the precise identification of the edges but the figure, without edges, is represented with a good approximation. Image courtesy: C. Deans, Department of Physics and Astronomy, UCL - PhD Thesis (2018).

These are two-dimensional maps in which it is possible to identify blue objects on a red background. Moving away towards the outlines, i.e. on the edges of the samples, the colors degrade to a yellow scale. Each image of these represents a different property of the secondary field and can be associated to different electromagnetic properties of the sample. In addition, images reproduce the size and shape of the sample.
The "rounding-off" of corners is attributed to the limited flow of eddy currents in those regions.
As eddy current flows are circular their density is reduced in areas containing sharp angles. The results include examples from the initial EMI-AM I experiment and throughout the development of the EMI-AM II system.
For completeness of information, the results include RF-AMs operating with different isotopes of Rb, and results using both D1 and D2 line optical pumping.
It is important to note that the latest imaging of low-conductivity samples

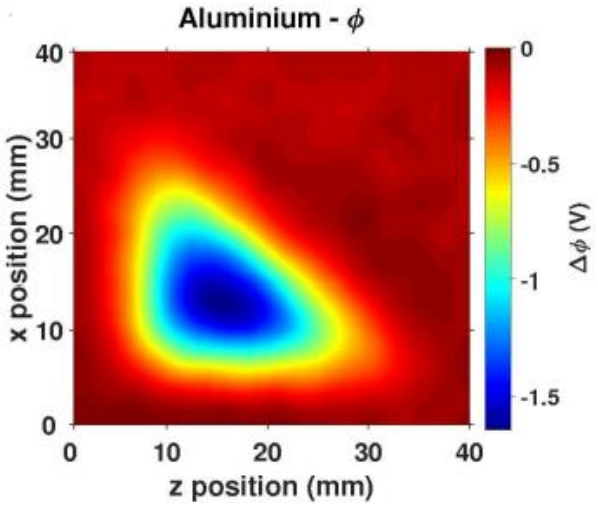

Figure 6.2: Two-dimensional map of set P relative to the 50mm aluminum square is shown. The image presents considerable problems in identifying both the shape and the size. The elaborations performed refer to the sets, which contain all the information relating to the magnetic field induced by the eddy currents. Image courtesy: C. Deans, Department of Physics and Astronomy, UCL - PhD Thesis (2018).

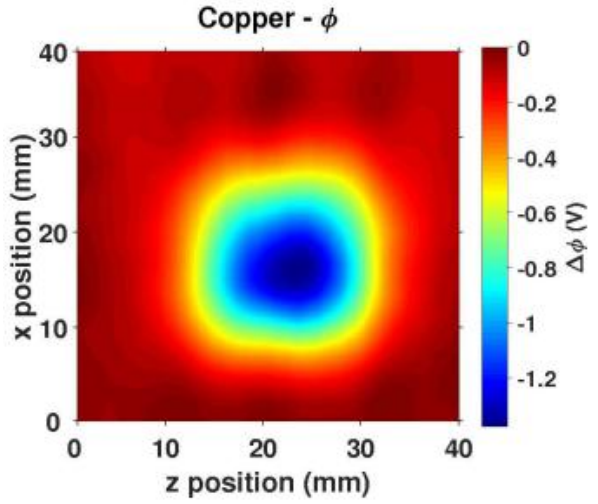

Figure 6.3: Two-dimensional map of set P relative to the 30mm copper disk is shown. The image presents considerable problems in identifying both the shape and the size. In particular, the edges appear to have a low level of definition. Image courtesy: C. Deans, Department of Physics and Astronomy, UCL - PhD Thesis (2018).

is only possible due to the improvements in sensitivity, stability, and range of tunability of the sensor. The increased signal stability of the EMI-AM results in a reduction in the background noise, so the image outline is more clear.
The suitable experimental control software has been developed and improved in parallel to the system. The X, Y, and R channels are the signal in mV and Φ in degrees.

6.3 Processing of data

The ambitious goal of this analysis, which represents a step forward respect the UCL research, is the possible application of this method to a large variety of samples and contexts, included the biological field. In fact, for example, investigating bulk spatial inhomogeneities in the complex dielectric constant which characterizes the various tissues, makes it possible to discriminate between various pathological states.
On the other hand, our focus is the development of an operational strategy which would allow us to treat different materials without having to worry about their particular type. In practice we wanted to implement a script whose functionality was absolutely independent of the object examined.
We have elaborated a $MatLab$ program with the purpose of operating a filtering process, in order to perform an accurate elaboration of each data set, trying to better define the borders of the objects. It is useless to say that some trials have still to be approached while others are actually in progress. We will report on some preliminary results and some recently planned strategies which represent imaging performance.
The geometry of the samples is a crucial parameter that requires discussion. In summary, as already declared, all the samples have the same order of magnitude for their sizes and thicknesses, that is approximately the same as that of the coil detector: for further reference, the largest sample volume is $12.5cm^3$, for the lowest conductivity samples the volume is $6.25cm^3$. This allows for a detailed high-resolution EMI performance of the sample's features. In the following, we will show our reconstruction in a 3D view of these samples, picturing along the plane the real coordinates, while on the third axis the magnetic field intensity values introducing false colors.

6.3.1 Statistical processing data

Our work can be divided into two distinct phases. In the first place, we have represented and organized the data that express the values of the total magnetic field in correspondence with each of the scanning groups. In fact, it was immediately evident that the images obtained with standard graphic techniques, had a low resolution; in particular it was easy to identify the metal samples but the edges of the objects were very blurry.
Defining the geometry of samples turned out to be a particularly critical operation in the case of the aluminum square due to the presence of edges. It was necessary to follow a different approach in order to achieve a better definition of the edges of the objects. These procedures can also be easily reiterated through the possible assumption and processing of the most substantial data sets. In the following Figures, 3D plot of the 2D data was represented.
For each sample, i.e. for the two copper disks and the aluminum square, we had four sub sets: X, Y, R and P, but we worked on the R set as it contained all the information relating to the numerical variations of the magnetic field. Finally, a fitting process was performed in order to reconstruct an image of the samples, interpolating the points found on the contour. The results obtained are presented, point by point, in the following paragraphs with the addition of an interesting case study on the fracture present in a metal ring. In the following Figures, we show the organization of the data that came to us in the form of 70×70 matrices, representing the noise.

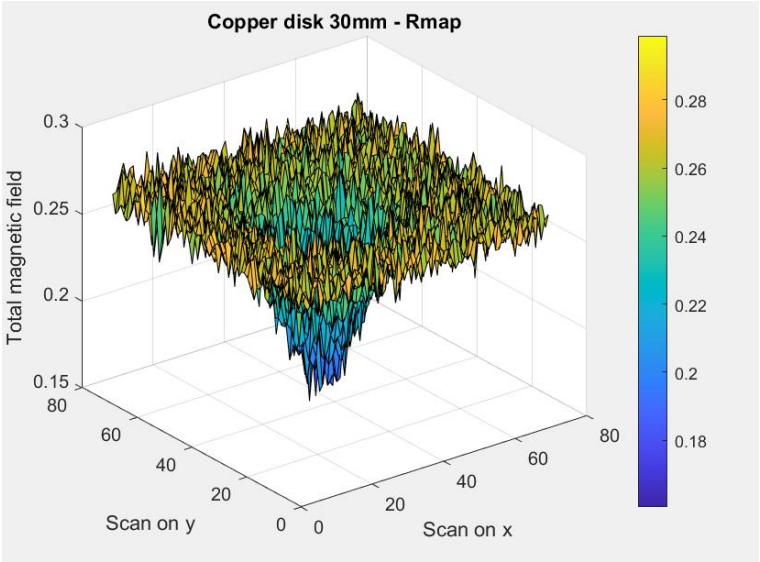

Figure 6.4: Copper Disk 30 mm - Set R. Three-dimensional noise representation.

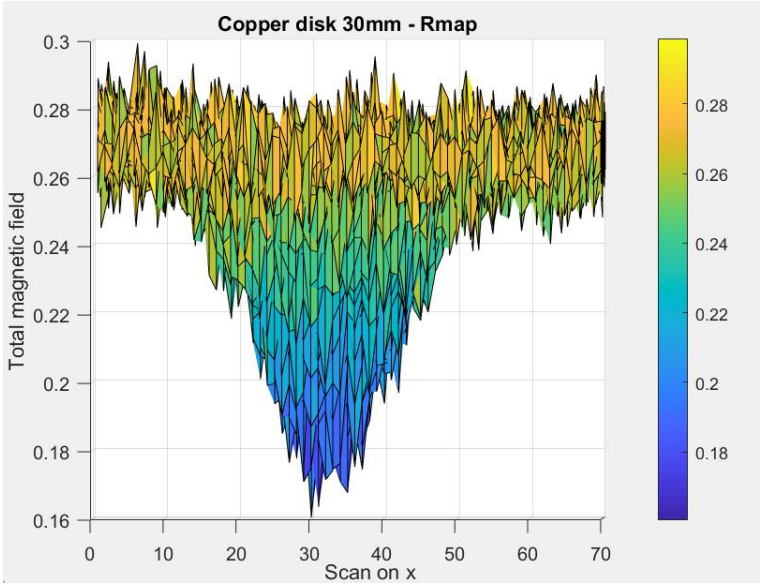

Figure 6.5: Copper Disk 30 mm - Set R. Two-dimensional noise representation observed in a plane of a fixed y.

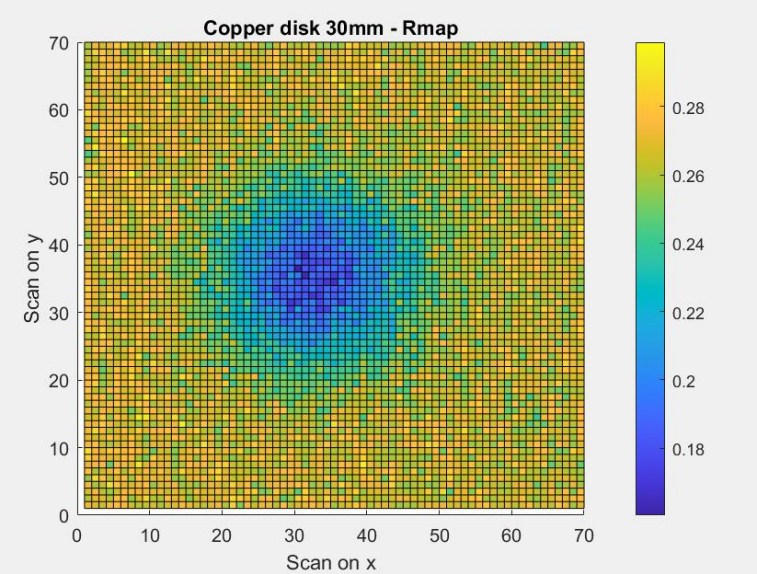

Figure 6.6: Copper Disk 30 mm - Set R. Two-dimensional noise representation observed in a plane x,y.

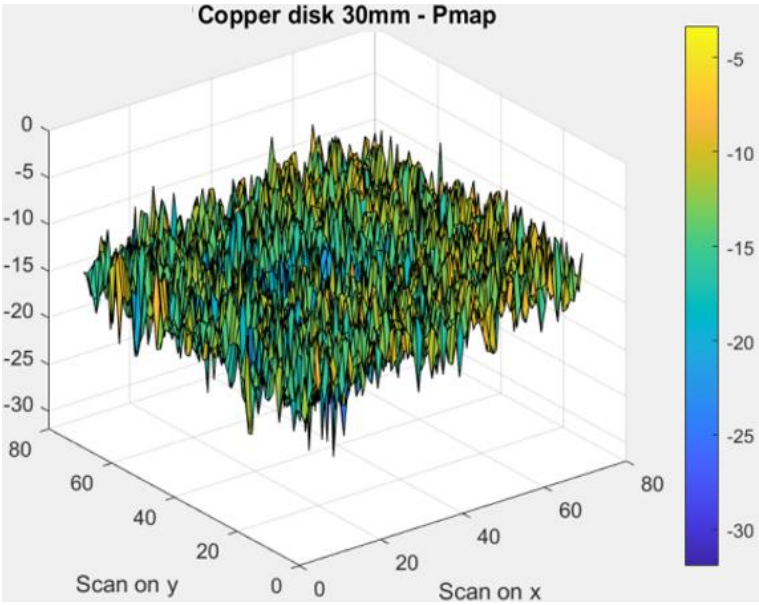

Figure 6.7: Copper Disk 30 mm - Set P. Three-dimensional representation.

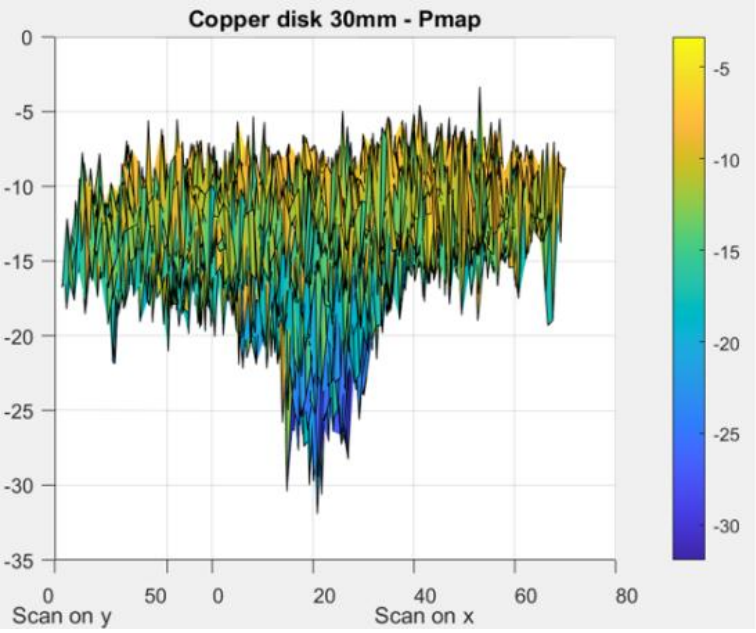

Figure 6.8: Copper Disk 30 millimeters - Set P. Three dimensional representation.

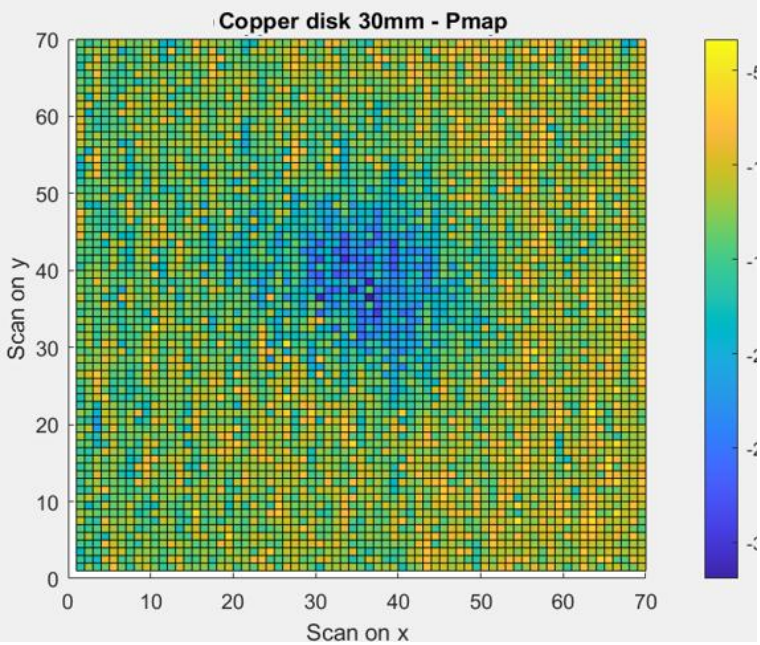

Figure 6.9: Copper Disk 30 mm. Set - P. Two dimensional representation observed in x,y plane.

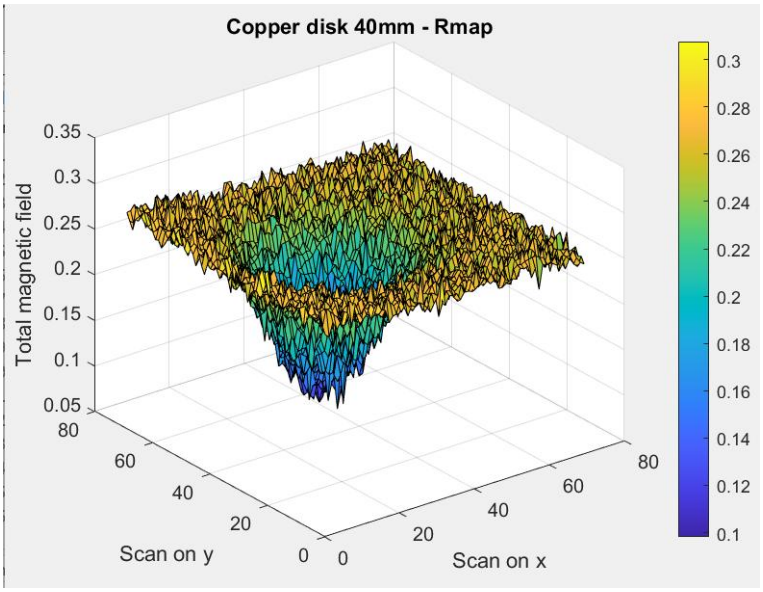

Figure 6.10: Copper Disk 40 mm - Set R. Three-dimensional representation.

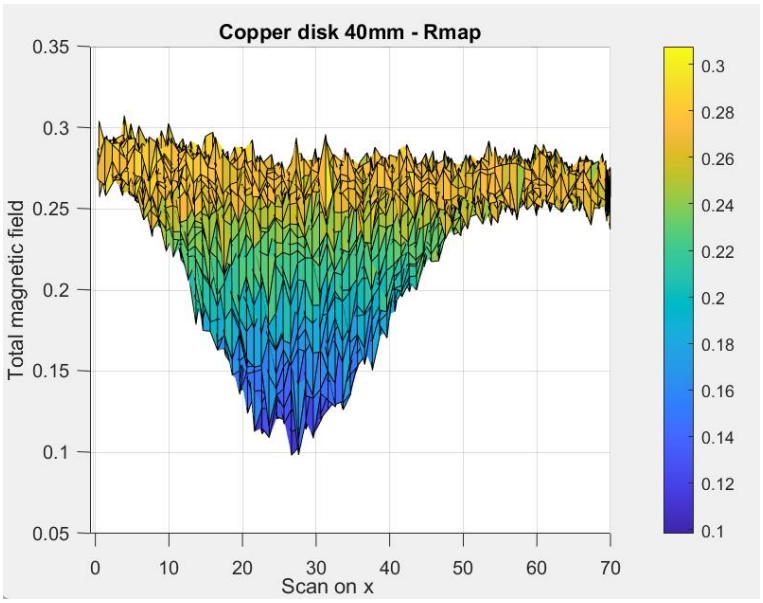

Figure 6.11: Copper Disk 40 mm - Set R: Two-dimensional representation of noise observed in a plane of a fixed y.

.

.

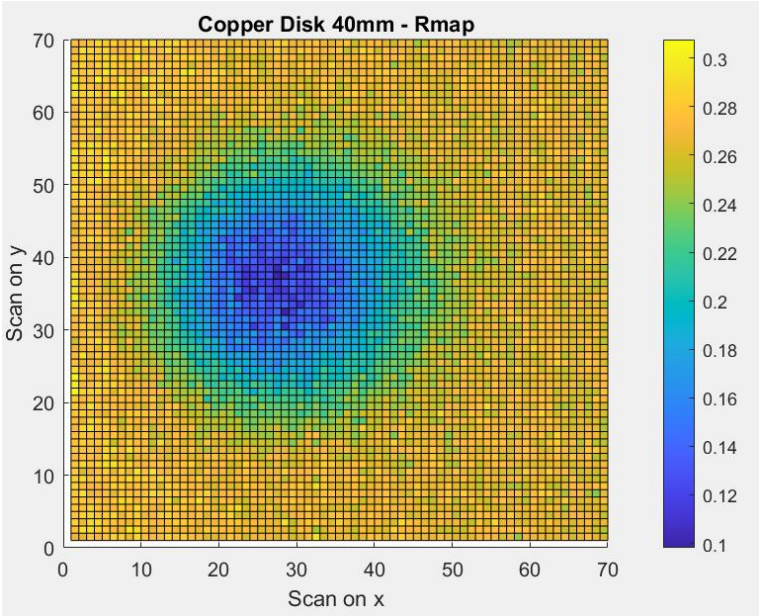

Figure 6.12: Copper Disk 40 mm - Set R: Two-dimensional representation of noise observed in a plane x,y.

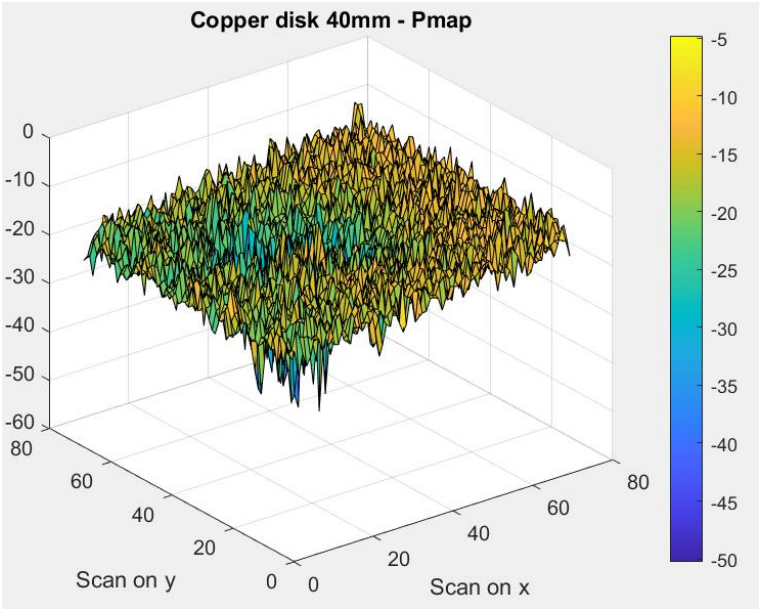

Figure 6.13: Copper Disk 40 millimeters - Set P. Three-dimensional noise representation of noise observed in plane x,y.

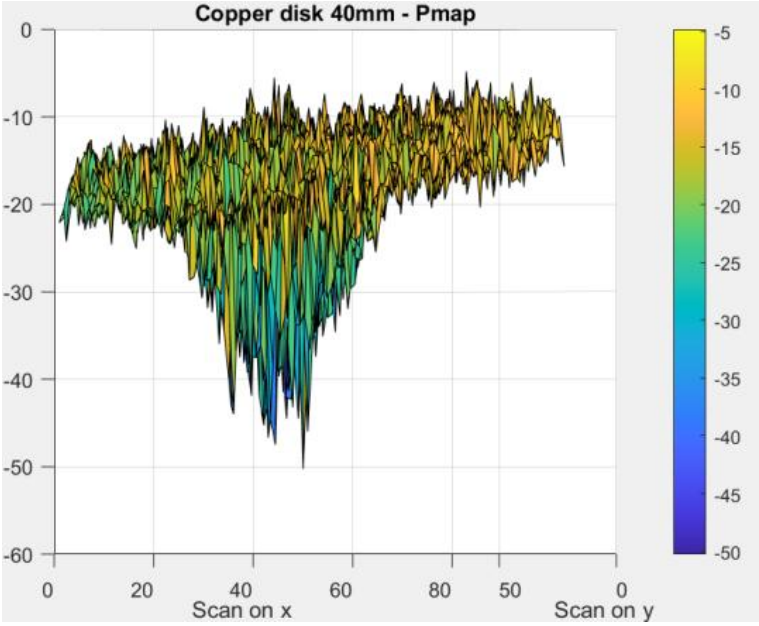

Figure 6.14: Copper Disk 40 millimeters - Set P. Three-dimensional noise representation from a different point of view respect to the previous one.

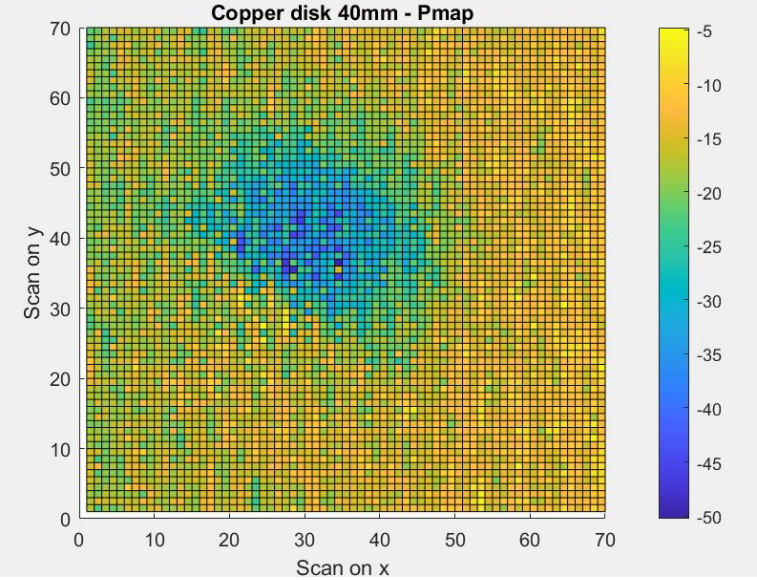

Figure 6.15: Copper Disk 40 millimeters - Set P. Two-dimensional noise representation observed in plane x,y.

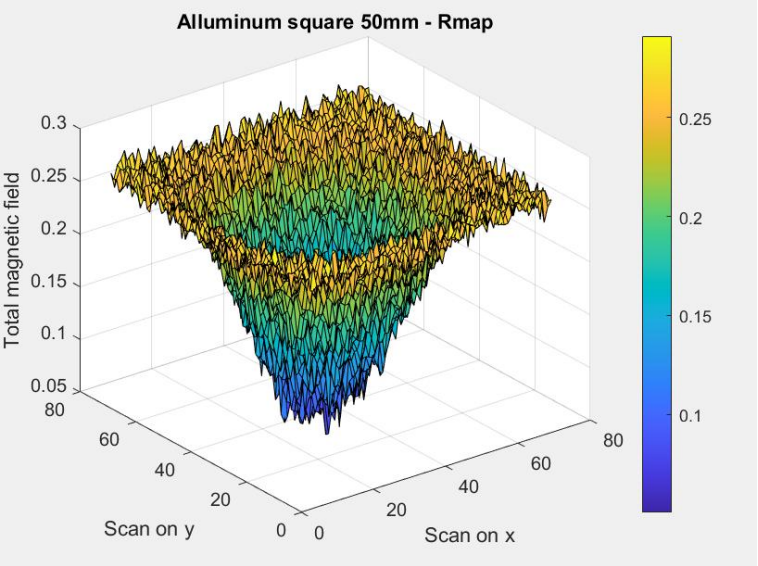

Figure 6.16: Aluminum square 50 mm - Set R. Three dimensional noise representation observed in x,y.

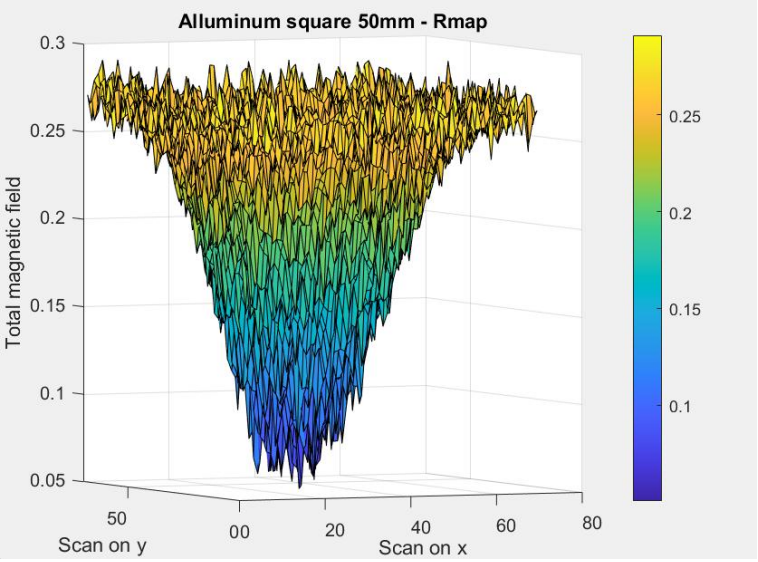

Figure 6.17: Aluminum square 50 mm - Set R. Three-dimensional noise representation from a different point of view respect on the previous one.

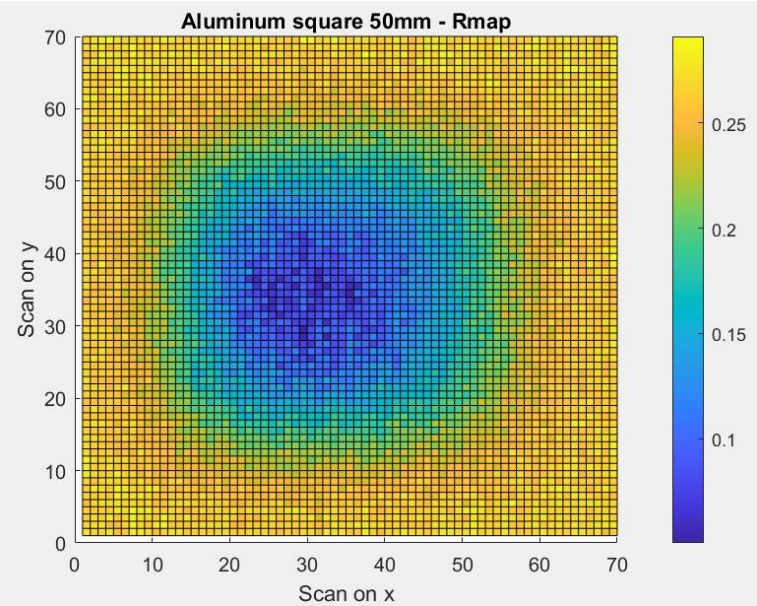

Figure 6.18: Aluminum square 50 mm - Set R. Two-dimensional noise representation in plane x,y.

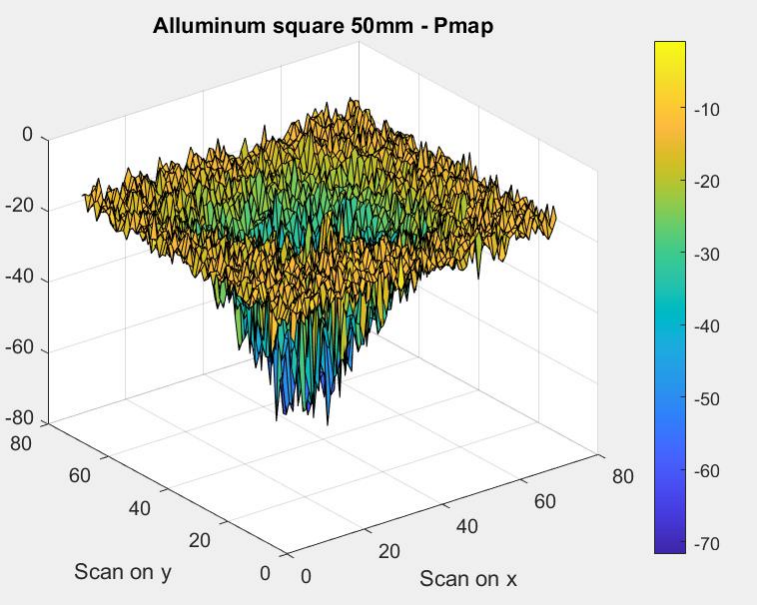

Figure 6.19: Aluminum square 50 mm - Set P. Three-dimensional noise representation.

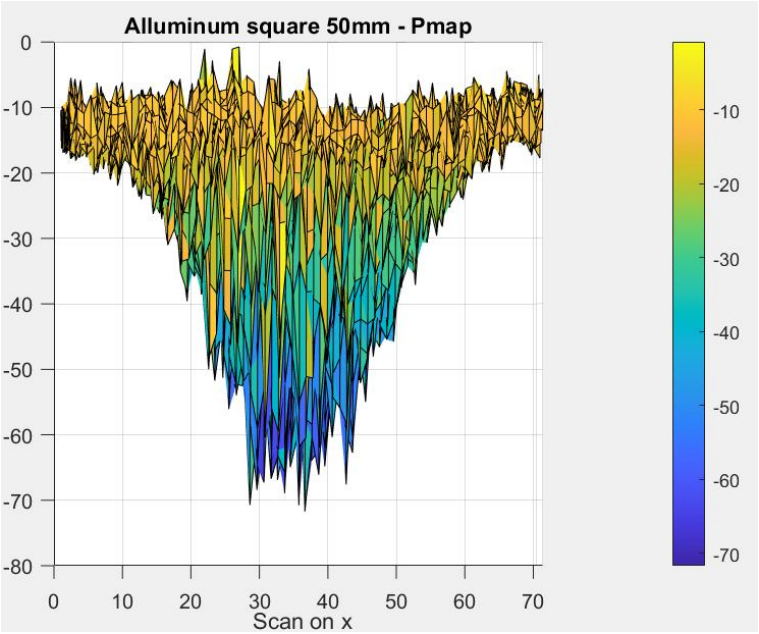

Figure 6.20: Aluminum square 50 mm - Set P. Two-dimensional noise representation in a plane of a fixed y.

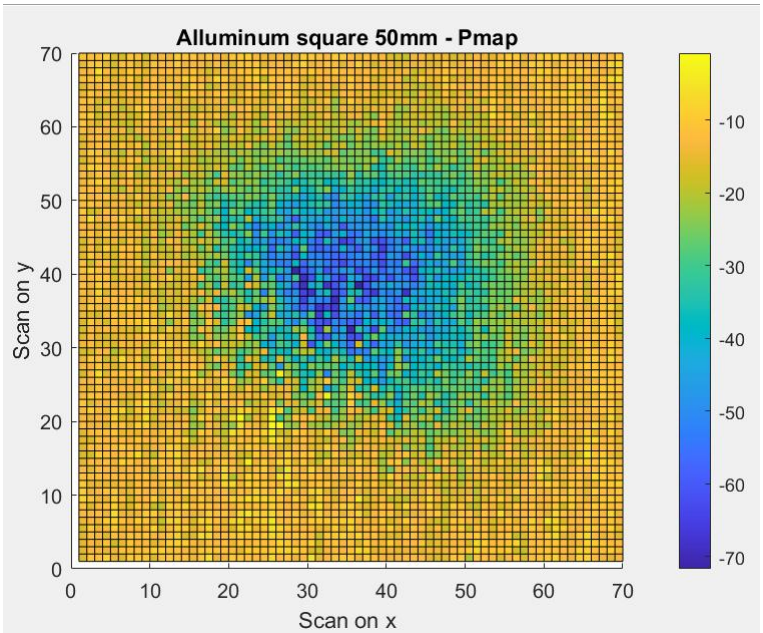

Figure 6.21: Aluminum square 50 mm - Set P. Two-dimensional noise representation in plane x,y.

6.3.2 Gaussian Noise

Generally we assume that the noise has a Gaussian profile, so we have to treat datasets from OAM magnetometry with the hypothesis of being in the presence of Gaussian noise. In order to clean the images from noise, it is useful to perform a histogram image transformation where it is reported how many values ($Counts$) of the matrix 70×70 fall in an interval in a given range (bin), for ease we consider $100 bins$ and so a separation in value of 0.01 for each bin. If we had just pure noise, the histogram should indicate a simple Gaussian curve. The Figures 6.25, 6.29 and 6.33 represent the images of R_{map}. The $x - axis$ corresponds to the bins normalized at unity, while in the $y - axis$ the counts are reported. The curve centered about 0.25 shows an almost Gaussian behavior, while the asymmetry at higher bin values is due to the presence of the conductive sample.

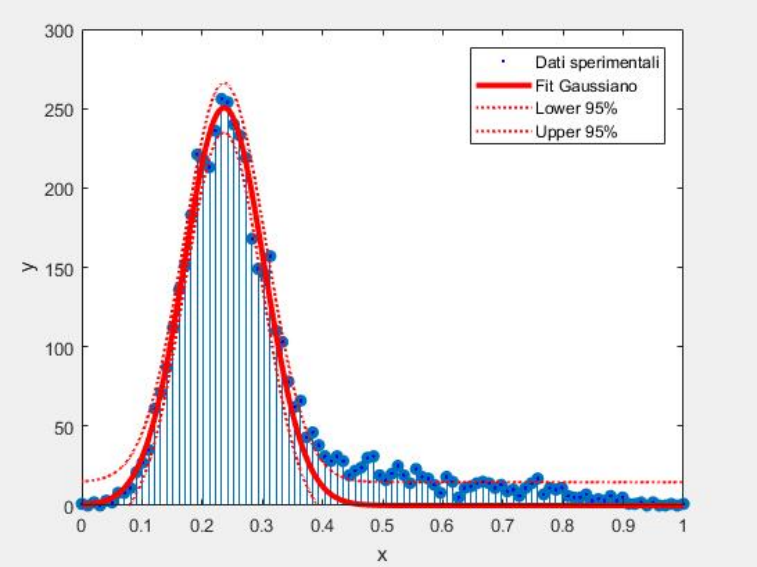

Figure 6.22: Copper Disk 30 millimeters Set R - Gaussian Noise

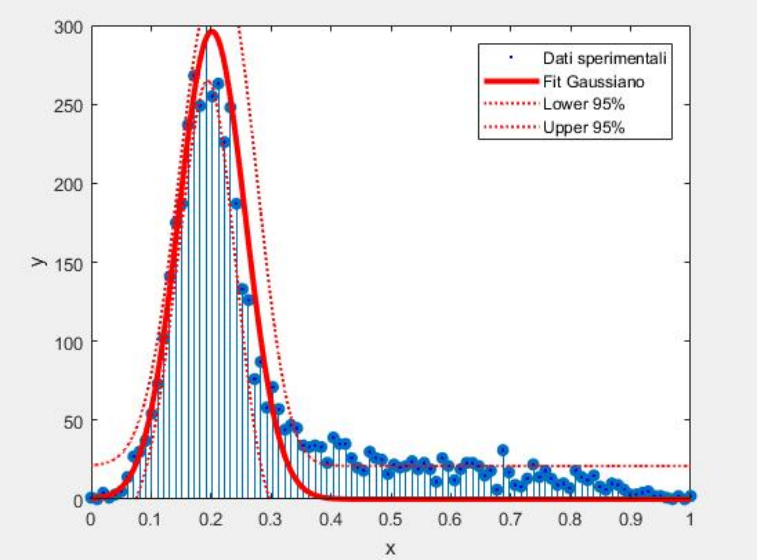

Figure 6.23: Copper Disk 40 millimeters Set R - Gaussian Noise

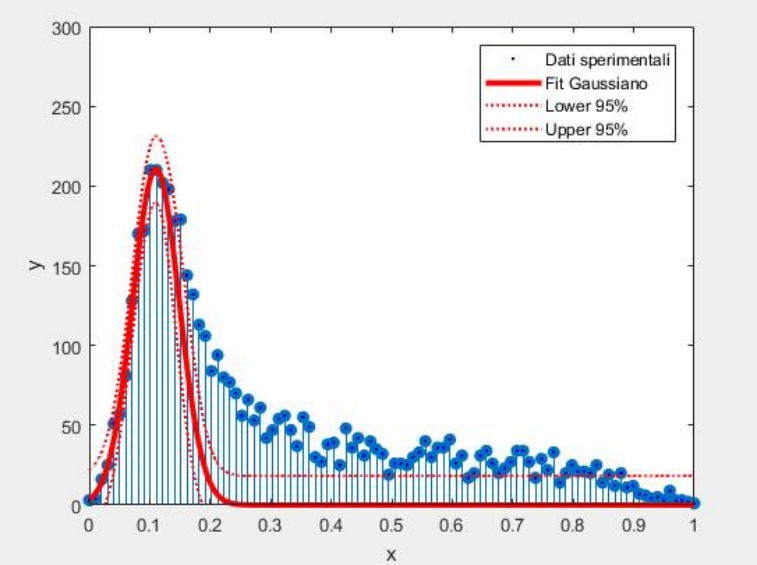

Figure 6.24: Alluminum square 50 millimeters Set R - Gaussian noise.

After these considerations, it is evident that the borders of the sample are located at the right side of the Gaussian curve, exactly where the symmetry is broken from secondary fields on the surface of the sample.
Although a Gaussian Noise hypothesis is the most generic behavior for background signal, a confirmation of this hypothesis is needed before proceeding with the analysis, because the cleaning procedure strongly depends on the Gaussian Noise Characterization. Therefore, considering now a single row or a single column at the border of the 70×70 matrix of collected data, where any contribution due to secondary field from the sample is minimized (or, better, is absent), we have to check if the distribution of the values follows a Gaussian shape.
Defining the mean and the standard deviation of the selected data as usual:

$$\mu = \sum_{i=1}^{N} = \frac{x_i}{N} \tag{6.1}$$

$$\sigma = \sqrt{\frac{1}{N}\sum (x_i - \mu)^2} \tag{6.2}$$

we construct the Normal Distribution with the same mean and standard deviation of the noise data-set.
As a next step, we have to proceed with the analysis of the following rows/-columns until we start to evidence a lack of symmetry, that is the signature of the border of the sample. An iterative fitting process has been embedded

on the algorithm considering several histograms where the fits are performed. In order to select the best parameters, resulting from the best fit performed, it is necessary to introduce a merit figure as root-mean-square-error (RMSE) defined as:

$$RMSE = \sqrt{\sum_{i}^{N} \frac{(x_o i - x_p i)^2}{\gamma}} \tag{6.3}$$

where x_0 and x_p are the observed and predicted counts for each bin interval and γ represents the degrees of freedom of the fit.
It is evident that the best fit procedure yields the lower RMSE: in this way we can extrapolate the best Gaussian parameters which describe the noise behavior.
A typical fit has been posted in Figures 6.25, 6.29, 6.33.

6.3.3 Statistical Indicators: Skewness

To estimate the goodness of the fit we used some statistical indicators, that is, tools with which a statistical phenomenon can be described in a synthetic way. A statistical indicator is basically a number that is obtained in an appropriate way by operating through differences and ratios between the statistical data collected and possibly multiplying the ratios by convenient powers of 10. It provides information on the reciprocal behavior of the same data and, consequently, on the statistical phenomenon to be studied. In our case, we used skewness which measures the lack of symmetry in a data distribution; it can be negative or positive, depending on whether the data points are tilted left and negative, or right and positive with respect to the mean of the data. A truly symmetrical dataset would have skewness of 0. After having represented the Gaussian that describes the noise, the application of skewness allows us to identify the point where the curve begins to show a loss of symmetry; it essentially measures the relative size of the two tails. In other words, the point where the presence of the metal sample under study begins to perturb the electromagnetic field. By calculating skewness of 1.87, a noise Gaussian-like curve is distinctively visible centered about 0.25, describing the noise values, and a long tail toward higher values where the disk is present causing the asymmetry.

6.4 Filtering

The problem of eliminating the so called outlayers, i.e. the points generated by noise clearly far from the rest of the dataset, could be solved through the use of filters. Usually the word *filter* makes us think of elaboration of images not only in sciences but also in arts, from Alan Turing to Andy Warhol. In this Thesis we used convolution filters in order to clean up the sets of data from NMR experiment.
For many years now *MatLab* has been incorporating a toolbox for processing digital images, accompanied by a set of graphic tools useful for assessing the quality of the same draw graphs of some features, such as an histogram. The processing applied to the images is often computationally very demanding and, precisely for this reason, in the last few years a branch of the GPU has developed computing dedicated specifically to image processing.
Digital images can be processed for various purposes, such as: correct imperfections which occurred during the acquisition or the transmission, improve the visual rendering, introduce artistic effects.
There are numerous applications of filtering to images: noise removal, image sharpening, edge enhancement, image de-blurring. The convolution is implemented through a sliding window on the data, which is precisely the response to the unitary impulse. The convolution filters use local neighbors to compute the weighted average, and each pixel is used multiple times by its neighbors.

6.4.1 Convolution filters

There are a large number of different convolution filters that are commonly used for processing images. Most software will also come with a large number of prepackaged filters already implemented. For instance, edge-detection methods are quite useful in a variety of compositing situations and as most such operators will feature a number of additional useful parameters for fine-tuning the result. Convolution is a popular array operation which is used in various forms in signal processing, digital recording, image processing, video processing, and computer vision. Convolution typically involves a significant number of arithmetic and logic operations on each data element. In general, the convolution filter, consists of replacing the brightness of a pixel with a brightness value computed with the eight neighbors brightness value: an im-

age can be seen as a matrix I, where $I(x, y)$ is the brightness of the pixel located at coordinates (x, y). A convolution product is computed between the matrix I and a kernel matrix K which represents the type of filter. In image processing, convolution is a commonly used algorithm which modifies the value of each pixel in an image by using information from neighboring pixels. A convolution kernel, or filter, describes how each pixel will be influenced by its neighbors. Using the same source image and changing only the filter, one can produce effects such as sharpening, blurring, edge enhancing, and embossing.

Convolution algorithms work by iterating over each pixel in the source image. For each source pixel, the filter is centered over the pixel, and the values of the filter multiply the pixel values which they overlay.

The approach shown here accelerates convolution by encoding the convolution filter into a texture image. A matrix 70×70, whose color is the random value to be convolved, is rendered with the monochrome texture containing the convolution filter image applied to it. It is possible to observe, on a blue background, the presence of experimental sample in red scale. The fundamental problem arises when identifying with extreme definition the edge of the sample.

The convolution operation can be implemented using a combination of texturing and blending. A texture map contains the desired filter weights for each pixel neighbor. The resolution of the texture filter is determined by the complexity of the filtering function. The texture performs two functions: it spreads the sample value over the region of the rectangle and modulates the sample value at the resolution of the filter texture.

There are a number of parameters that need to be adjusted properly to get the desired filtering.

To avoid artifacts at the edges of the image, the filter function should extend beyond the bounds of the image, just as it does for normal convolution operations. This group of output pixels that will be considered is known as the kernel, and is usually a square group of pixels that has an odd number of rows and columns. We then multiply each pixel by the coefficient with which it is aligned.

The particular filter we applied in this example is one which is designed to detect edges in an image. As one can see, it produced a bright pixel wherever there was a transition area in the original image, and produced dark pixels wherever the source image had a constant tone.

The convolution technique changes each value of the raw 70×70 matrix with the mean of its neighbors smoothing the noise value.
Because the outliers are randomly dispersed, the mean around their position is lower with respect to the edges of the sample, where the convolution masking technique is essentially useless.
However, if the SNR is sufficiently high, biggest threshold can be selected in order to avoid the the implementing of masking method.
An additional circle fit has been embedded to estimate coordinates of the samples.

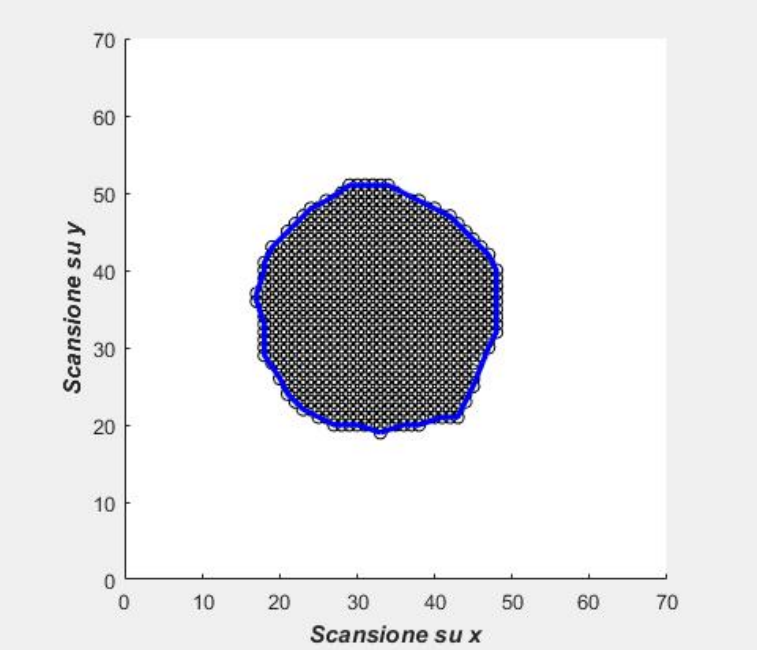

Figure 6.25: Digital reconstruction of copper disk 30mm imagine - Set R.

A particularly interesting case concerns the detection of a crack operated on an aluminum ring. This experiment takes on particular relevance; the crack is on a millimeter scale, but despite this it was easy to identify it. In the region of the crack the secondary field around it should be absent because the eddy currents are suppressed by the dielectric interspace. It is evident the drop of the signal field values in correspondence of the cut in the ring. The analysis algorithm are able to detect details under $1mm$ in size. The bigger dimension of the coil with respect to the crack does not permit a full resolution of the defect.

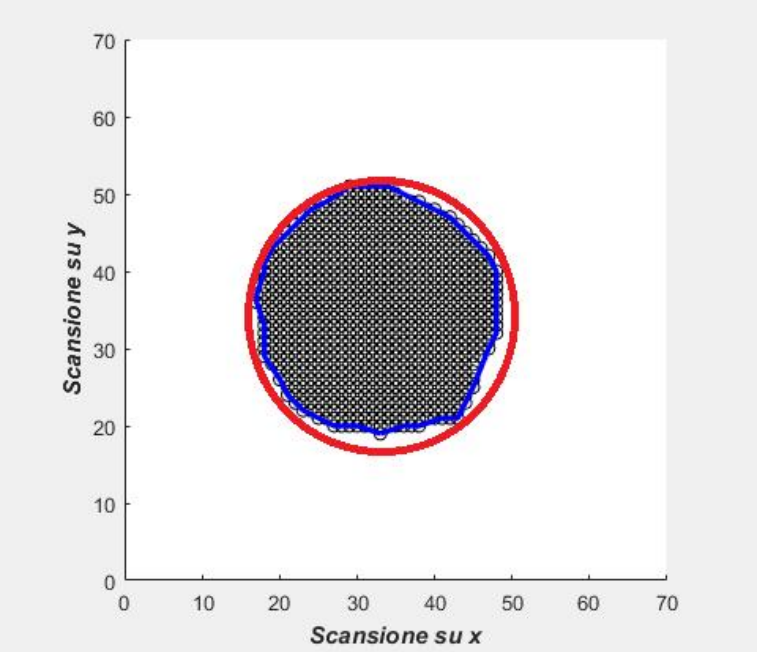

Figure 6.26: Copper disk 30mm fit - Set R.

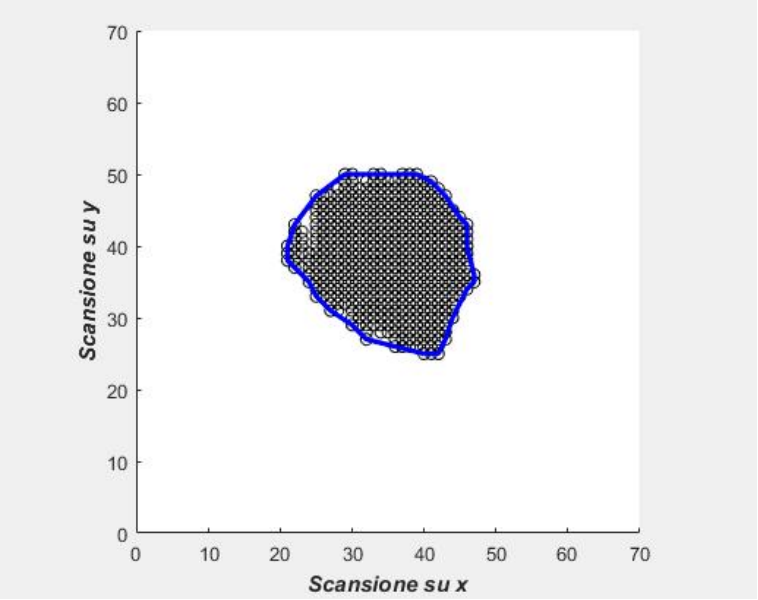

Figure 6.27: Digital reconstruction of copper disk 40mm imagine - Set P.

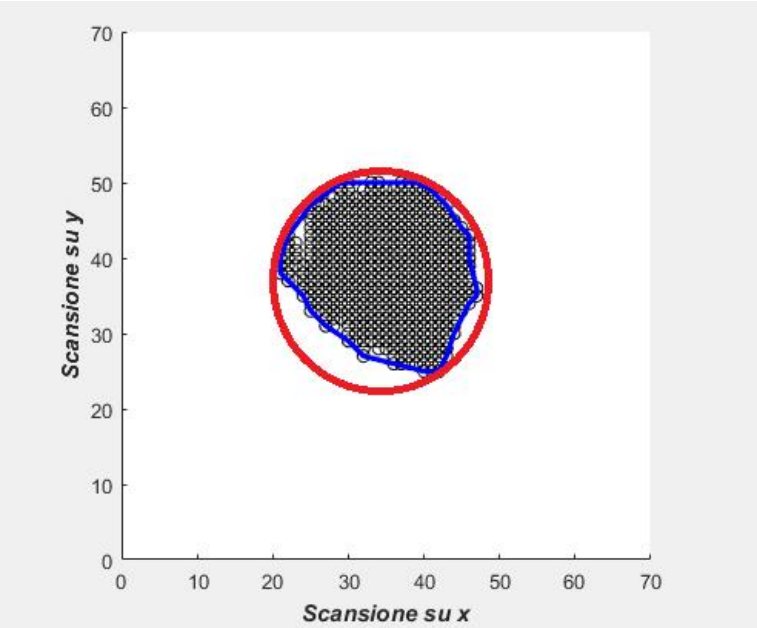

Figure 6.28: Copper disk 30mm fit - Set P.

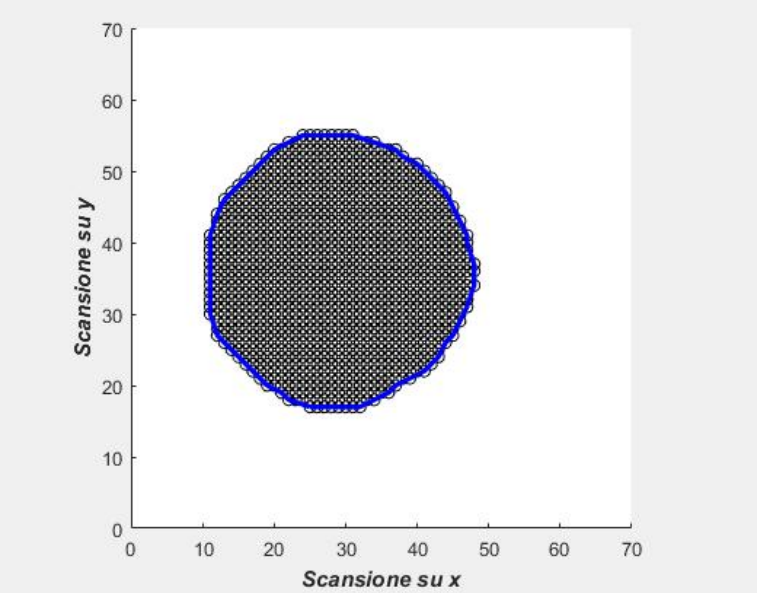

Figure 6.29: Digital reconstruction of copper disk 40mm imagine - Set R.

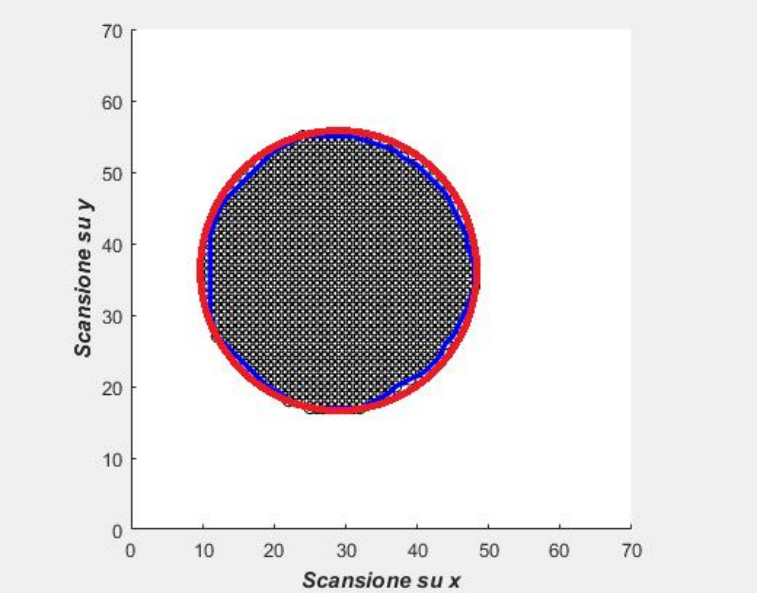

Figure 6.30: Copper disk 40mm fit - Set R.

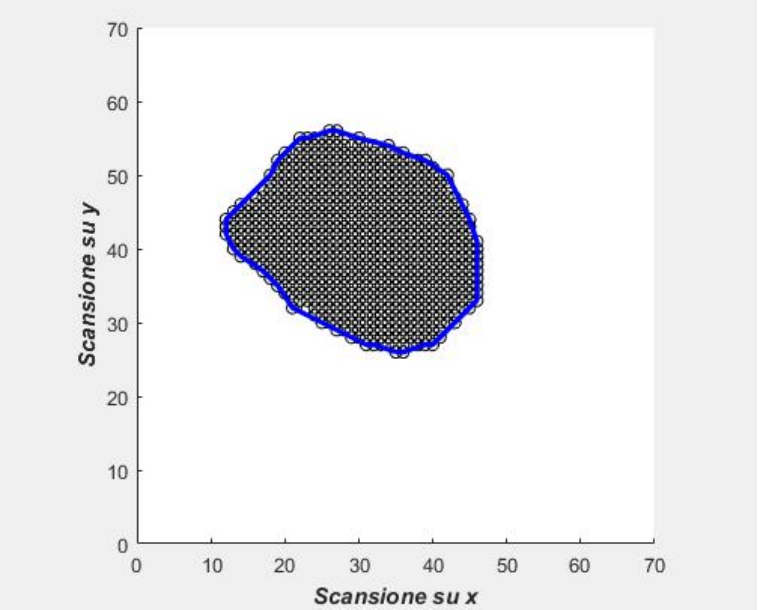

Figure 6.31: Digital reconstruction of copper disk 40mm imagine - Set P.

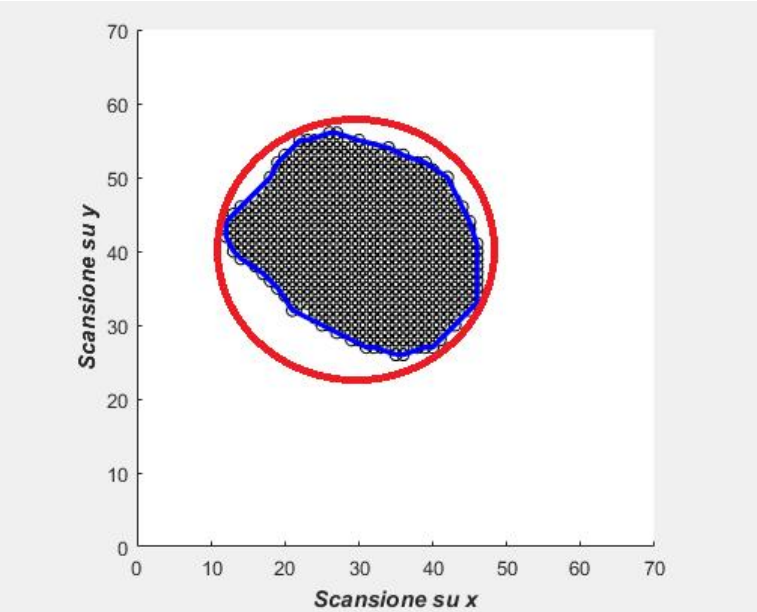

Figure 6.32: Copper disk 40mm fit - Set P.

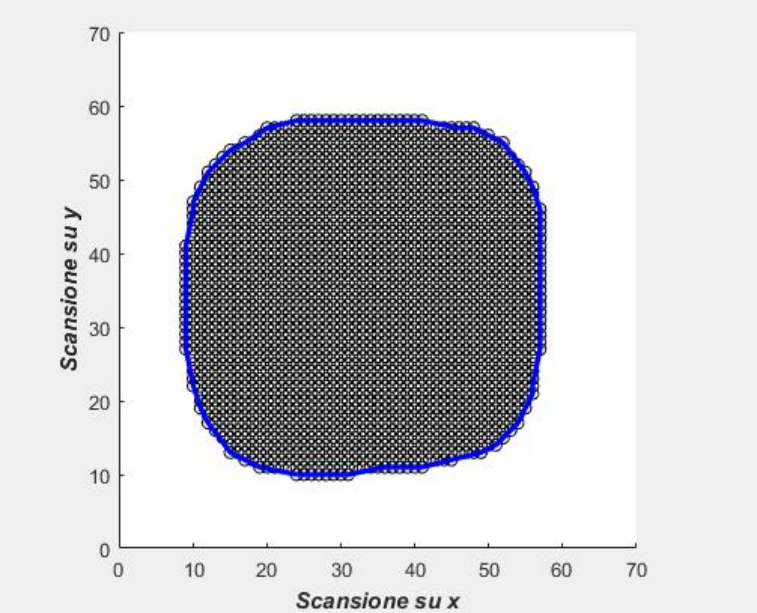

Figure 6.33: Digital reconstruction of aluminum square 50mm imagine - Set R.

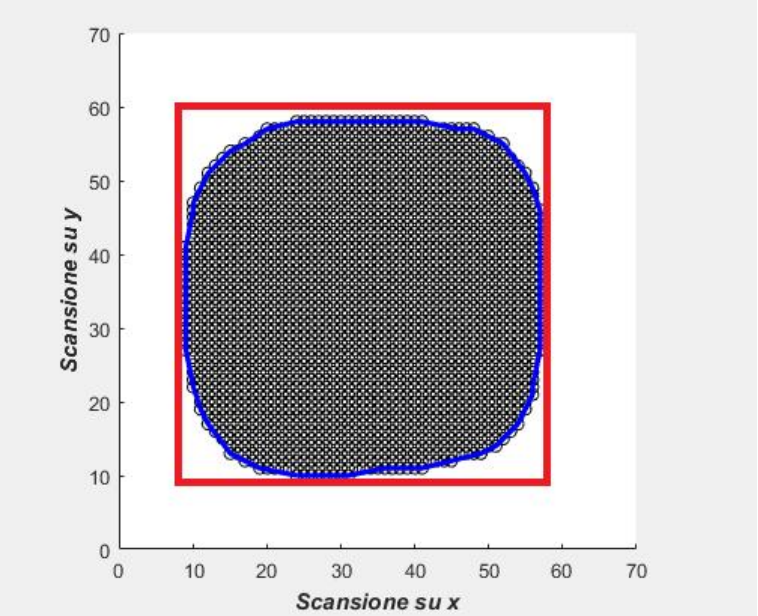

Figure 6.34: Aluminum square 50mm fit - Set R.

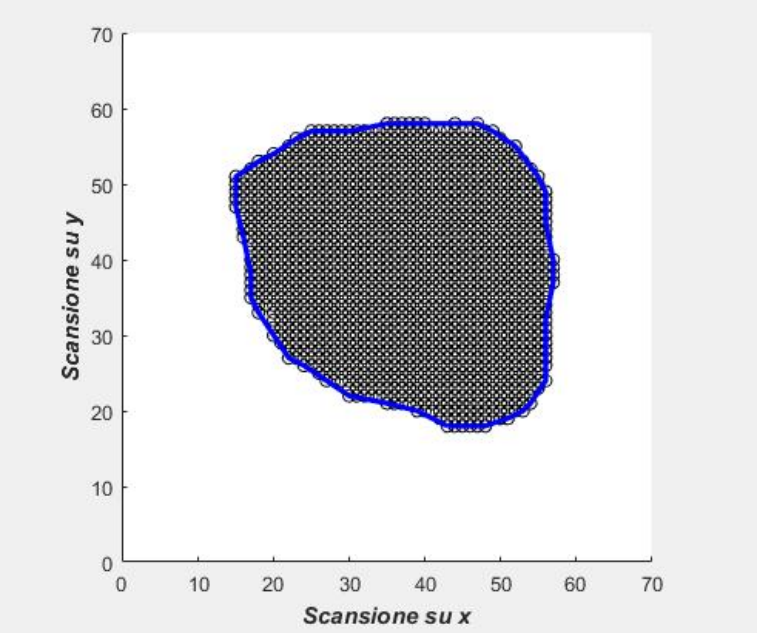

Figure 6.35: Digital reconstruction of aluminum square 50mm imagine - Set P.

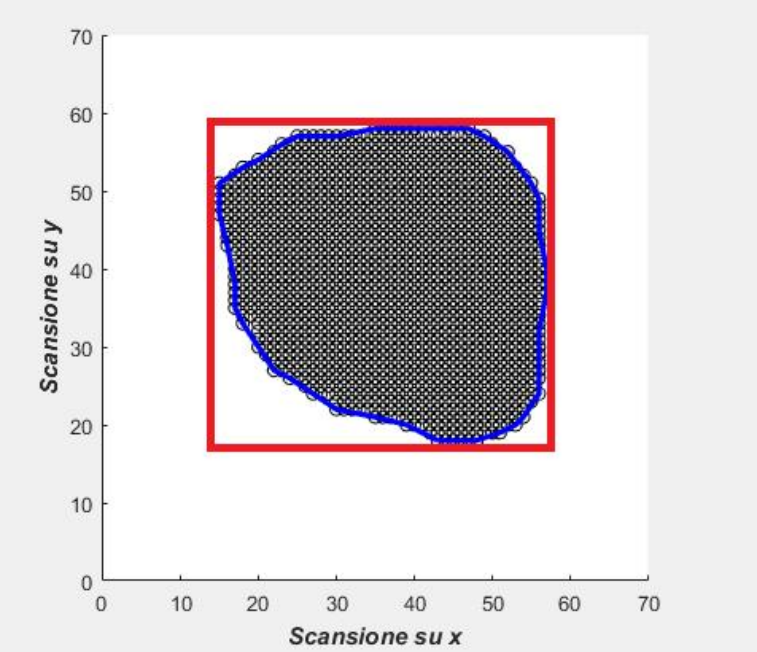

Figure 6.36: Aluminum square 50mm fit - Set P.

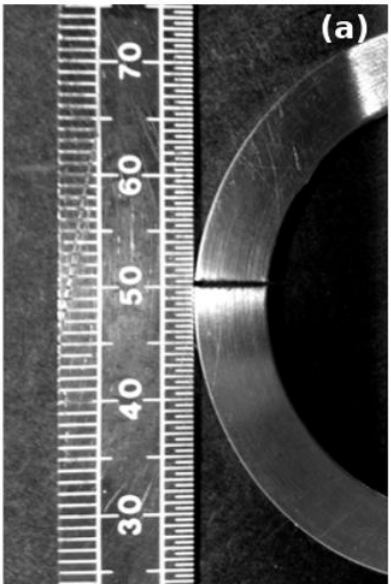

Figure 6.37: Real image of the crack in an aluminum ring.

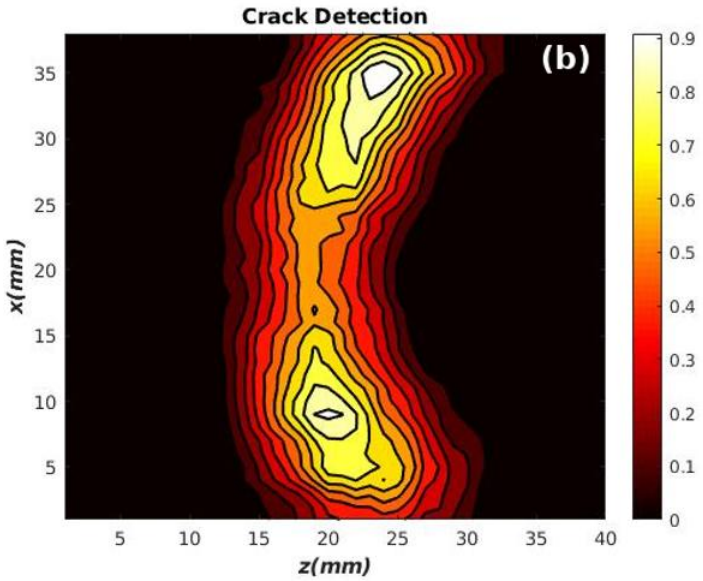

Figure 6.38: Crack detection. The Figure is an advanced processing compared to what is contained in [41]

6.5 Conclusions

The goal of this thesis is the data processing about an OAM experiment. The analysis procedure has characteristic of generality and it is independent from kind of samples. Only by using the Gaussian Noise parameters, i.e. the amplitude A, the mean μ and the standard deviation σ_G obtained from the fit method, we can remove noise contributions from the original data. This was possible by the implementation of a threshold in terms of Gaussian Noise's standard deviation, in our case $T = 3\sigma_G$.

At higher threshold values there correspond a less noisy image result and a reduction of the size of the sample, otherwise at lower threshold value the image results more noised.

Even though there is a hidden relationship between the signal-to-noise-ratio (SNR) and the threshold value still unknown, good results are obtained with empirical value of $T = 3\sigma_G$ at $SNR \sim 4$.

In fact this value statistically removes the 90% of the noise contribution. The analysis method applied to Magnetometer Resonance Imaging permits the detection of a conductivity sample by the characterization of noise background from R_{map}.

We demonstrated its performance in determining the dimension of the sample and in tracing sample borders. The error is lower than the dimension of coil. The experimental setup and the analysis method achieved a sensibility under $1mm$ in size in unshielded environment.

Compared to original data, the cleaning procedure massively removes the noise background emphasizing the edge of the sample.

In addition, our algorithm does not impact on original data avoiding any loss of original information.

Appendix A

Atomic models

In this appendix we present a brief history of *atomic theory* and of the models developed in the last two centuries. The history of atomic theory is intertwined at first with philosophy, subsequently with alchemy and only in the last instance with chemistry and physics.
The path of investigation on the matter begins from afar, in ancient Greece with the philosophical current called major exponents are Leucippus ($early-first\ half\ of\ the\ fifth\ century$ BC, $-\ third\ quarter\ of\ the\ fifth\ century$ BC), Zeno of Elea ($495-445$ BC) and Democritus ($430-370$ BC). The starting point was the problems of infinite divisibility already conceived in a geometric context.
Atomism is in fact a natural philosophical orientation of an ontological character based on the plurality of the fundamental constituents of physical reality. In this conception the perceptible world consists of two parts: the indivisible atoms and the void.
Atoms are microscopic elements, indivisible and qualified by shape, arrangement and position, contained in the vacuum inside which they move randomly and rapidly. This approach was purely qualitative and the conjectures were mostly based on arguments of plausibility rather than on direct clues as claimed in modern science.
Titus Lucretius Carus ($98-55$ BC) was able to translate this philosophical theory into lofty poetry, imagining recognizing in the dance of particles of dust in a ray of sunshine an example of what, many centuries later, will be described as a "*Brownian motion*".
In the following two thousand years, the debate on the intimate nature of matter would have seen *Platonism* and *Aristotelianism* borrow from the

theory of Empedocles (*V century* BC) the idea that the perceptible world was composed of four main elements (*Air*, *Earth*, *Fire*, *Water*).
Aristotle (383 *B.C.*-322 BC), in particular, is strenuously opposed to the existence of the void and, in his physical theory to explain the substance, it is convenient to refer to the matter-form and power-act couples.
We will have to wait for the *Age of Enlightenment* for Atomism, which remained on the sidelines of scientific investigation into Nature, to receive new vital lymph.
At that time, scientists such as Joseph-Louis Proust (1754 – 1826), John Dalton (1766 – 1844) and Joseph-Louis Gay-Lussac (1778 – 1850) showed that thinking in terms of atoms was extremely effective. The model of a gas made up of non-interacting atoms, the perfect gas, applicable with good approximation in the case of rare gases, consolidates this way of thinking.
A turning point in the process of "*atomization*" of physical reality was the work of Amedeo Avogadro (1776 – 1856) who guessed that equal volumes of gas under the same conditions of pressure and temperature contain the same number of molecules.
The introduction of the notions of molecule and mole paved the way for modern chemistry which culminated in the compilation by Dmitry Ivanovic Mendeleev (1834 – 1907) of the *Periodic Table of the Elements* which constitutes the extraordinary face of the hypotheses atoms is hypothesis of Atomism.
At this point the theater of the investigations moved inside the atom which, following discoveries made in the decades between the nineteenth and twentieth centuries, began to lose the concept of indivisible particle. The scientific community was troubled for a long time by hypotheses about the atomic structure and within two decades numerous models were developed to explain the nature of atoms.
We can categorize these models into two main categories: pre-quantum and quantum models. The first atomic models were numerous, many more than we commonly remember; some of them contained innovative scientific insights that today live on in physical theories different from the originals.
The Italian physicist and astronomer Ottaviano Fabrizio Mossotti (1791 – 1863) proposed to describe the electrical behavior of the atom starting from the assumption that it could be approximated as a perfectly conductive sphere. In this case, the dipole moment induced by the action of an ex-

ternal field is

$$\mathbf{p} = \mathbf{E}a^2 \tag{A.1}$$

The first worth mentioning dates back to 1901, by the French scientist Jean Baptiste Perrin $(1870 - 1942)$; the French scientist stated that "the virtue of Atomism is to explain the complicated visible with the simple invisible"
From the modeling point of view, he assumed that each atom was made up of both various positively charged masses ("*soleils*") and a multitude of negative corpuscles ("*planetes*") that gravitated under the action of electrical forces. The total negative charge was exactly equivalent to the total positive charge so that the atom was electrically neutral.
The "*dynamid*" model proposed by Philipp Eduard Anton von Lenard $(1862-1947)$, on the other hand, dates back to 1903, who had made remarkable observations on the behavior of electrons by demonstrating that the absorption of electrons depended more on the mass of material than on the its specific composition or its chemical properties; he also proved that the interaction forces were essentially electrical and that these forces controlled chemical interactions. His atomic model was structured as a model presented a pair of positive and negative charges linked together, the dynamid in fact. The forces that held the dynamids together were not explained but the theory accounted for the structure of the periodic table and the presence of electrons in atoms even if it was unable to explain Rydberg's formula for hydrogen spectra.
In theory, the positive components should have been equally extractable than the negative ones from the atom but this, in practice, did not happen.
Just a year later, in 1904 Japanese physicist Hantaro Nagaoka $(1865 - 1950)$ revisited a 1859 work by James Clerk Maxwell in which it was shown that Saturn's rings were sufficiently stable and made up of a relatively small series of objects; the inevitable disturbances of the orbit only caused oscillations but not the destruction of the ring. The Japanese physicist applied the same mathematical idea, however, assuming that the rotating bodies did not attract each other as it happened with the components of Saturn's ring, but repelled each other. He mathematically proved that the oscillations of the electron ring produced spectral lines and a continuous band structure, that in the presence of a magnetic field a splitting effect would be produced and proposed that radioactivity depended on repulsive effects between different electron rings around to the same atom. His proposal, despite the remarkable

explanatory success that included ghosts, did not have much resonance.
This model, however, was unstable due to the Coulomb repulsive forces between electrons which did not allow to apply the same laws used for Saturn, in which gravitational, i.e. attractive, forces were at play. The objection of such an electron system was that the system had to eventually stop as a result of the exhaustion of the energy it radiated, if the loss was not properly compensated.
However, in this historical ridge there were still those, like Lord William Thomson, I Baron Kelvin ($1824 - 1907$), struggled to think of the behavior of sub-atomic constituents as "*corpuscles*", remaining attached to the fluidistic theory of electricity to a only Epino fluid: the positive and negative electrifications consist of excesses and deficiencies with respect to an electric fluid that permeates all the space between the atoms of the ponderable matter. Portions of matter devoid of electric fluid repel each other; portions of electric fluid repel each other; portions of electric fluid and fluid-free matter attract each other.
In other words, Kelvin believed that the positive charge inside the atom should be assigned to a homogeneous and continuous mass, to be thought of as fluids are ordinarily thought of, that is, as a kind of very low density gelatinous mass. Among the other "*defeated*" atomic structure models we include. George Adolphus Augustus Schott ($1868-1937$), a true "master" of Maxwell's electromagnetic theory and extreme champion of classical physics. He tried until his death in 1937 to develop a traditional approach that lived up to experimental observations. In particular, he argued that the solution may come from an internal structure of the electron that provides that the electron is not a point particle and that it instead expands, albeit at low speed. This proposal would conflict with the conservation of energy and therefore the author is forced to consider an internal stress in the electron caused by the pressure exerted by the ether. Schott also proposed, on an analytical basis, that this phenomenon of interaction between aether and electron is at the origin of gravity.
Between 1904 and 1907 Schott tried to perfect the ideas of Thomson and Nagaoka; the latter, in particular, argued that the Saturnian model was not necessarily neutral from an electrical point of view as the nucleus could have a very strong charge compared to that of the electrons. Schott observed that this was not the reason why the instability problem became very serious. He was therefore able, again analytically, to demonstrate that the perturbations

increased in intensity by about a factor of three for every three electronic revolutions.
Then he tried to overcome the difficulties of his atomic model by modifying the "usual conceptions on the constitution of the electron and the ether", suggesting for example to discuss electrons as if they were subject to variation in radius.
Scott's theory, like Nagaoka's, was discarded in favor of the one proposed by Thomson which was better suited to the experimental data of the spectra and took electrical phenomena into due consideration.
In 1906 came a proposal John William Strutt III Baron of Rayleigh (1842 – 1919). Such a fluid is irrotational, i.e. there is no element that rotates around the axis passing through the center of mass of the element itself. This greatly simplifies the calculations and combined with the supposed incompressibility it facilitates the mathematical modeling. The electronic fluid, therefore, oscillates but does not rotate around the center and does so with discrete and calculable frequencies, but which do not turn out to be those of Rydberg, a difficulty that Rayleigh tries to overcome by considering them as "*beats*" of much higher frequencies.
Rayleigh also comes to the conclusion that other conditions are probably needed to justify that the oscillation frequencies are only those detected, an idea that somehow is in accordance with the requirements of the QM.
Rayleigh's ideas are powerful, they eliminate the need for regular rotation but point to the need for new conditions. This fluid was irrotational (which simplified the calculations), incompressible, it underwent vibrations of discrete frequency. He calculated this frequency but it did not correspond to that of Rydberg of the atom, so he sought an escape from these difficulties by considering the spectral lines as due to a "$difference\ in\ tone$" but he did not clearly describe the phenomenon.
As a conclusive observation, it can be noted that all the atomic models discussed present great theoretical difficulties relating to mechanical and electromagnetic stability, even if the presence of instability in the model could serve to explain the behavior of radioactive substances.
The *archion model* by Johannes Stark (1874 – 1957) dates back to 1910. In this original, insufficiently celebrated work, the idea of the proton is actually introduced, which is called "*archion*".
According to Stark's idea, the arch has a magnetic dipolar moment, which would allow the arch to bind head-to-tail with another arch, aligning itself to

form a closed circle that would give shape and structure to the atom as such. The weakness of the magnetic attraction between archions would be helped by the appropriate presence of electrons that would decrease the repulsion between archions. Once again this proposal does not respond to the need to foresee the Rydberg formula.

At this point, in the same 1910 an article was published by Paul Ehrenfest $(1880-1933)$, also fond of classical mechanics and also a seed for the future problem of creating invisibility materials. In a single seminal page, the scientist asked himself the question: is there a way in the context of Maxwell's theory to prevent a system of charges in accelerated motion from emitting electromagnetic radiation and therefore its energy from decreasing? Is it possible to switch to a vision that prevents the use of QM?

Ehrenfest's intuition was the possibility of admitting the existence of accelerating charge distributions that did not emit radiation.

Supposing we have, for example, an infinite plane sheet with homogeneous charge density that accelerates vertically, that is, perpendicular to itself; since the electromagnetic field is transverse, such a movement perpendicular to the surface does not correspond to the emission of radiation.

It is important to keep in mind that at the time of publication of this article the atomic models that focus on the problem of the stability of the motion of electric charges at the center were not yet established, so Ehrenfest's intuition was perfectly centered. If the motion of the system of charges is perpendicular to the surface, electromagnetic waves cannot be generated.

A system conceived in this way does not radiate, because it is an infinite non-point system like the example that is always done; obviously there are no infinite systems; but there is a finite solution: a uniformly charged sphere whose radius oscillates.

$$\nabla^2\varphi(x,y,z)=0 \tag{A.2}$$

$$\mathbf{E}=-\nabla\varphi \tag{A.3}$$

$$4\pi\rho=-\nabla^2\varphi \tag{A.4}$$

$$v=\frac{\frac{\partial}{\partial t}\nabla\varphi}{\nabla^2\varphi} \tag{A.5}$$

$$\mathbf{H}=0 \tag{A.6}$$

Appendix B

Gauss-Lamont's method

Based on both experimental and theoretical considerations, the magnetic field generated by a magnet is not due to the presence of the poles of magnetic masses similar to the charges that produce an electric field: the permanent magnetization is due to the *magnetons* associated with the atomic currents due to the electrons. In ferromagnetic materials they remain oriented even if the field that produced the orientation is removed.
The existence of the magnetic poles, that is, of an area in which the attractive or repulsive action of the magnet appears concentrated, is due to the orientation of the field that produced its polarization; thus a bar-shaped magnet has two well-defined poles at its ends if it has been magnetized in the presence of a field parallel to its axis.
From a practical point of view, however, it may be convenient to consider the magnetic masses and treat the field due to one of them as the analogous to the electrostatic case. In fact, it was theoretically and experimentally verified that the force acting between two polarities has the same properties as that observed between two electric charges; it is directed according to the joining of the two poles and has intensity

$$F = \frac{1}{4\mu\pi}\frac{p_1 p_2}{r^2} \tag{B.1}$$

where r is the distance between the poles and p_1 and p_2 are their magnetic masses. Furthermore, the magnetic moment of a magnet can be considered as the product of the magnetic mass of its poles and their distance

$$m = p \cdot d \tag{B.2}$$

We speak of magnetic poles in analogy with electric dipoles which are made up of two charges of equal and opposite values, placed at a certain distance

from each other. The mechanical moment produced by a magnetic mass p_1 on a moment dipole

$$m_2 = p_2 \cdot d \tag{B.3}$$

and

$$M = Fd\sin\vartheta = \frac{1}{4\pi\mu}\frac{p_1 p_2}{r^2}\sin\vartheta \tag{B.4}$$

and therefore in the point where the dipole is found there is a field

$$H = \frac{1}{4\pi\mu}\frac{p_1}{r^2} = \frac{F}{p_2} \tag{B.5}$$

The intensity of the magnetic field $\overrightarrow{H}$ can therefore be considered as the force acting on the unit magnetic mass. The famous geomagnetist Ciro Chistoni wrote important speculations on the measurement methodologies suggested by Gauss and perfected by Lamont. In these magnetometers the oscillation magnet is placed on the rod which acts as a deflecting magnet.
The relationship between the horizontal component H of the Earth's magnetism and the magnetic moment M, when the oscillation needle is at 0

$$\frac{H}{M} = \frac{2(1+a\tau)(1-hH\sin\varphi)}{R^3(1+3\beta\tau)\sin\varphi} \tag{B.6}$$

in which ϕ is the deviation of the magnetic axis of the suspended magnet, from the magnetic meridian, when this magnet is under the action of the oscillation needle at the distance R; a and h are respectively the temperature and induction coefficients of the oscillation needle; τ the temperature of the metric rod and the oscillation needle and β is the linear expansion coefficient of the bar on which the distances R are measured.
In most Gauss-Lamont magnetometers the bar is made of brass so $\beta = 0.000018$. The coefficients p and q depend on the size of the two magnets used to measure the deviations and on the distribution of the magnetism in them. Lamont had theoretically come to calculate the values of p and q

$$p = 0.1806(2l^2 - 3l_1^2) \tag{B.7}$$

$$q = 0,0326(3l^4 - 15l^2 l_1^2 + \frac{45}{8}l_1^4) \tag{B.8}$$

in which l is the length of the deflecting magnet, that is of the oscillations and l_1 is the length of the deflected magnet. Combining theoretical calculations and experimental data, it can be concluded that if we give the magnets such lengths that

$$3l^4 - 15l^2 l_1^2 + \frac{45}{8}l_1^4 = 0 \tag{B.9}$$

you get

$$\frac{H}{M} = \frac{2(1 - a\tau)(1 - hH \sin \phi)}{R^3(1 + 3\beta\tau) \sin \phi} \left(1 + \frac{p}{R^2(1 + 2\beta\tau)}\right) \tag{B.10}$$

If we set, for simplicity, $l = 1$ and knowing that in practice it is $l > l_1$, it turns out $l_1 = 0.47$. Chistoni defined p as magnetometric coefficient. To calculate it he performed measurements of deviations at two distances R_1 and R_2, obtaining the deviations ϕ_1 and ϕ_2 at temperatures τ_1 and τ_2, so

$$\frac{2(1 - a_\tau 1)(1 - hH \sin \phi)}{R_1^3(1 + 3\beta\tau_1) \sin \phi} = A_1 \tag{B.11}$$

,

$$\frac{2(1 - a_\tau 1)(1 - hH \sin \phi)}{R_1^3(1 + 3\beta\tau_1) \sin_\phi 2} = A_2 \tag{B.12}$$

.

Appendix C

Atomic spin

The electron and total atomic spins are aligned either parallel or anti-parallel and we can measure the direction of one serves in order to determine the direction of the other.
We can be decomposed the electric field vector at position $x = 0$ of light linearly polarized in the $\widehat{\mathbf{y}}$ direction in two circularly polarized components of opposite helicity

$$E(0) = \frac{E_0}{2} e^{i\omega t}\widehat{\mathbf{y}} + c.c. + \frac{E_0}{4} e^{i\omega t}(\widehat{\mathbf{y}} + i\widehat{z}) + \frac{E_0}{4} e^{i\omega t}(\widehat{\mathbf{y}} - i\widehat{z}) + c.c. \tag{C.1}$$

where *c.c.* denotes the complex conjugate. The electric field, after traveling a distance $l = \frac{tc}{n(\nu)}$, becomes

$$E(l) = \frac{E_0}{4} e^{\frac{i\omega n_+(\nu)}{c}}(\widehat{\mathbf{y}} + i\widehat{\mathbf{z}}) + \frac{E_0}{4} e^{\frac{i\omega n_+(\nu)}{c}}(\widehat{\mathbf{y}}) + c.c. \tag{C.2}$$

The quantities of interest are

$$\overline{n}(\nu) = \frac{[n_+(\nu) + n_-(\nu)]}{2} \tag{C.3}$$

$$\Delta n(\nu) = \frac{n_+(\nu) - n_-(\nu)}{2} \tag{C.4}$$

$$E(l) = \frac{E_0}{4} e^{\frac{i\omega \overline{n}(\nu) l}{c}} e^{\frac{i\omega Delta \overline{n}(\nu) l}{c}}(\widehat{\mathbf{y}} + i\widehat{\mathbf{z}}) + \frac{E_0}{4} e^{\frac{i\omega \overline{n}(\nu) l}{c}} e^{\frac{i\omega \Delta \overline{n}(\nu) l}{c}}(\widehat{\mathbf{y}} - i\widehat{z}) + c.c. \tag{C.5}$$

Ignoring the common phase factor $e^{i\omega \overline{n}(\nu) l/c}$ and defining the rotation angle

$$\theta = \frac{\pi \nu l}{c}[n_+(\nu) - n_-(\nu)] \tag{C.6}$$

we have

$$\mathbf{E}(l) = E_0(\cos\theta\hat{\mathbf{y}} - \sin\theta\hat{\mathbf{z}}) \tag{C.7}$$

This represent the plane of polarization of the light rotates by an angle θ after traveling a distance l through a birefringent medium with $n_+(\nu) \neq n_-(\nu)$.
We can use the complex wave number $k(\nu)$ of the light and the complex dielectric constant $\bar{\varepsilon}(\nu)$ of the vapor. In this way the propagation of light through the vapor is

$$k(\nu) = k + ik \tag{C.8}$$

$$\epsilon(\nu) = \left(\frac{kc}{\omega}\right)^2 \tag{C.9}$$

giving the standard plane-wave solution

$$\mathbf{E}(x,t) = E_0 e^{i(kx-\omega t)} \tag{C.10}$$

The intensity of the light is proportional to $|\mathbf{E}|^2$.
The imaginary component of the complex wave number is the absorption coefficient

$$k = \frac{1}{2}n\sigma(\nu) \tag{C.11}$$

The real component of the complex wave number is related to the index of refraction

$$k = \frac{n(\nu)\omega}{c} \tag{C.12}$$

The regime is $\frac{kc}{\omega} - 1 \ll 1$ and $(\frac{kc}{\omega}) \ll 1$.
The dielectric constant is

$$\widetilde{\epsilon}(\nu) \approx 1 + 2\left(\frac{kc}{\omega} - 1\right) + \frac{2ikc}{\omega} \tag{C.13}$$

The real and imaginary parts of the dielectric constant are related by the Kramers-Kronig relations

$$Re[\epsilon(\nu)] = 1 + \frac{1}{\pi}\mathcal{P}\int \frac{Im[\epsilon(\nu')]}{\nu' - \nu}d\nu' \tag{C.14}$$

$$Re[\epsilon(\nu)] = -\frac{1}{\pi}\mathcal{P}\int \frac{Re[\epsilon(\nu')-1]}{\nu'-\nu}d\nu' \tag{C.15}$$

The $\mathcal{P}$ implies the Cauchy principal value of the integral and the relationship between the index of refraction and absorption cross-section is

$$n(\nu) = 1+\left(\frac{nc}{4\pi\nu}\right)\frac{1}{\pi}\mathcal{P}\int \frac{\sigma(\nu')}{\nu'-\nu}d\nu' = 1+\left(\frac{nr_e c^2 f}{4\nu}\right)\frac{1}{\pi}\mathcal{P}\int \frac{Re[\mathcal{V}(\nu'-\nu_0)]}{\nu'-\nu}d\nu' \tag{C.16}$$

We can obtain the index of refraction of light for a medium from the absorption profile of the light.
The relations between real and imaginary components are

$$Re[(\mathcal{V}(\nu-\nu_0)] = \frac{1}{\pi}\mathcal{P}\int \frac{Im[\mathcal{V}(\nu'-\nu_0)]}{\nu'-\nu'}d\nu' \tag{C.17}$$

$$Im[(\mathcal{V}(\nu-\nu_0)] = -\frac{1}{\pi}\mathcal{P}\int \frac{Re[\mathcal{V}(\nu'-\nu_0)]}{\nu'-\nu'}d\nu' \tag{C.18}$$

so the index of refraction is

$$n(\nu) = 1 + \left(\frac{nr_e c^2 f}{4\nu}\right) Im[(\mathcal{V}(\nu-\nu_0))] \tag{C.19}$$

Redefining the Lorentzian lineshape in complex form, its real and imaginary components satisfy the same relations for the Voigt profile

$$\mathfrak{L}(\nu-\nu_0) = \frac{\Gamma_L/2\pi + i(\nu-\nu_0)/\pi}{(\nu-\nu_0)^2 + (\Gamma_L/2)^2} \tag{C.20}$$

It's possible to replace the Voigt profile with the complex Lorentzian lineshape in any equation, so we provide a valid approximation in the limit that $\Gamma_L \gg \Gamma_G$.
The absorption coefficients for $\sigma-$ and $\sigma+$ light and the indices of refraction $n_-(\nu)$ and $n_+(\nu)$, depend on the ground state populations $\rho - 1/2$ and $\rho + 1/2$, as well as the branching ratios of the optical excitation transitions. We are only interested in $D2$ transitions but to be thorough, consider that the $D1$ transition the indices of refraction are

$$n_-(\nu) = 1 + 2\rho\left(+\frac{1}{2}\right)\left(\frac{nr_e c^2 f_{D1}}{4\nu}\right) Im[\mathcal{V}(\nu-\nu_{D1})] \tag{C.21}$$

$$n_+(\nu) = 1 + 2Im[\mathcal{V}(\nu - \nu_{D1})] \tag{C.22}$$

while for the D_2 transition

$$n_-(\nu) = 1+2\left(\frac{3}{4}\rho(-1/2) + \frac{1}{4}\rho(+1/2)\right)\left(\frac{nr_e c^2 f_{D2}}{4\nu}\right) Im[\mathcal{V}(\nu-\nu_{D2})] \tag{C.23}$$

$$n_+(\nu) = 1+2\left(\frac{1}{4}\rho(-1/2) + \frac{3}{4}\rho(+1/2)\right)\left(\frac{nr_e c^2 f_{D2}}{4\nu}\right) Im[\mathcal{V}(\nu-\nu_{D2})] \tag{C.24}$$

The atomic vapor is birefringent when $\rho(-1/2 \neq \rho + 1/2))$, such that there is some nonzero polarization $P_x = 2\langle S_x\rangle = \rho(+1/2 - (-1/2))$. The total optical rotation is

$$\theta = \frac{\pi}{2} l n r_e c P_x \left(-f_{D1} Im[\mathcal{V}(\nu - \nu_{D1})] + \frac{1}{2} f_{D2} Im[\mathcal{V}(\nu - \nu_{D2})]\right) \tag{C.25}$$

where $nD1$ is the resonance frequencies of $D1$ and $nD2$ are the resonance frequencies of the $D2$ transitions.
Recall that $f_D1 \approx \frac{1}{2} f_D2$.
The optical rotation spectrum has a dispersive shape.
For rubidium the $D1$ and $D2$ transitions are well-separated, so we need only consider the resonance on which we are probing.

Appendix D

Skin depth

Equivalence of skin dept formulae

$$\delta(\omega) = \frac{1}{\omega}\left[\sqrt{\frac{\mu\varepsilon}{2}}\left(\sqrt{1+\left(\frac{\sigma}{\omega\varepsilon}\right)^2}-1\right)\right]^{-\frac{1}{2}} \tag{D.1}$$

$$= \frac{1}{\omega}\left(\frac{2}{\mu\varepsilon}\right)^{1/2}\frac{1}{\left(\sqrt{1+\left(\frac{\sigma}{\omega\varepsilon}\right)^2}-1\right)^{1/2}}\frac{\left(\sqrt{1+\left(\frac{\sigma}{\omega\varepsilon}\right)^2}+1\right)^{1/2}}{\left(\sqrt{1+\left(\frac{\sigma}{\omega\varepsilon}\right)^2}+1\right)^{1/2}} \tag{D.2}$$

$$= (\frac{2}{\mu\varepsilon})^{1/2}\frac{\varepsilon}{\omega}\left(\sqrt{1+\left(\frac{\sigma}{\omega\varepsilon}\right)^2}+1\right)^{1/2} \tag{D.3}$$

$$= \left(\frac{2\varepsilon}{\mu\sigma^2}\right)^{1/2}\left(\frac{\sigma}{\omega\varepsilon}\right)^{1/2}\left(\sqrt{\left(\frac{\omega\varepsilon}{\sigma}\right)^2+1}+\frac{\omega\varepsilon}{\sigma}\right)^{1/2} \tag{D.4}$$

$$= \sqrt{\frac{2}{\omega\mu\sigma}}\left(\sqrt{1+\left(\frac{\omega\varepsilon}{\sigma}\right)^2}+\frac{\omega\varepsilon}{\sigma}\right)^{1/2} \tag{D.5}$$

Acknowledgments

First and foremost I wish to thank my advisor, Prof. Emilio Mariotti, for his support and guidance during these years.
Through his interest and enthusiasm for my work, he has driven me to do my personal best in physics inside and outside the lab.
The enthusiasm, courage and pleasure in making research he is able to transfer to his collaborators has represented for me a strong stimulus in working.
I also took great advantage from the collaboration with my co-tutor Prof. Vincenzo Millucci, who has read and reread my Thesis.
Prof. Tarcisio Del Prete - of the blessed memory - deserves an acknowledgment for his efforts in helping me and the rest of the group in all the theoretical aspects of our research.
I also would like to thank him for giving me the opportunity to foster collaborations with Department of Physics and Astronomy of University College of London.
A particular acknowledgement goes to those who helped me in the everyday challenges of research.
Dr. Luca Marmugi has continuously monitored this work, dedicating to me a lot of time and patience.
Without his help end without the collaboration with Dr. Cameron Deans, this Thesis would not have seen the light.
I would thank all the people encountered in different moments and different places along this three year journey, which gave me fundamental inputs and answers: Prof. Luigi Moi, Prof. V. Biancalana, Prof. G. Bevilacqua, Prof. Andrea Sorbi and Prof. Maria Lucia Sampoli.
Dr. Nicolò Papi shared with me his experience in information technology and he helped me many times in tackling problems, planning and performing measurements as well as finding new solutions and ideas.
Dr. Claudio Marini supported me a lot in the final redaction.

Bibliography

[1] A. Abragam. *The principles of nuclear magnetism.* Oxford University Press, 1961.

[2] C. Affolderbach, C. Andreeva, S. Cartaleva, T. Karaulanov, G. Mileti, D. Slavov. *Light shift suppression in laser optically-pumped vapour-cell atomic frequency standards*, Appl. Phys. B 80, 841 – 848 (2005).

[3] C. Affolderbach, M. Sthler, S. Knappe, and R. Wynands. *An all-optical, highsensitivity magnetic gradiometer.* Applied Physics B, 75(6−7) : 605− 612, 2002.

[4] E. B. Alexandrov, M. Auzinsh, D. Budker, D. F. Kimball, S. M. Rochester, and V. V. Yashchuk. *Dynamic effects in nonlinear magneto-optics of atoms and molecules*, JOSA $B22$, 7 – 20 (2005).

[5] E. B. Alexandrov and V. A. Bonch-bruevich. *Optically pumped magnetometers after three decades*, Opt. Eng. 31, 711 – 717 (1992).

[6] J. C. Allred, R. N. Lyman, T. W. Kornack, and M. V. Romalis. *High-sensitivity atomic magnetometer unaffected by spin-exchange relaxation.* Physical Review Letters, 89(13) : 130801, 2002.

[7] G. Alzetta, L. Moi, G. Orriols. *Non absorption hyperfine resonances in a sodium vapor irradiated by a multimode dye laser*, Nuovo Cimento $B52$, 209 (1979).

[8] G. Alzetta, A. Gozzini, L. Moi, and G. Orriols. *An experimental method for the observation of r.f. transitions and laser beat resonances in oriented Na vapors*, Nuovo Cimento $B36$, 5 (1976).

[9] S. Appelt, A. B. Baranga, C. J. Erickson, M. V. Romalis, et al. *Theory of spinexchange optical pumping of* $3He$ *and* $129Xe$. Physical Review A, 58(2) : 1412, 1998.

[10] S. N. Atutov, R. Calabrese, V. Guidi, B. Mai, A. G. Rudavets, E. Scansani, L. Tomassetti, V. Biancalana, A. Burchianti, C. Marinelli, E. Mariotti, L. Moi, and S. Veronesi (2003).*Fast and efficient loading of a Rb magneto-optical trap using light-induced atomic desorption.* Physical Review A 67(5), 053401.

[11] M. Auzinsh, D. Budker, S. M. Rochester .*Optical polarized atoms.* Oxford University Press.(2010)

[12] M. Basso. *La misura assoluta del campo magnetico terrestre eseguita dagli astronomi di Brera nel* 1836*, secondo le modalità di Gauss, e suo sviluppo.* Annali di Geofisica, Vol.$XXXVI$, Suppl. N. 5,6. 1993.

[13] M. Basso, L. Cafarella, A. Meloni, P. Tucci.*Due secoli di strumenti geomagnetici in Italia* 1740 − 1971. Istituto nazionale di Geofisica, *Editrice Compositori*, 1997.

[14] M. V. Balabas, D. Budker, J. Kitching, P. D. D. Schwindt, and J. E. Stalnaker.*Magnetometry with millimeter-scale antirelaxation-coated alkali-metal vapor cells.* JOSA B, 23(6) : 1001 − 1006, 2006.

[15] W. E. Bell and A. L. Bloom.*Physical Review*, 1957.

[16] J. Belfi, G. Bevilacqua, V. Biancalana, S. Cartaleva, et al.*Cesium coherent population trapping magnetometer for cardiosignal detection in an unshielded environment.* JOSA B, 24(9) : 2357 − 2362, 2007.

[17] G. Bevilacqua, V. Biancalana, Y. Dancheva, and L. Moi.*All-optical magnetometry for NMR detection in a micro-Tesla field and unshielded environment.* Journal of Magnetic Resonance, 201(2) : 222 − 229, 2009.

[18] G. Bevilacqua, V. Biancalana, Y. Dancheva, A. Vigilante, et al.*Simultaneous detection of H and D NMR signals in a micro-Tesla field.* Journal of Physical Chemistry Letters, 2017.

[19] P. Bevington, R. Gartman,W. Chalupczak, C. Deans, et al.*Non-destructive structural imaging of steelwork with atomic magnetometers.* Applied Physics Letters, 113(6) : 063503, 2018.

[20] G. Bison, R. Wynands, and A. Weis.*Dynamical mapping of the human cardiomagnetic field with a room-temperature, laser-optical sensor*, Opt. Express 11, 904 − 909 (2003).

[21] F. Bloch.*Nuclear induction.* Physical Review, 70(7 – 8) : 460, 1946.

[22] N. Bloembergen, E. M. Purcell, and R. V. Pound.*Relaxation Effects in Nuclear Magnetic Resonance Absorption* Phys. Rev. 73, 679-Published 1*April*1948

[23] A. R. Borges, J. E. De Oliveira, J. Velez, C. Tavares, et al.*Development of electromagnetic tomography (EMT) for industrial applications. Part 2: Image reconstruction and software framework.* In Proc. 1*st* World Congr. Industrial Process Tomography, pages 219 – 225, 1999.

[24] E. Boto, N. Holmes, J. Leggett, G. Roberts, et al.*Moving magnetoencephalography towards real-world applications with a wearable system.* Nature, 555(7698) : 657, 2018.

[25] L. Bougas, L. D. Langenegger, C. A. Mora, M. Zeltner, et al.*Nondestructive inline sub-picomolar detection of magnetic nanoparticles in flowing complex fluids.* Scientific Reports, 8(1) : 3491, 2018.

[26] G. Breit and I. I. Rabi.*Measurement of nuclear spin.* Physical Review, 38(11) : 2082, 1931.

[27] J. Brossel and F. Bitter.*A New Double Resonance Method for Investigating Atomic Energy Levels. Application to* $Hg3P1$, Phys. Rev. 86, 308 (1952).

[28] D. Budker, W. Gawlik, D.F. Kimball, S.M. Rochester, V.V. Yashchuk, A. Weis.*Resonant nonlinear magneto-optical effects in atoms*, Rev. Mod. Phys. 74, 1153 (2002).

[29] D. Budker and D. F. Kimball.*Optical magnetometry.* Cambridge University Press 2013.

[30] D. Budker, D. F. Kimball, V. V. Yashchuk, and M. Zolotorev.*Nonlinear magnetooptical rotation with frequency-modulated light.* Physical Review A, 65(5) : 055403, 2002.

[31] D. Budker, D. F. Kimball, S. M. Rochester, V. V. Yashchuk, and M. Zolotorev.*Sensitive magnetometry based on nonlinear magneto-optical rotation.* Physical Review A, 62(4) : 043403, 2000.

[32] D. Budker and M. Romalis. *Optical magnetometry*. Nature Physics, 2007. D. Budker and D. F. Kimball. Optical magnetometry. Cambridge University Press 2013.

[33] M. Cheney and D. Isaacson. *Disguishability in impedance imaging*. IEEE Transactions on Biomedical Engineering, 39(8): 852 − 860, 1992.

[34] C. Chistoni. *Appendice - Sulla pubblicazione del Liznar*. Anleitung zur Mess. und Berech. der Elemente der Erdmagnetismus, 1885.

[35] R. J. Cooper, D. W. Prescott, P. Matz, K. L. Sauer, et al. *Atomic magnetometer multisensor array for RF interference mitigation and unshielded detection of nuclear quadrupole resonance*. Physical Review Applied, 6(6) : 064014, 2016.

[36] W. Daily and A. Ramirez. *Environmental process tomography in the United States*. The Chemical Engineering Journal and the Biochemical Engineering Journal, 56(3) : 159 − 165, 1995.

[37] Damadian R. *Tumor detection by nuclear magnetic resonance*. Science 1971; 171 : 1151 − 3. (First measurements of $T1$ and $T2$ relaxations of a wide range of normal tissues, including several cancers that showed prolongation of $T1$ and $T2$)

[38] H. B. Dang, A. C. Maloof, and M. V. Romalis. *Ultrahigh sensitivity magnetic field and magnetization measurements with an atomic magnetometer*. Applied Physics Letters, 97(15) : 151110, 2010.

[39] A. David, M. Cole, T. Horsley, N. Linford, et al. *A rival to Stonehenge?* Geophysical survey at Stanton Drew, England, 2004.

[40] O. Darrigol. *Electrodynamics from Ampère to Einstein*, Centre National de la Recherche Scientifique (Paris). Oxford University Press.

[41] C.Deans. *Electromagnetic Induction Imaging with Atomic Magnetometers-PhD Thesis*, Department of Physics and Astronomy of University College London.

[42] C. Deans, L. D. Griffin, L. Marmugi, and F. Renzoni. *Machine learning based localization and classification with atomic magnetometers*. Physical Review Letters, 120(3) : 033204, 2018.

[43] C. Deans, L. Marmugi, S. Hussain, and F. Renzoni.*Electromagnetic induction imaging with a radio-frequency atomic magnetometer*. Applied Physics Letters, 108(10) : 103503, 2016.

[44] C. Deans, L. Marmugi, S. Hussain, and F. Renzoni.*Optical atomic magnetometry for magnetic induction tomography of the heart*. In Quantum Optics, volume 9900, page 99000F. International Society for Optics and Photonics, 2016.

[45] C. Deans, L. Marmugi, S. Hussain, and F. Renzoni.*Electromagnetic induction imaging with a radio-frequency atomic magnetometer*. Applied Physics Letters, 108(10) : 103503, 2016.

[46] C. Deans, L. Marmugi, and F. Renzoni.*Electromagnetic induction imaging with atomic magnetometers*. In Imaging and Applied Optics. Optical Society of America, 2017.

[47] C. Deans, L. Marmugi, and F. Renzoni.*Through-barrier electromagnetic imaging with an atomic magnetometer*. Optics Express, 25(15) : 17911 − 17917, 2017.

[48] C. Deans, L. Marmugi, and F. Renzoni.*Active underwater detection with an array of atomic magnetometers*. Applied Optics, 57(10) : 2346 − 2351, 2018.

[49] C. Deans, L. Marmugi, and F. Renzoni*Sub-picotesla widely tunable atomic magnetometer operating at room-temperature in unshielded environments*. Review of Scientific Instruments, 89(8) : 083111, 2018.

[50] H. G. Dehmelt..Physical Review, 1957.

[51] E. C. Jordan and K. G. Balmain. *Electromagnetic waves and radiating systems, prentice hall*. Englewood Cliffs, New Jersey, 1968.

[52] W. Demtroeder.*Laser Spectroscopy*, 2*nd* Ed. Springer-Verlag, Berlin (1996).

[53] J. Dupont-Roc, S. Haroche and C. Cohen-Tannoudji.*Detection of very weak magnetic fields (*$10 - 9Gauss$*) by* $87Rb$ *zero-field level crossing resonance*, Phys. Lett. A, 28, 638 (1969).

[54] E. C. Jordan and K. G. Balmain. *Electromagnetic waves and radiating systems, prentice hall*. Englewood Cliffs, New Jersey, 1968.

[55] W. Demtroeder.*Laser Spectroscopy*, 2*nd* Ed. Springer-Verlag, Berlin (1996).

[56] J. Dupont-Roc, S. Haroche and C. Cohen-Tannoudji.*Detection of very weak magnetic fields* $(10-9Gauss)$ *by* $87Rb$ *zero-field level crossing resonance*, Phys. Lett. A, 28, 638 (1969).

[57] C. J. Erickson.*Measurements of the magnetic field dependence of the spin relaxation rate in alkali metal vapors*. PhD thesis, Princeton University, 2000.

[58] R. R. Ernst and W. A. Anderson.*Application of Fourier Transform Spectroscopy to Magnetic Resonance* Review of Scientific Instruments 37, 93 (1966).

[59] S. Esposito, M. Olimpo.*ACCADDE QUELL'ANNO - Quei moti "rivoluzionari" di Oersted, Ampère e Faraday. On the "revolutionary" motions of Oersted, Ampère and Faraday* GIORNALE DI FISICA DOI 10.1393/gdf/i2021 − 10394-9 $Vol.\ LXI$, N.4, ($Ottobre - Dicembre$ 1966).

[60] R. L. Fagaly.*Superconducting quantum interference device instruments and applications*. Review of Scientific Instruments, 77(10) : 101101, 2006.

[61] U. Fano.*Description of States in Quantum Mechanics by Density Matrix and Operator Techniques*. Rev. Mod. Phys. 29, 74 (1957).

[62] F. A. Franz.*Enhancement of alkali optical pumping by quenching*. Physics Letters A, 27(7) : 457 − 458, 1968.

[63] R. M. Fish and L. A. Geddes.*Conduction of electrical current to and through the human body: A review*. Eplasty, 9, (2009).

[64] M. Giorgi, E. Medi, F. Molina.*Rilievo Magnetometrico della Sicilia Centro-Settentrionale*.

[65] W. C. Griffith, S. Knappe, and J. Kitching.*Femtotesla atomic magnetometry in a microfabricated vapor cell*. Optics Express, 18(26) : 27167 − 27172, 2010.

[66] Garroway AN, Grannell PK, Mansfield P.*Image formation in NMR by a selective irradiative process.* J Phys C: Solid State Phys 1974; 7 : L457.462.

[67] A. Gozzini, F. Mango, J.H. Xu, G. Alzetta, F. Maccarrone and R.A. Bernheim.*Light-Induced Ejection of Alcali Atoms in Plysiloxane Coated Cells*, Nuovo Cimento 15, 709722 (1993)

[68] H. Griffiths.*Magnetic induction tomography. Measurement Science and Technology*, 12(8) : 1126, 2001.

[69] H. Griffiths, W. Gough, S. Watson, and R. J. Williams.*Residual capacitive coupling and the measurement of permittivity in magnetic induction tomography.* Physiological Measurement, 28(7) : S301, 2007.

[70] W. C. Griffith, S. Knappe, and J. Kitching.*Femtotesla atomic magnetometry in a microfabricated vapor cell.* Optics Express, 18(26) : $27167 - 27172$, 2010.

[71] H. Griffiths, W. R. Stewart, and W. Gough.*Magnetic induction tomography: A measuring system for biological tissues.* Annals of the New York Academy of Sciences, 873(1) : $335 - 345$, 1999.

[72] S. Groeger, G. Bison, J.-L. Schenker, R. Wynands and A. Weis.*A high-sensitivity laser-pumped Mx magnetometer*, Eur. Phys. J. D 38, $239 - 247$ (2006).

[73] L. Guarnieri Botti.*Elementi di Magnetismo.* Istituto idrografico della Marina, Genova 1980.

[74] R. Guilizzoni, J. C. Watson, P. Bartlett, and F. Renzoni.*Penetrating power of resonant electromagnetic induction imaging.* AIP Advances, 6(9) : 095017, 2016.

[75] L. Guilmette.*The History Of Maxwell's Equations.* - Sacred Heart University, (Class of 2012) Digital Commons@SHU.

[76] W. Happer.*Optical Pumping.* Reviews of Modern Physics, 44(2) : 169, 1972.

[77] W. Happer and B. S. Mathur.*Effective operator formalism in optical pumping.* Physical Review, 163(1) : 12, 1967.

[78] J. M. Higbie et al.*Robust, high-speed, all-optical atomic magnetometer*,Rev. Sci. Instrum. 77, 113106 (2006).

[79] Hinshaw WS.*Image formation by nuclear magnetic resonance: the sensitive point method*. J Appl Phys 1976; 47 : 3709 − 21.

[80] D. Holder.*Clinical and Physiological Applications of Electrical Impedance Tomography*. CRC Press, 1993.

[81] K. Hollaus, C. Magele, R. Merwa, and H. Scharfetter.*Numerical simulation of the eddy current problem in magnetic induction tomography for biomedical applications by edge elements*. IEEE Transactions on Magnetics, 40(2) : 623 − 626, 2004.

[82] A. Horsley and P. Treutlein.*Frequency-tunable microwave field detection in an atomic vapor cell*. Applied Physics Letters, 108(21) : 211102, 2016.

[83] S. Hussain, L. Marmugi, C. Deans, and F. Renzoni.*Electromagnetic imaging with atomic magnetometers: a novel approach to security and surveillance. In Detection and Sensing of Mines, Explosive Objects, and Obscured Targets XXI*, volume 9823, page 98230Q. International Society for Optics and Photonics, 2016.

[84] K. Jensen, R. Budvytyte, R. A. Thomas, T. Wang, et al.*Non-invasive detection of animal nerve impulses with an atomic magnetometer operating near quantum limited sensitivity*. Scientific Reports, 6 : 29638, 2016.

[85] T. Jeong, J. Y. Won, and H. Noh.*Line shapes in polarization spectroscopy for the rubidium $D1$ line in an external magnetic field*. Optics Communications, 292 : 106 − 110, 2013.

[86] C. N. Johnson, P. D. D. Schwindt, and M. Weisend.*Multi-sensor magnetoencephalography with atomic magnetometers*. Physics in Medicine and Biology, 58(17) : 6065, 2013.

[87] W. T. Joines, Y. Zhang, C. Li, and R. L. Jirtle.*The measured electrical properties of normal and malignant human tissues from* 50 *to* 900 *MHz*. Medical Physics, 21(4) : 547 − 550, 1998.

[88] E. C. Jordan and K. G. Balmain.*Electromagnetic waves and radiating systems, prentice hall*. Englewood Cliffs, New Jersey, 1968.

[89] J. G. Kappenman at al.*Geomagnetic Storms Can Threaten Electric Power Grid", American Geophysical Union, Earth in Space*, 9, 7, $9-11$ (1997).

[90] R. Karplus, J. M. Luttinger Hall Effect in Ferromagnetics, *Phys. Rev.* 95 1154 (1- *September* 1954).

[91] D. A. Keder, D.W. Prescott, A.W. Conovaloff, and K. L. Sauer.*An unshielded radiofrequency atomic magnetometer with sub-femtoTesla sensitivity.* AIP Advances, 4(12) : 127159, 2014.

[92] Knappe, P. D. D. Schwindt, V. Gerginov, V. Shah, L. Liew, J. Moreland, H. G. Robinson, L. Hollberg and J. Kitching.*Microfabricated atomic clocks and magnetometers*, Journal of Optics A: Pure and Applied Optics 8, $S318-S322$ (2006).

[93] R. H. Koch, J. G. Deak, and G. Grinstein.*Fundamental limits to magnetic-field sensitivity of flux-gate magnetic-field sensors.* Applied Physics Letters, 75(24) : 3862, 1999.

[94] A. Korjenevsky, V. Cherepenin, and S. Sapetsky.*Magnetic induction tomography: Experimental realization.* Physiological Measurement, 21(1) : 89, 2000.

[95] T. W. Kornack, G. Vasilakis, and M. V. Romalis.*Preliminary results from a test of CPT and lorentz symmetry using a* $K-3He$ *comagnetometer.* World Scientific Publishing Company, $1 : 206-213$, 2008.

[96] Kumar A, Welti D, Ernst RR.*NMR Fourier Zeugmatography.* J Magn Reson 1975; $18 : 69-83$.

[97] P.C. Lauterbur*Image Formation by Induced Local Interactions: Examples Employing Nuclear Magnetic Resonance.* Nature volume 242, pages $190-191(1973)$

[98] M. P. Ledbetter, V. M. Acosta, S. M. Rochester, D. Budker, et al.*Detection of radiofrequency magnetic fields using nonlinear magneto-optical rotation.* Physical Review A, 75(2) : 023405, 2007.

[99] H. L. Libby.*Introduction to electromagnetic nondestructive test methods.* Krieger, 1971.

[100] G. Liu and S. Gu.*Experimental study of the CPT magnetometer worked on atomic energy level modulation.* Journal of Physics B: Atomic, Molecular and Optical Physics, 43(3) : 035004, 2010.

[101] Mansfield P.*Multi-planar image formation using NMR spin echoes.* J Phys C: Solid State Phys 1977; 10 : $L55 - L58$.

[102] Mansfield P, Grannell PK.*em NMR 'diffraction' in solids* J Phys C: Solid State Phys 1973; 6 : $L422 - L426$.

[103] Mansfield P, Maudsley AA.*Planar spin imaging by NMR.* J Magn Reson 1977; 27 : $101 - 119$.

[104] Mansfield P, Maudsley AA.*Medical imaging by NMR.* Br J Radiol 1977; 50 : $188 - 194$. (First image of human finger)

[105] E. Mariotti, G. Bevilacqua, V. Biancalana, R. Cecchi, et al.*Forty years after the first dark resonance experiment: an overview of the COSMA project results.* In $19th$ International Conference and School on Quantum Electronics: Laser Physics and Applications, volume 10226, page $102260K$. International Society for Optics and Photonics, 2017.

[106] L. Marmugi, C. Deans, and F. Renzoni.*Atomic magnetometry-based electromagnetic imaging of low-conductivity semiconductors.* [Submitted: May 2018], 2018.

[107] L. Marmugi, L. Gori, S. Hussain, C. Deans, and F. Renzoni.*Remote detection of rotating machinery with a portable atomic magnetometer.* Applied Optics, 56(3) : $743 - 749$, 2017.

[108] L. Marmugi, S. Hussain, C. Deans, and F. Renzoni.*Magnetic induction imaging with optical atomic magnetometers: towards applications to screening and surveillance.* In Optics and Photonics for Counterterrorism, Crime Fighting, and Defence XI; and Optical Materials and Biomaterials in Security and Defence Systems Technology XII, volume 9652, page 965209. International Society for Optics and Photonics, 2015.

[109] L. Marmugi and F. Renzoni.*Optical magnetic induction tomography of the heart.* Scientific Reports, 6 : 23962, 2016.

[110] V. Mathé, F. Lévêque, P. Mathé, C. Chevallier, and Y. Pons. *Soil anomaly mapping using a caesium magnetometer: Limits in the low magnetic amplitude case. Journal of Applied Geophysics*, 58(3) : 202 − 217, 2006.

[111] D.D. McGregor (1987).*High-sensitivity helium resonance magnetometers*. Review of Scientific Instruments 58 (6), 1067 − 1076.

[112] R. Merwa, K. Hollaus, O. Bir, and H. Scharfetter.*Detection of brain oedema using magnetic induction tomography: A feasibility study of the likely sensitivity and detectability*. Physiological Measurement, 25(1) : 347, 2004.

[113] R. Merwa, K. Hollaus, B. Brandsttter, and H. Scharfetter.*Numerical solution of the general* 3*D eddy current problem for magnetic induction tomography (spectroscopy)*. Physiological Measurement, 24(2) : 545, 2003.

[114] M. Meucci, E. Mariotti, P. Bicchi and L. Moi.*Light-Induced Atom Desorption*, Europhys. Lett. 25, 639643 (1994).

[115] M. Meyerstein.*Fisica*, SIRBEC scheda PSTRL- $s6010 - 00011$.

[116] G. Musmann. Fluxgate magnetometers for space research.*BoD-Books on Demand*, 2010.

[117] I. Novikova, A.B. Matsko, V.A. Sautenkov, V.L. Velichansky, G.R. Welch, M.O. Scully.*Ac-Stark shifts in the non-linear Faraday effect*, Optics Letters 25, 1651 − 1653 (2000).

[118] I. Novikova, D.F. Phillips, A.S. Zibrov, R.L. Walsworth, A.V. Taichenachev, and V.I. Yudin. *Cancellation of lightshifts in an N-resonance clock*, Optics Letters 31, 622 − 624 (2006).

[119] .*The Magnetic Moment of the Hydrogen Atom*, (12 Nov 1926). Vol 64, Issue 1663 pp. 480 − 481 DOI: 10.1126/science.64.1663.480.

[120] .*The Magnetic Moment of the Hydrogen Atom*, Phys. Rev. 29, 309 (1 *February* 1927).

[121] F. Primdahl.*The fluxgate magnetometer. Journal of Physics E: Scientific Instruments*, 12(4) : 241, 1979.

[122] S. Pustelny, D. F. Kimball, C. Pankow, M. P. Ledbetter, et al. *The global network of optical magnetometers for exotic physics (GNOME): A novel scheme to search for physics beyond the standard model*. Annalen der Physik, 525(8 – 9) : 659 – 670, 2013.

[123] S. Pustelny, A. Wojciechowski, M. Gring, M. Kotyrba, et al. *Magnetometry based on nonlinear magneto-optical rotation with amplitude-modulated light*. Journal of Applied Physics, 103(6) : 063108, 2008.

[124] I.I. Rabi, J.R. Zacharias, S. Millman, P. Kusch. *A new method of measuring nuclear magnetic moment*, Phys. Rev. 53, 318 (1938).

[125] A. Ramirez, W. Daily, A. Binley, D. LaBrecque, and D. Roelant. *Detection of leaks in underground storage tanks using electrical resistance methods*. Journal of Environmental and Engineering Geophysics, 1(3) : 189 – 203, 1996.

[126] A. Ramirez, W. Daily, D. LaBrecque, E. Owen, and D. Chesnut. *Monitoring an underground steam injection process using electrical resistance tomography*. Water Resources Research, 29(1) : 73 – 87, 2010.

[127] S. Rebic, D. Vitali, C. Ottaviani, P. Tombesi, M. Artoni, F. Cataliotti and R.Corbalan. *Polarization phase gate with a tripod atomic system*, Phys. Rev. *A*70, 032317 (2004).

[128] M. A. Rosenberry, J. P. Reyes, D. Tupa, and T. J. Gay. *Radiation trapping in rubidium optical pumping at low buffer-gas pressures*. Physical Review A, 75(2) : 023401, 2007.

[129] G. J. Saulnier, R. S. Blue, J. C. Newell, D. Isaacson, and P. M. Edic. *Electrical impedance tomography*. IEEE Signal Processing Magazine, 18(6) : 31 – 43, 2001.

[130] I. M. Savukov and T. Karaulanov. *Multi flux transformer MRI detection with an atomic magnetometer*. Journal of Magnetic Resonance, 249 : 49 – 52, 2014.

[131] I. M. Savukov and M. V. Romalis. *NMR Detection with an Atomic Magnetometer*. Physical Review Letters, 94(12) : 123001, 2005.

[132] I. M. Savukov, S. J. Seltzer, and M. V. Romalis.*Detection of NMR signals with a radio-frequency atomic magnetometer*. Journal of Magnetic Resonance, 185(2) : 214 − 220, 2007.

[133] I. M. Savukov, S. J. Seltzer, M. V. Romalis, and K. L. Sauer. *Tunable atomic magnetometer for detection of radio-frequency magnetic fields*. Physical Review Letters, 95(6) : 063004, 2005.

[134] H. Scharfetter, H. K. Lackner, and J. Rosell.*Magnetic induction tomography: Hardware for multi-frequency measurements in biological tissues*. Physiological Measurement, 22(1) : 131, 2001.

[135] P. D. D. Schwindt, S.Knappe, V. Shah, L.Hollberg, J.Kitching, L.A. Liew and J. Moreland. *Chip-scale atomic magnetometer*, Appl. Phys. Lett. 85, 6409 − 6411 (2004).

[136] S. J. Seltzer.*Developments in alkali-metal atomic magnetometry*. PhD thesis, Princeton University, 2008.

[137] A. M. Sinton, R. W. M. Smith, F. J. McArdle, and B. H. Brown.*Fast display for real-time electrical impedance tomography*. In Engineering in Medicine and Biology Society, 1992 $14thAnnualInternationalConferenceoftheIEEE$, volume 5, pages 1708 − 1709. IEEE, 1992.

[138] S. J. Smullin, I. M. Savukov, G. Vasilakis, R. K. Ghosh, and M. V. Romalis.*Lownoise high-density alkali-metal scalar magnetometer*. Physical Review A, 80(3) : 033420, 2009.

[139] D. A. Steck.*Rubidium* $85D$ *line data* (2008). [Revised; $20September2013$], 2001.

[140] D. A. Steck.*Rubidium* $87D$ *line data* (2001). [Revised; $13January2015$], 2008.

[141] A. Tarantola.*Inverse problem theory and methods for model parameter estimation*, Volume 89. SIAM, 2005.

[142] S. Tumanski.*Induction coil sensors: A review. Measurement Science and Technology*, 18(3) : $R31$, 2007.

[143] A. Vander Vorst, A. Rosen, and Y. Kotsuka.*RF/microwave interaction mechanisms in biological materials. In RF/Microwave Interaction with Biological Tissues*, pages 63 – 92. Wiley-Blackwell, 2006.

[144] U. Volz and H. Schmoranzer.*Precision lifetime measurements on alkali atoms and on helium by beamgaslaser spectroscopy.* Physica Scripta, 1996(T65) : 48, 1996.

[145] M. E. Wagshul and T. E. Chupp.*Laser optical pumping of highdensity Rb in polarized* $3He$ *targets.* Physical Review A, 49(5) : 3854, 1994.

[146] D. K. Walter, W. M. Griffith, and W. Happer.*Magnetic slowing down of spin relaxation due to binary collisions of alkali-metal atoms with buffer-gas atoms.* Physical Review Letters, 88(9) : 093004, 2002.

[147] A. Wickenbrock, S. Jurgilas, A. Dow, L. Marmugi, and F. Renzoni.*Magnetic induction tomography using an all-optical* $87Rb$ *atomic magnetometer.* Optics Letters, 39(22) : 6367 – 6370, 2014.

[148] A. Wickenbrock, N. Leefer, J. W. Blanchard, and D. Budker.*Eddy current imaging with an atomic radio-frequency magnetometer.* Applied Physics Letters, 108(18) : 183507, 2016.

[149] A. Wickenbrock, F. Tricot, and F. Renzoni.*Magnetic induction measurements using an all-optical* $87Rb$ *atomic magnetometer.* Applied Physics Letters, 103(24) : 243503, 2013.

[150] R. Wyllie, M. Kauer, R. T. Wakai, and T. G. Walker.*Optical magnetometer array for fetal magnetocardiography.* Optics Letters, 37(12) : 2247 – 2249, 2012.

[151] H. Xia, A. B. Baranga, D. Hoffman, and M. V. Romalis.*Magnetoencephalography with an atomic magnetometer.* Applied Physics Letters, 89(21) : 211104, 2006.

[152] S. Xu, V. V. Yashchuk, M. H. Donaldson, S. M. Rochester, et al.*Magnetic resonance imaging with an optical atomic magnetometer.* Proceedings of the National Academy of Sciences, 103(34) : 12668−12671, 2006.

[153] .*Imaging system based on electromagnetic tomography (EMT).* Electronics Letters, 29(7) : 625, 1993.

[154] M. Zolgharni, P. D. Ledger, D. W. Armitage, D. S. Holder, and H. Griffiths.*Imaging cerebral haemorrhage with magnetic induction tomography: Numerical modelling.* Physiological Measurement, 30(6) : $S187$, 2009.